INFORMATION TO USERS

This reproduction was made from a copy of a document sent to us for microfilming. While the most advanced technology has been used to photograph and reproduce this document, the quality of the reproduction is heavily dependent upon the quality of the material submitted.

The following explanation of techniques is provided to help clarify markings or notations which may appear on this reproduction.

1. The sign or "target" for pages apparently lacking from the document photographed is "Missing Page(s)". If it was possible to obtain the missing page(s) or section, they are spliced into the film along with adjacent pages. This may have necessitated cutting through an image and duplicating adjacent pages to assure complete continuity.

2. When an image on the film is obliterated with a round black mark, it is an indication of either blurred copy because of movement during exposure, duplicate copy, or copyrighted materials that should not have been filmed. For blurred pages, a good image of the page can be found in the adjacent frame. If copyrighted materials were deleted, a target note will appear listing the pages in the adjacent frame.

3. When a map, drawing or chart, etc., is part of the material being photographed, a definite method of "sectioning" the material has been followed. It is customary to begin filming at the upper left hand corner of a large sheet and to continue from left to right in equal sections with small overlaps. If necessary, sectioning is continued again—beginning below the first row and continuing on until complete.

4. For illustrations that cannot be satisfactorily reproduced by xerographic means, photographic prints can be purchased at additional cost and inserted into your xerographic copy. These prints are available upon request from the Dissertations Customer Services Department.

5. Some pages in any document may have indistinct print. In all cases the best available copy has been filmed.

8505864

Randel, William John

STRUCTURE AND ENERGETICS OF MEDIUM-SCALE ATMOSPHERIC WAVES IN THE SOUTHERN HEMISPHERE SUMMER

Iowa State University   PH.D.   1984

University Microfilms International

300 N. Zeeb Road, Ann Arbor, MI 48106

PLEASE NOTE:

In all cases this material has been filmed in the best possible way from the available copy.
Problems encountered with this document have been identified here with a check mark __√__.

1. Glossy photographs or pages _____

2. Colored illustrations, paper or print _____

3. Photographs with dark background _√_

4. Illustrations are poor copy _____

5. Pages with black marks, not original copy _____

6. Print shows through as there is text on both sides of page _____

7. Indistinct, broken or small print on several pages _√_

8. Print exceeds margin requirements _____

9. Tightly bound copy with print lost in spine _____

10. Computer printout pages with indistinct print _____

11. Page(s) _____ lacking when material received, and not available from school or author.

12. Page(s) _____ seem to be missing in numbering only as text follows.

13. Two pages numbered _____. Text follows.

14. Curling and wrinkled pages _____

15. Other_____

Structure and energetics of medium-scale atmospheric waves

in the Southern Hemisphere summer

by

William John Randel

A Dissertation Submitted to the

Graduate Faculty in Partial Fulfillment of the

Requirements for the Degree of

DOCTOR OF PHILOSOPHY

Major: Physics

Approved:

In Charge of Major Work

For the Major Department

For the Graduate College

Iowa State University
Ames, Iowa

1984

TABLE OF CONTENTS

v

LIST OF FIGURES

LIST OF TABLES

I. INTRODUCTION

A complete understanding of the earth's atmosphere involves knowledge of its structure and of the physical processes which govern its evolution. The structure of the atmosphere cannot be known at all times and places; we must rely on limited observations, along with knowledge of basic physical principles in thermodynamics, radiative transfer, and fluid dynamics to serve as a basis for our understanding. The past decade has seen large advances in global circulation studies, primarily due to the use of satellite-based observations and computers for numerical simulations. As in other areas of science, advances are generally the result of the interaction between observations and theory. The preponderance of atmospheric observational studies have been based on Northern Hemisphere (NH) circulation statistics, as conventional observations are made with a relatively high density over the northern continents.

This work uses the above principles in an observational study of the large-scale flow in the atmosphere of the Southern Hemisphere (SH) during summer. This flow is found to be dominated by so-called 'medium-scale' waves, with typically 4-7 wavelengths fitting around a circle of latitude. These waves exhibit remarkably regular eastward phase progression, and at times globally symmetric wave patterns are observed. Observations of the structure of these waves are presented and interpreted in terms of geophysical fluid dynamics as applied to the earth's atmosphere. The medium-scale waves are found to be manifestations of a fundamental instability of the atmosphere, called baroclinic in-

stability. The observed wave characteristics are found to agree well
with those of modeled global scale baroclinic waves. In addition,
stationary medium-scale waves are occasionally present, and clear
instances of stationary-transient wave interference are observed and
studied.

In order to gain a correct perspective, the overall structure of
the atmosphere will be described, along with a review of the governing
large-scale dynamical principles.

A. Atmospheric General Circulation

The energy source of the atmosphere as a whole is the radiative
forcing due to the sun. The sun emits radiation as a blackbody source
with temperature near 5750°K, with the resulting solar flux at the earth
being approximately 1370 W/m^2. This flux is partially absorbed and par-
tially reflected from the ground or from clouds, the ratio of reflected
to incident flux being about 0.3 for the earth as a whole. Approximately
20% is absorbed in the atmosphere, while the remaining 50% is absorbed
by the surface.

The lower atmosphere is in local thermodynamic equilibrium, and
radiative emission is governed by the Planck blackbody function, with
an effective blackbody temperature near 250°K. The time over which
changes occur due to radiative processes in the lower atmosphere (below
30 km) is on the order of a week. Radiative processes thus act rather
slowly, and may often be neglected when considering short term atmospheric
developments. They are, however, of major importance to the long term

energy balance in the atmosphere.

The atmosphere is observed to be composed of approximately four parts nitrogen to one part oxygen. Because typical atmospheric temperatures are not close to phase transition temperatures of these gases, the atmosphere may be treated as a perfect gas, using the state equation:

$$p_s = \rho_s R T_s \text{ with } R = 287 \text{ J/kg-}^\circ K$$

Although atmospheric water vapor does undergo phase changes, the low mixture ratio still allows the above expression to be approximately valid.

Because the earth's atmosphere is in a gravitational field, and vertical motion is generally very small, the gravitational force on a parcel of air must be balanced by the vertical pressure gradient across that parcel. This situation is termed hydrostatic equilibrium. This may be stated mathematically as

$$- \rho_s g = dp_s/dz$$

This can be combined with the state equation and integrated to give

$$p_s(z) = p_\infty \exp(- \int_0^z dz/H), \text{ with } H = RT(z)/g.$$

Pressure, and also density, thus fall off exponentially with height, with an e-folding distance of H, called the vertical scale height. For the lower atmosphere, H is approximately 7 km.

Different vertical levels in the atmosphere are controlled by distinct physical processes, and these regions can be distinguished

by their vertical temperature profiles. The observed vertical distribution of temperature is shown in Figure 1. This represents a mean profile averaged over latitude, longitude and time.

The surface temperature maximum, maintained by solar radiation, falls off at a nearly constant rate of $-6.5°K/km$ throughout the lowest part of the atmosphere. This decrease in temperature with height, the so-called lapse rate, is dynamically constrained to be less than a certain value, the adiabatic lapse rate. The adiabatic lapse rate is the temperature change with height resulting from the adiabatic cooling of an air parcel due to vertical displacement in the hydrostatic pressure field. If the actual lapse rate is greater than this value, the atmosphere will be convectively unstable: convective effects will then return it to a stable configuration. Since convection is the dominant vertical heat transport mechanism here, this lowest portion of the atmosphere is termed the troposphere, or turning-sphere. The level dividing this region from those above is termed the tropopause.

Above the tropopause, the main features of the temperature structure are determined by radiative processes. The temperature is nearly constant with height in the lower stratosphere, so termed because this temperature profile indicates it is stably stratified. In the upper stratosphere, the temperature increases, due to ozone absorption of solar ultraviolet radiation, and reaches a maximum at the stratopause, near 50 km. This absorption is highly dependent on latitude during the solstices. The summer hemisphere is heated in polar regions, while the winter polar region, isolated from solar radiation, is relatively cold.
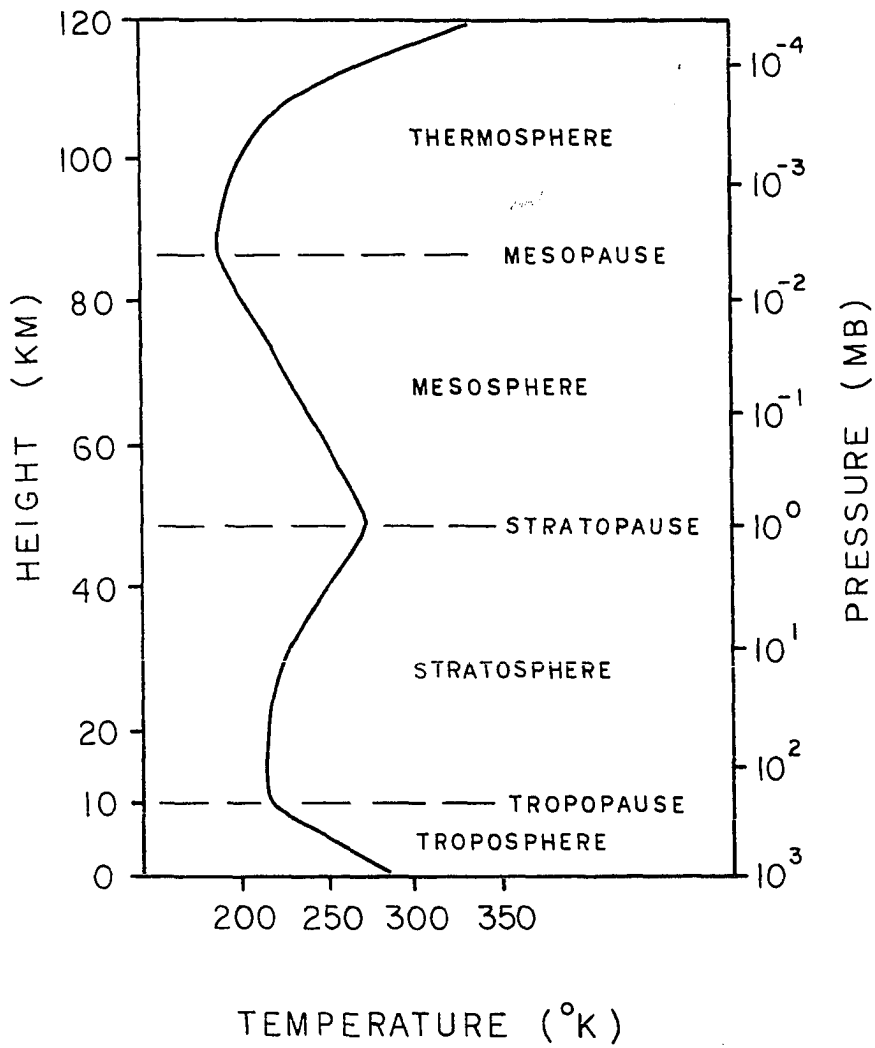
Figure 1. Vertical temperature structure of the atmosphere,
averaged over latitude, longitude and time

The temperature again falls in the mesosphere, or middle-sphere, though not as steeply as in the troposphere. A minimum is reached at the top of the mesosphere, called the mesopause, near 80 km, where there is little absorption of solar radiation.

Above this region, molecular diffusion dominates turbulence, molecular transitions are radiatively controlled, and local thermodynamic equilibrium is no longer valid. The dominant processes controlling the temperature is the absorption of extreme ultraviolet solar radiation by atomic oxygen, balanced by molecular conduction of heat. The temperature rises to between $500^\circ K$ and $2000^\circ K$ in this region known as the thermosphere.

The rest of the discussion here will be concerned with processes below 30 km, where, on the time-scale of several days, processes are dynamically controlled.

In the time mean, the net radiation received by the earth must equal that radiated back into space. The incoming flux is strongly dependent on latitude, however, while the outgoing flux is only weakly latitude dependent. This results in an excess of heat in equatorial regions and a deficit in polar regions. Just as convective effects limit the magnitude of vertical temperature gradients, so these strong horizontal temperature gradients will at some point be relieved by dynamical processes.

The first attempts to explain the resulting fluid circulation were due to Halley (1686) and Hadley (1735), who proposed an axially-symmetric circulation with rising motion in tropical regions and sinking in polar regions. This type of circulation is in fact observed, though

confined to tropical regions. Known as the Hadley cell, it consists of rising motion over the equator and sinking motion near latitudes 20-30°.

In mid-latitudes, the rotation of the earth becomes important on time scales longer than a day: Coriolis accelerations balance the pressure gradient forces arising from the radiative imbalance. This force balance is termed geostrophic, from Greek roots meaning earth-turning. The resulting motion is mainly east-west, and there is relatively little symmetric circulation. The hot equator and cold poles in the troposphere result in geostrophic westerly (from the west) jet streams in both summer and winter. In the stratosphere, the warm summer pole results in an easterly summer stratospheric jet, while a westerly jet in the winter stratosphere is the result of the cold pole.

The situation outlined above is not, however, dynamically stable. Large disturbances develop in mid-latitudes which in turn transport heat northward to relieve the imposed imbalance. These disturbances are thought to be manifestations of baroclinic instabilities, so named because they result from the baroclinicity (presence of horizontal temperature gradients) of the basic flow. Such instabilities appear to be of fundamental importance in the earth's atmosphere, and have also been observed in the ocean, in the atmosphere of Mars, and in laboratory experiments. Although a host of motions are possible depending on the imposed parameters of the system, structures with similar temporal and spatial scales repeatedly populate the SH summer atmosphere. An improved understanding of these features is the purpose of this present study.

Natural questions arise concerning these waves. What are their

observational properties? How do they grow and decay? How do they interact with their environment? Such questions have been the subject of extensive theoretical modeling efforts, which to a good degree explain the observed structure. Numerous observational studies, guided by theory, have attempted to understand the nature of these waves. A major problem is that the atmosphere is highly nonlinear, and it is usually difficult to clearly separate one type of wave motion from other atmospheric phenomena. This is especially true in the NH, where large amplitude stationary waves result from orography and sea-land heating contrasts. These stationary features result in preferred regions of baroclinic wave formation termed storm tracks, which are frequently populated by such waves. In addition, low-frequency planetary (large scale) waves, with time scales on the order of two weeks or more, may be forced by a variety of mechanisms. Recent studies have shown that these may contribute as much or more than baroclinic waves to the observed seasonal atmospheric variability in the NH. Most recent observational studies of the baroclinic waves employ spatial and/or temporal filtering techniques in an attempt to separate the properties of the waves from other effects.

A different situation exists in the SH, which is predominantly ocean-covered in midlatitudes, and usually devoid of large amplitude stationary waves. This is especially true during the summer, although the aforementioned low frequency planetary waves may occasionally be present. The SH summer atmosphere may thus provide an environment that allows planetary scale baroclinic waves to be studied without large effects from other phenomena. A negative point is that the data coverage

in the SH is much poorer than in the NH, although the use of meteorologi-
cal satellites has improved the data base, allowing the study of large
scale circulation patterns. The objective of this study is to charac-
terize the structure and energetics of medium-scale waves in the SH
summer, and compare results to theory and NH observations.

B. Waves in the Atmosphere

Wave motions result from a perturbed system trying to remain in
equilibrium. The equilibrium position is determined as a balance or
conservation of certain properties of the system. For the atmosphere,
we may list some of these conserved quantities: mass, momentum, energy,
and vorticity. (Vorticity is the curl of the velocity, a quantity in
fluid dynamics analogous to angular momentum in rigid-body dynamics.)

Fluid oscillations in the atmosphere may generally be divided into
two groups: 1) high frequency gravity waves, which are little af-
fected by variations in the Coriolis parameter with latitude, and 2) low
frequency planetary waves, whose existence depends on this variation.

Gravity waves, also called buoyancy waves, are oscillations that
result from the adiabatic adjustment of a fluid under gravity to an
initial disturbance. Typical horizontal wavelengths are on the order
of 1 to 100 km, with periods on the order of minutes to hours. On the
time scale of several days, gravity waves are unimportant in the
troposphere, although tropospherically-forced gravity waves which
propagate upwards are thought to be important to the circulation in
the mesosphere.

Planetary waves, also called Rossby waves, are long period oscillations of a rotating atmosphere that result from the conservation of vorticity. They are called planetary waves because of their large zonal (east-west) and meridional (north-south) extent: typical horizontal wavelengths are of the order of thousands of kilometers. The underlying dynamical principles of the waves were first discussed by C. G. Rossby and collaborators in the 1930s, and they are named in his honor. An observational study of such planetary scale features is the subject of the present work. A discussion of the geophysical fluid dynamics relevant to Rossby wave motion is given in the next chapter.

II. ROSSBY WAVE DYNAMICS

The problem to be considered here is how does a rotating fluid, under the influence of gravity, adjust to an initial disturbance on a slow time scale, i.e., when rotation is important. The objective in this section is not to derive all the relevant fluid equations, but rather to state the main assumptions and important results that will be used throughout this work, and give some feeling as to why they are meaningful.

The coordinate system used here is the mid-latitude β-plane, a planar approximation to the earth's sphericity in mid-latitudes, where the rate of rotation varies linearly with latitude. This is a good approximation as long as the meridional extent of the features is smaller than the radius of the earth. (The full spherical equations are used in actual calculations in this thesis, but the β-plane is used here because the equations assume much simpler forms.) Standard notation is used, as outlined in Appendix A, and the most important equations are numbered.

A. Zonal-Mean, Quasi-Geostrophic Theory

The basic governing equations of the atmosphere are the momentum, thermodynamic and continuity equations given in Appendix B. We are interested in wave motions, or departures from some average state. We may consider a time average, a spatial average, or some combination of the two. A good deal of theory has been developed for zonally averaged analyses, although in recent years, the emphasis has moved away from

averaging different climates around a latitude circle to averaging

(locally) in time. This is predominantly due to the longitudinally

localized nature of NH circulation patterns. A more zonally symmetric

situation is found in the SH, permitting zonally averaged analyses to

be more physically applicable, and that approach will be followed in

this work.

The underlying dynamical constraint for large scale motions is

the conservation of potential vorticity q (derived in Appendix B):

$$d/dt(q) = 0$$

where $\quad q = f^{-1}\nabla^2\phi + \rho_s^{-1} \frac{\partial}{\partial z} (\rho_s \frac{f}{N^2} \frac{\partial\phi}{\partial z})$

is called the potential vorticity. When this equation is linearized

about the zonally averaged flow, zonal mean (zeroth order) and perturba-

tion (first order) equations are obtained:

Zonal mean:

$$\frac{\partial}{\partial t} (\bar{q}) + \frac{\partial}{\partial y} \overline{v'q'} = 0 \tag{1}$$

Perturbation:

$$(\frac{\partial}{\partial t} + \bar{u} \frac{\partial}{\partial x})q' + v'\bar{q}_y = 0 \tag{2}$$

where $\quad \bar{q} = f - \frac{\partial \bar{u}}{\partial y} + \rho_s^{-1} \frac{\partial}{\partial z} (\rho_s \frac{f}{N^2} \frac{\partial\bar{\phi}}{\partial z})$

is the zonal mean potential vorticity,

$$q' = f^{-1}\nabla^2\phi' + \rho_s^{-1} \frac{\partial}{\partial z} (\rho_s \frac{f}{N^2} \frac{\partial\phi'}{\partial z}) \tag{3a}$$

is the perturbation potential vorticity, and

$$\bar{q}_y = \beta - \frac{\partial^2 \bar{u}}{\partial y^2} - \rho_s^{-1} \frac{\partial}{\partial z} \left(\rho_s \frac{f^2}{N^2} \frac{\partial \bar{u}}{\partial z} \right) \qquad (3b)$$

is the northward zonal mean potential vorticity gradient. It is well-known (Pedlosky, 1979, pp. 432-441) that when $\bar{q}_y$ is of the same sign throughout the fluid, only stable (nongrowing) Rossby waves are possible. On the other hand, a change in the sign of $\bar{q}_y$ is a necessary condition for instability.

Equation 2 will be the basis for much of our understanding of planetary or Rossby wave motion. Consider a traveling plane wave of the form:

$$\phi(x,y,z,t) = \phi_0 \exp\left(\frac{z}{2H}\right) \exp(i(kx + \ell y + mz - \sigma t)).$$

where $i = \sqrt{-1}$. The $\exp\left(\frac{z}{2H}\right)$ factor is incorporated due to the wave's constant energy density with height in the hydrostatic pressure field. Insertion into Equation 2 gives the Rossby wave dispersion relation:

$$\sigma = \bar{u}k - \frac{k\bar{q}_y}{(K^2 + F)} \qquad (4)$$

where $\quad K^2 = k^2 + \ell^2 + m^2 \left(\frac{f}{N}\right)^2 \quad$ and $\quad F = \frac{f^2}{4H^2N^2}$

Note the vertical wavenumber m is scaled by $\left(\frac{f}{N}\right)$, which is of order 10^{-2}. This is because vertical wavelengths are typically a hundred times smaller than horizontal wavelengths due to atmospheric stability.

The Rossby wave is dispersive. The zonal phase speed is given by:

$$c_{p_x} = \frac{\sigma}{k} = \bar{u} - \frac{\bar{q}_y}{(K^2 + F)}$$

while the components of the group velocity are given by:

$$c_{g_x} = \bar{u} - (-k^2 + \ell^2 + m^2 \left(\frac{f}{N}\right)^2 + F) \frac{\bar{q}_y}{(K^2 + F)^2} \tag{5a}$$

$$c_{g_y} = 2 k \ell \frac{\bar{q}_y}{(K^2 + F)^2} \tag{5b}$$

$$c_{g_z} = 2 k m \left(\frac{f}{N}\right)^2 \frac{\bar{q}_y}{(K^2 + F)^2} \tag{5c}$$

Two important properties of this plane Rossby wave are the associated zonal average northward heat flux $(\overline{v'T'})$ and northward momentum flux $(\overline{u'v'})$:

$$\overline{v'T'} = \frac{H}{2Rf} \exp\left(\frac{z}{H}\right) k \, m \, \phi_0^2 \tag{6}$$

$$\overline{u'v'} = - \frac{1}{2f^2} \exp\left(\frac{z}{H}\right) k \, \ell \, \phi_0^2 \tag{7}$$

These equations show that Rossby wave heat flux is associated with vertical phase tilts (a westward tilt with height indicates poleward heat transport), and momentum flux is associated with latitudinal phase tilts (a NW to SE tilt indicates poleward momentum transport). Comparison of Equations 5b, 5c, 6, and 7 also shows that, in the SH (where $f < 0$), the poleward heat and momentum fluxes are proportional to the vertical and equatorward group velocities, respectively. Rossby waves that tilt westward with height are thus propagating energy vertically, as well as transporting heat poleward, and poleward momentum transport is associated with equatorward group velocity.

B. Transformed Eulerian Mean (TEM) Formalism

A fundamental problem that arises when using the zonal average operator is the artificial separation of terms that are not physically

distinct. Consider the zonally averaged momentum and thermodynamic

equations (Equations B1 and B9):

$$\frac{\partial \bar{u}}{\partial t} + \frac{\partial}{\partial y} \overline{u'v'} - f\bar{v} = 0$$

$$\frac{\partial \bar{T}}{\partial t} + \frac{\partial}{\partial y} \overline{v'T'} + \frac{H}{R} N^2 \bar{w} = 0$$

Here $\overline{u'v'}$ and $\overline{v'T'}$ are regarded as components arising from the presence

of the waves, while $\bar{v}$ and $\bar{w}$ are associated with a mean meridional

circulation. However, the mean meridional motions include contribu-

tions which arise due to the presence of the wave induced fluxes of

heat and momentum. These contributions are given by (Pedlosky, 1979,

p. 376-377):

$$\bar{v}_e = \frac{R}{H} \rho_s^{-1} \frac{\partial}{\partial z} (\rho_s \frac{1}{N^2} \overline{v'T'})$$

$$\bar{w}_e = - \frac{R}{H} \frac{1}{N^2} \frac{\partial}{\partial y} (\overline{v'T'})$$

To take account of this fact, we can (following Edmon et al., 1980)

define a 'residual' meridional circulation $\overline{v^*}$, $\overline{w^*}$, which subtracts

these wave-induced contributions to the total $\bar{v}$ and $\bar{w}$:

$$\overline{v^*} = \bar{v} - \bar{v}_e$$

$$\overline{w^*} = \bar{w} - \bar{w}_e$$

and rewrite the zonal mean momentum and thermodynamic equations as:

$$\frac{\partial \bar{u}}{\partial t} - f\overline{v^*} = \rho_s^{-1} \nabla \cdot \vec{F} = DF \qquad (8)$$

$$\frac{\partial \bar{T}}{\partial t} + \frac{H}{R} N^2 \overline{w^*} = 0$$

where
$$\vec{F} = \begin{bmatrix} F_y \\ F_z \end{bmatrix} = \begin{bmatrix} -\rho_s \overline{u'v'} \\ \frac{fR}{H} \rho_s \frac{\overline{v'T'}}{N^2} \end{bmatrix} \tag{9a}$$

is called the Eliassen-Palm (EP) flux vector, and

$$DF = \rho_s^{-1} \nabla \cdot \vec{F} = \rho_s^{-1} \left(\frac{\partial F_y}{\partial y} + \frac{\partial F_z}{\partial z} \right) \tag{9b}$$

is the EP flux divergence. An important identity is given by:

$$DF = \rho_s^{-1} \nabla \cdot \vec{F} = \overline{v'q'} \tag{10}$$

i.e., the EP flux divergence is equal to the zonally averaged northward

potential vorticity flux.

The EP flux divergence is fundamental to understanding the inter-

action of Rossby waves with the zonally averaged flow. Under conditions

where the waves remain steady in time, the EP flux divergence is

identically zero. This is shown by taking q' times Equation 2 and

zonally averaging to get:

$$\frac{\partial}{\partial t} \left(\frac{1}{2} \overline{q'^2} \right) + \overline{v'q'} \cdot \overline{q}_y = 0 \tag{11a}$$

or equivalently

$$\frac{\partial}{\partial t} \left(\frac{1}{2} \frac{\overline{q'^2}}{\overline{q}_y} \right) + \overline{v'q'} = 0 \tag{11b}$$

The quantity $\left(\frac{1}{2} \overline{q'^2} \right)$ is called the wave potential enstrophy, and the

quantity $\left(\frac{1}{2} \frac{\overline{q'^2}}{\overline{q}_y} \right)$ is called the 'EP wave activity' or simply 'wave

activity.' If the wave amplitude is constant in time, these equations

show that the northward potential vorticity flux (Equation 10)

vanishes, and thus the EP flux divergence is zero. Equation 8 shows

that the zonal mean fields are also time-independent if the waves are

steady. Under these conditions, wave-induced mean flow changes are

exactly counterbalanced by wave-induced mean meridional motions, and no

net change occurs. This is called the nonacceleration theorem, first

discussed by Charney and Stern (1962). In general, forcing terms may

be included on the right hand side of Equations 11a and 11b. As shown

by Palmer (1982) and described in Appendix D, slight modifications are

necessary for Equations 10 and 11 to be valid for true planetary-scale

motions.

The nonacceleration theorem applies only in the limit that the

waves are steady in time. In the real atmosphere, waves grow and decay,

and the EP flux divergence provides information on where nonacceleration

is violated. In addition, in cases where the concept of group velocity

is valid, the EP flux vector is proportional to the Rossby wave group

velocity or energy flux vector, i.e., group velocity paths are EP

flux trajectories. A so-called EP flux diagram, containing the EP

flux vectors and EP flux divergence, then shows: a) wave source and

sink regions, b) the net effect of the waves on the mean flow, c) direc-

tion of wave-induced heat and momentum fluxes, and their relative im-

portance, and d) net wave propagation tendencies. Plotting conventions

used in these diagrams are discussed in Appendix C.

C. Energetics

We next consider the zonally averaged energy budget for Rossby waves and the zonal mean flow. The kinetic energy (KE) per unit mass is given by $\frac{1}{2}(u^2 + v^2)$. The potential energy of the atmosphere is comprised of two parts: the internal potential energy $(c_v T)$, and the gravitational potential (gz). Due to the hydrostatic pressure field, these two terms are proportional, and they may be combined to give the total potential energy $(c_p T)$. Not all of the potential energy in the atmosphere is available for release, as this could occur only by lowering the temperature to absolute zero and bringing all the mass to the surface. A quantity which is a measure of the amount of potential energy available for conversion through adiabatic processes was introduced by Lorenz (1955), and called the available potential energy (APE). The APE per unit mass is given by $\frac{1}{2}(\frac{\phi_z}{N})^2$. Here, ϕ_z is the vertical derivative of geopotential, equal to $\frac{RT}{H}$ (Equation B8).

The total zonal mean energy, integrated over the mass of the atmosphere is:

$$\bar{E} = \int dy \int dz \; \rho_s \; (\frac{1}{2}(\bar{u}^2 + (\frac{\widehat{\phi}_z}{N})^2))$$ (12)

where $\widehat{\phi}_z$ indicates the deviation of zonal mean temperature from the latitudinal mean. The total zonal mean wave energy is:

$$E' = \int dy \int dz \; \rho_s \; (\frac{1}{2}(\overline{u'^2} + \overline{v'^2} + \overline{(\frac{\phi'_z}{N})^2}))$$ (13)

Equations for the time rates of change of zonal mean and wave energy have recently been discussed by Plumb (1983), based upon the

TEM formalism. They are given by:

$$\frac{\partial \bar{E}}{\partial t} = \int dy \int dz \; \rho_s \; \bar{u} \; (\frac{\partial}{\partial y} \overline{u'v'} - \frac{R}{H} \rho_s^{-1} \frac{\partial}{\partial z} (\rho_s \frac{f}{N^2} \overline{v'T'})) \quad (14a)$$

$$= \int dy \int dz \; \rho_s \; \bar{u} \cdot (DF) \quad (14b)$$

while

$$\frac{\partial \bar{E}'}{\partial t} = - \int dy \int dz \; \rho_s \; \bar{u} \cdot (DF) \quad (15)$$

Note that the rate of energy change in the zonal mean is opposite and equal to the rate of change in the waves, i.e.:

$$\frac{\partial}{\partial t} (\bar{E} + E') = 0$$

The two terms in Equation 14a are of different physical origin. The first term is termed barotropic conversion, because of its dependence on horizontal gradients, and takes place due to the convergence of wave momentum flux. The second term is called baroclinic conversion, because it depends on the change with height of the wave structure. A changing northward flux with height produces a corresponding thermal wind change, and thus a change in the energy.

The EP flux divergence, already seen to be useful in studying the wave structure, is also found to be a fundamental quantity in studying wave energetics. Much of the theory developed here is based on many simplifying assumptions, namely a) no external heating or latent heat releases, b) no dissipation or frictional effects, c) no effects from topography, and d) linearity (although the nonacceleration theorem also holds for nonlinear waves). These effects are certainly at work in the real atmosphere, but it is anticipated that much of the dynamics of the

SH medium-scale waves can be understood based upon this simplified
analytical theory.

III. DATA AND ANALYSES

The data used in this study consist of wind and temperature fields derived from gridded geopotential height data, archived at the Climate Analysis Center, Washington, D.C. The time periods covered consist of 90 consecutive days during three SH summers: December 1 through February 28 of 1978-79, 1979-80, and 1980-81. This section will describe the origin and error characteristics of these data, along with the analyses used in this study.

A. Gridded Geopotential Data

Daily geopotential height data are obtained in the form of 4225 point (65 x 65) SH polar stereographic grids on the following standard pressure levels: 1000, 850, 700, 500, 400, 300, 250, 200, 150, 100, 70, 50, 30, 10, 5, 2, 1, and 0.4 mb. For this study, only data below 10 mb were used. Grids from 1000 to 100 mb are produced by the National Meteorological Center (NMC) based on analyses as outlined by Bergman (1979), and briefly reviewed here.

The NMC analyses are the result of a statistical 'optimal interpolation' of temperature and wind fields. Optimal interpolation is a scheme which estimates the value of a meteorological field at a particular location from a first guess at that location, and observations in the vicinity of that location. A numerical global prediction model (McPherson et al., 1979) is used to provide the background or first guess fields. This model is a primitive equation gridpoint model with 2.5 x 2.5 degree horizontal resolution and nine layers in the vertical.

The atmosphere between the surface and 50 mb is divided into two domains (6 layers in the troposphere and 3 layers above) separated by a material-surface tropopause near 250 mb. This separation has the effect of enhancing the vertical resolution without adding additional layers (McPherson et al., 1979), although there are some problems in the upper levels (to be discussed) that are not apparent below the tropopause level.

Observations are comprised of surface data from ships or buoys, aircraft reports, satellite cloud winds, rawinsonde (balloon) observations (raobs), and (most importantly in the SH) satellite-retrieved temperature profiles. Due to problems over high terrain, satellite retrievals are only used over oceanic regions. Observations are assigned rms error levels depending on the instrument and observation type, and weighted accordingly in the analyses. A much denser observational network was deployed in the SH during the Global Weather Experiment conducted during 1978-79; in particular, a large array of buoys provided improved sea-level pressure measurements for reference in 'building up' the geopotential grids.

The optimal interpolation is made on each of the nine layers in the model, then interpolated to standard pressure levels. The layer mean temperature is integrated vertically (using the hydrostatic equation) to give the geopotential height at each pressure level.

Grids above 100 mb are produced separately at the Climate Analysis Center, Washington, D.C., and stacked on the 100 mb NMC analyses. This procedure uses satellite-retrieved layer mean temperatures and raob data in a Cressman-type analysis system (Finger et al., 1965) to produce

stratospheric fields. Various satellite sounding systems were in use

during the periods covered in this study: the Vertical Temperature

Profile Radiometer (VTPR) aboard the NOAA-5 satellite until February 23,

1979, the Tiros Operational Vertical Sounder (TOVS) aboard TIROS-N

until January 20, 1980, and thereafter a similar TOVS system aboard

NOAA-6. Satellite data alone were used in the SH after October 17,

1980 (during the third season in this study), as the raobs are spaced

far enough apart that the analyses are considered more consistent with-

out them.

Both sets of data are centered on 1200 GMT. The optimum interpola-

tion procedure is updated every 6 hours, while data within plus and minus

6 hours of 1200 GMT are used in the upper levels. As the time scales

of interest here are generally of the order of 5-10 days, asynoptic

effects are probably small.

B. Error Characteristics

1. <u>Calculated</u> <u>versus</u> <u>observed</u> <u>wind</u> <u>comparisons</u>

In order to access the usability of these data, a preliminary

study was done in which geostrophic winds derived from the geopotential

grids were compared to actual measured winds. Even though the measured

winds are used in the analysis scheme, these comparisons provide a

check on the accuracy of the analyses. This study covered 8 days

(January 25-February 1) during 1979. The measured thermal wind (dif-

ference between wind at two vertical levels) between each pressure level

and 700 mb was calculated at various stations in southern mid-latitudes,

and compared to the geostrophic thermal wind derived from the geo-
potential grids, interpolated from the four grid points closest to each
station. The stations were separated according to their being over the
three continental regions (separately) or over ocean-covered area
(between 20 and 60°S latitude).

Figure 2 shows the mean and standard deviation of the grid-derived
minus observed thermal winds for meridional (v) and zonal (u) wind
components over ocean-covered areas and over Australia. The mean
differences are generally positive in both cases, indicating the grid-
derived geostrophic winds are slightly stronger than those observed.
The means change sign above 100 mb, perhaps a result of the different
grid analyses in that region. The standard deviations show similar
magnitudes for the u-component over both areas ($\simeq$ 10 m/s), although the
v-component shows larger values ($\simeq$ 20 m/s) over the oceans as compared
to over Australia ($\simeq$ 15 m/s). These results are not unexpected, as the
v-component will exhibit larger fluctuations than the u-component,
particularly in the upper troposphere, as a result of the waves to be
studied here. Stronger winds are generally found over the oceans, and
in addition, the grids over oceans are predominantly satellite derived,
while no satellite data is used over Australia. The overall good
comparison between the two areas enhances confidence in analyses of the
large, global-scale features that will be studied here.

The size of the standard deviations (10-20 m/s) are rather large
compared to the magnitudes of the winds involved (of order 30 m/s),
but these statistics are for point comparisons. The majority of the
analyses presented here involve the medium-scale wave Fourier components,
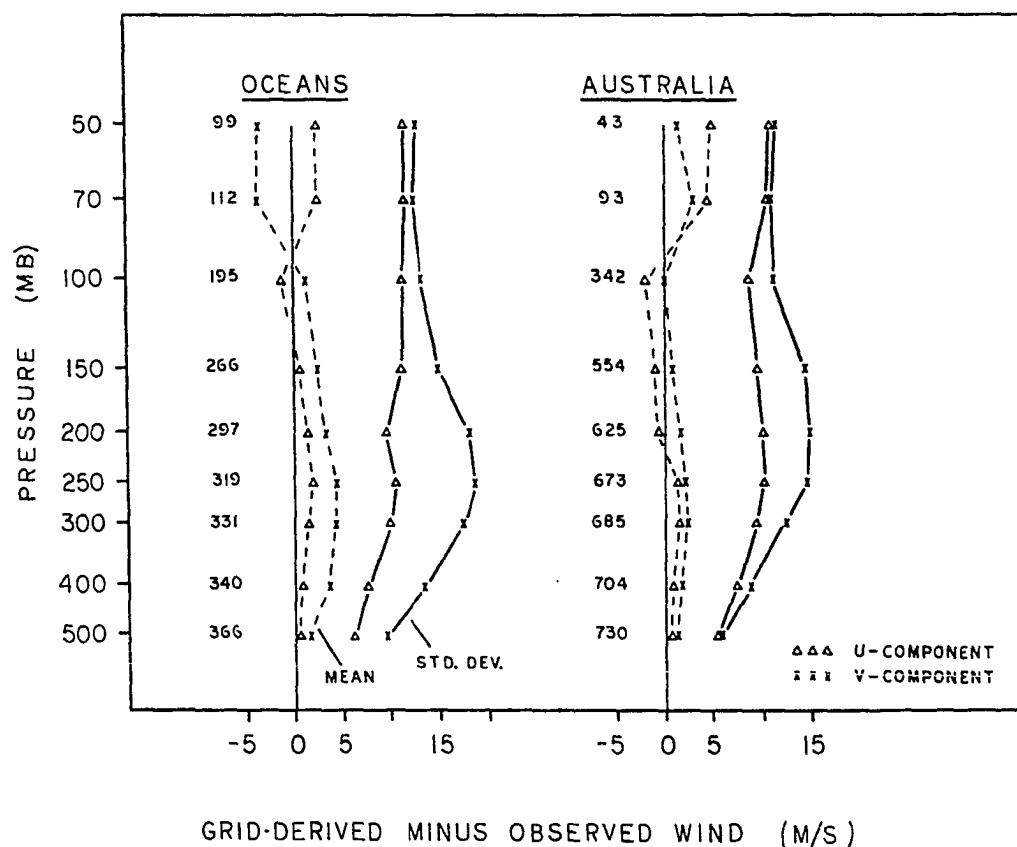
Figure 2. Means (dashed lines) and standard deviations (solid lines) of grid-derived minus observed thermal winds in the SH during January 25-February 1, 1979. Statistics are shown for zonal (u) and meridional (v) components separately, for measurements over ocean-covered area (left) and over Australia (right). Numbers to the left of the curves indicate the number of observations

which (since the above errors have been shown to be random) contain much smaller relative errors. In addition, most results will be shown to be consistent over large regions of latitude and height, increasing their reliability. The philosophy followed has been that results that are consistent in space and time, and physically realistic, will be treated as resulting from valid data.

2. Specific data problems

Several specific problems have been noted in the data, and listed here for future reference.

The geopotential grids above roughly 200 mb exhibit latitudinal 'bumps' at a spacing of approximately 10-15 degrees latitude. These bumps are most apparent when taking latitudinal derivatives, as is the case for many of the calculations used in this work. Tests have concluded that:

1) These bumps apparently originate as 'warm spots' in the 150-100 mb layer, not above 100 mb as might be expected from the different analyses scheme.

2) These bumps are not apparent below the tropopause level.

3) The bumps appear in zonally averaged quantities, but are also evident at all longitudes, i.e., they are not a longitudinally isolated problem.

4) The bumps are not a result of interpolation from the NMC grids to latitude-longitude grids.

5) The bumps result in unphysical results, such as gradients that are too sharp.

In order to alleviate this problem as much as possible, latitudinal derivatives are taken with a 5 degree grid spacing, reducing the response of these features (they are much more apparent using a 2.5 degree spacing). Nonetheless, several results still show effects from this problem in the upper levels, and such results should generally be overlooked. The problem is not apparent during 1980-81.

A second problem with the data is in a region near the west coast of South America at low latitudes (15-25°S latitude), where unreasonably large geostrophic winds result from several small scale irregularities in the grids at all pressure levels. These points do not significantly alter the low to medium wavenumber Fourier components considered here; in addition, most of our attention is focused in midlatitudes.

Small scale structure in the grids also result in a narrow stratospheric wind maximum in the vicinity southeast of Africa. It has been suggested that this is due to a problem of data associated with Marion Island (45°S latitude, 37°E longitude). This feature, along with the latitudinal bumps described earlier, are evident only above the tropopause. One may speculate that their appearance is connected with erroneous NMC analyses above the 'material surface' tropopause in their model.

C. Data Analyses

The first step in the data analysis is interpolation from the NMC 4225-point polar-stereographic grid to a regularly spaced 2.5 x 2.5 degree latitude-longitude grid. This is accomplished using a two-

dimensional Bessel 16-point interpolation scheme. The daily geopotential
fields are then Fourier analyzed at each latitude and pressure to obtain
the zonal sine and cosine coefficients, $ZS_k(\theta,p,t)$ and $ZC_k(\theta,p,t)$,
where k is the zonal wavenumber. These coefficients are obtained using
a standard fast Fourier routine available at the Iowa State University
Computation Center. Coefficients are retained to wavenumber 18. In-
frequent missing days are filled by linear interpolation.

Zonal Fourier coefficients of the geostrophic zonal and meridional
wind are found using Equations B5 and B6:

$$US_k(\theta,p,t) = - \left(\frac{g}{2\Omega r \sin \theta}\right) \frac{\partial}{\partial \theta} (ZS_k(\theta,p,t)$$

$$UC_k(\theta,p,t) = - \left(\frac{g}{2\Omega r \sin \theta}\right) \frac{\partial}{\partial \theta} (ZC_k(\theta,p,t)$$

$$VS_k(\theta,p,t) = - \left(\frac{gk}{2\Omega r \sin \theta \cos \theta}\right) ZC_k(\theta,p,t)$$

$$VC_k(\theta,p,t) = \left(\frac{gk}{2\Omega r \sin \theta \cos \theta}\right) ZS_k(\theta,p,t)$$

while the hydrostatic approximation allows the temperature coefficients
to be written:

$$TS_k(\theta,p,t) = \frac{g}{R} \frac{\partial}{\partial(\ln p)} (ZS_k(\theta,p,t))$$

$$TC_k(\theta,p,t) = \frac{g}{R} \frac{\partial}{\partial(\ln p)} (ZC_k(\theta,p,t))$$

Zonal averages of quantities such as $\overline{v'T'}$ are simply summations over
wavenumber, i.e.

$$\overline{v'T'} = \frac{1}{2\pi} \int_0^{2\pi} v'(\lambda,\theta,p,t) \cdot T'(\lambda,\theta,p,t)d\lambda$$

$$= \frac{1}{2} \sum_k (VS_k(\theta,p,t) \cdot TS_k(\theta,p,t) + VC_k(\theta,p,t) \cdot TC_k(\theta,p,t))$$

This allows convenient partitioning of such quantities according to their zonal scales.

Latitudinal averages are weighted by the cosine of latitude, to account for the sphericity of the earth. Vertical integrations, weighted by the density at each level, are simply a summation over pressure by use of the hydrostatic equation. Each pressure level is weighted by the pressure between midpoints (in altitude) of the standard levels. Limits of latitudinal averages are 25-65°S latitude, while the vertical integrations extend from 850 to 50 mb. The latitudinally-averaged and vertically-integrated value (referred to hereafter as the integrated value) of the variable $A(\theta,p)$ is then:

$$\frac{\int_{25}^{65} \cos\theta d\theta \int_{850}^{50} dp\, A(\theta,p)}{\int_{25}^{65} \cos\theta d\theta} = \frac{\sum_{i=25}^{65} \cos\theta_i \sum_{i=2}^{12} \Delta p_j\, A(i,j)}{\sum_{i=25}^{65} \cos\theta_i}$$

where Δp_j = 79, 179, 145, 101, 72, 50, 51, 51, 38, 25, and 9 mb for j=2-12, respectively.

Calculations involving the static stability parameter ($N^2(y,z)$) employ a standard field, shown in Figure 3b, based on the January 1979 average zonal-mean temperature field.

IV. OBSERVATIONAL ANALYSES

A. Basic States

Before analyzing the observational properties of the medium-scale waves, it is important to consider the properties of the basic state temperature and wind fields, which serve as an environment for the medium-scale waves. The general properties of these fields will be discussed in terms of their time-averaged values. The structure of the basic state fields changes with time, although such changes over the summer season (December-February) are small in comparison to their magnitude. The waves, on the other hand, undergo amplitude changes comparable to their average amplitude.

1. Time-averaged zonal mean structure

Since the analyses presented here will depend primarily on zonally-averaged quantities, the zonally-averaged wind and temperature fields are considered here. Because the flow is highly symmetric zonally (as shown in the next section), the zonal average is similar to longitudinal averages over any particular region.

The January 1979 mean zonally-averaged temperature field is shown in Figure 3a, and the associated Brunt-Väisälä frequency squared N^2 (Equation B9) field is shown in Figure 3b. Both pressure and geometrical height vertical scales are illustrated here; pressure coordinates alone will be used hereafter. The Brunt-Väisälä or buoyancy frequency, N^2, is the angular frequency (squared) of vertical buoyancy oscillations, and is an important dynamical quantity for Rossby waves. It is a measure of the static stability of the atmosphere: larger values
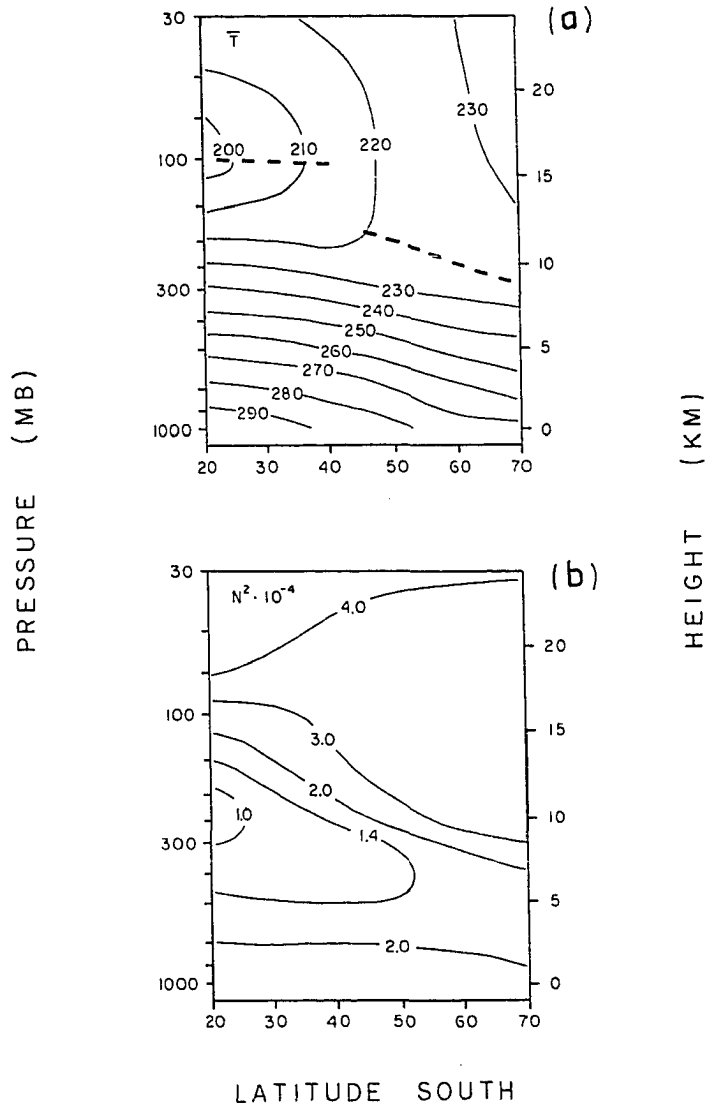
Figure 3. January 1979 average basic state structure. a) Zonal
mean temperature field ($^{\circ}$K). Approximate position
of tropopause is indicated by heavy dashed line.
b) Corresponding Brunt-Väisälä frequency squared,
N^2 ($10^{-4}s^{-2}$). The vertical scale on the left is
pressure (in mb), while that on the right is ap-
proximate geometrical height (in km)

indicate higher local stability. Local temperature changes, such as those caused by latent heat releases, can significantly alter the local stability characteristics, and model calculations show that this can be an important feedback mechanism in limiting the growth of small scale waves (Gall, 1976). Figure 3b shows the zonal and time average of N^2, simply indicating the mean overall structure.

The temperature decrease with height throughout the troposphere leads to relatively low stability there. The troposphere is thus the region most susceptible to instabilities involving vertical motions, an important part of baroclinic instabilities. Above the tropopause, small temperature changes with height result in increased stability, and N^2 is roughly twice its value in the troposphere. Note that the sloping tropopause is echoed in the N^2 structure.

Meridional sections of the zonal mean geostrophic wind $\bar{u}$ are shown in Figures 4a-c, representing seasonal means (December-February) for each of the three seasons studied. The general structure is similar for each season: a maximum westerly jet of approximately 30 m/s centered between 40 and 50°S latitude, near the tropopause. Note $\bar{u}$ increases with height throughout the troposphere and decreases with height in the lower stratosphere, in thermal wind balance with the latitudinal temperature gradient shown in Figure 3a. The seasonal-mean jets observed during 1978-79 and 1980-81 are similar in position, centered near 45-50°S latitude. During 1978-79, the jet exhibits weak horizontal wind shear (or gradient) on the equatorward side of the jet core, and a stronger gradient on the poleward side. The mean 1980-81 jet is more symmetrical in comparison; likewise, the mean

LATITUDE SOUTH
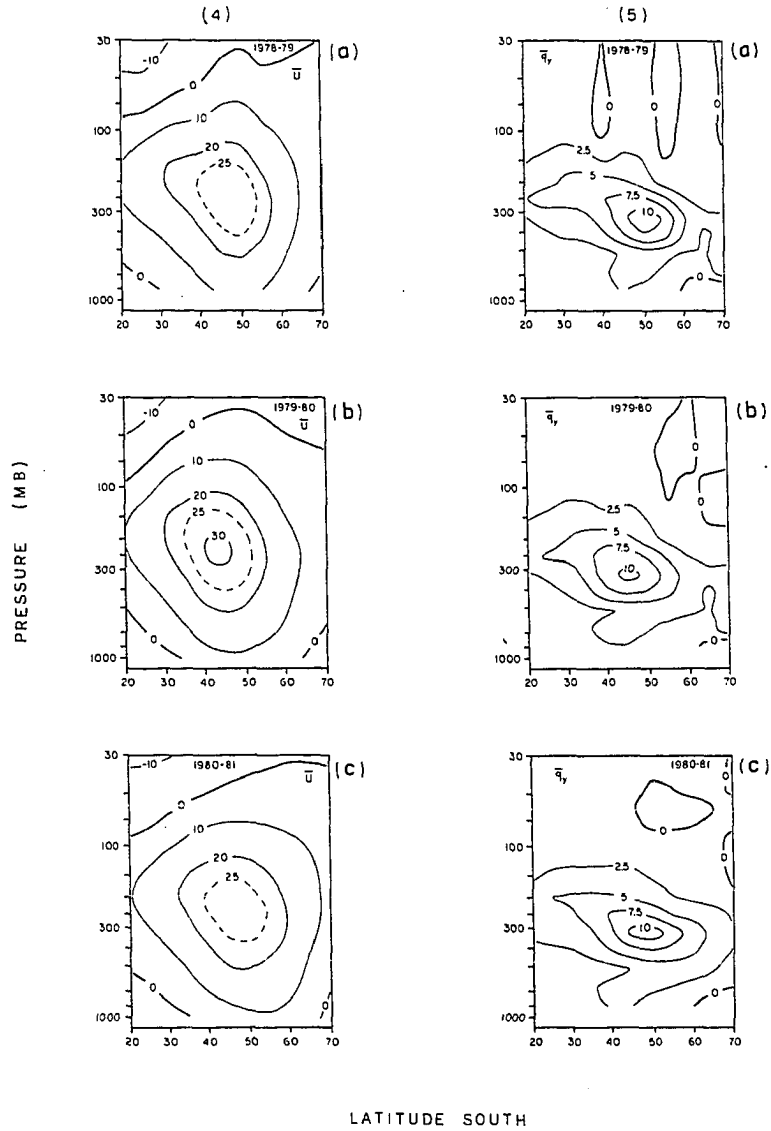
Figure 4. Seasonal (December 1-February 28) averages of the zonal mean wind (m/s) for a) 1978-79, b) 1979-80, c) 1980-81

Figure 5. Seasonally averaged zonal mean northward potential vorticity gradient $10^{-11}(m-s)^{-1}$ for a) 1978-79, b) 1979-80, c) 1980-81

1979-80 structure, which is a bit stronger and shifted equatorward

approximately 5 degrees.

The associated northward potential vorticity gradient ($\overline{q}_y$) fields

(Equation 3b) shown in Figures 5a-c, show a maximum slightly below

the corresponding jet maxima. This is due to the positive vertical

wind shear below the jet, whereas the negative wind shear on the top

of the jet suppresses $\overline{q}_y$ in that region. The maximum $\overline{q}_y$ during 1979-80

is shifted approximately 5 degrees equatorward, following the relative

position of the jet core during that season. The broader jet of 1980-81

is reflected in its broader $\overline{q}_y$ structure. As discussed in Section II.A,

positive values of $\overline{q}_y$ throughout most of the cross section considered

indicate a positive restoring force for parcels displaced latitudinally,

resulting in Rossby wave oscillations.

Regions where $\overline{q}_y$ changes sign indicate dynamically unstable areas.

The negative values found in Figures 5a-c are only marginally negative,

and may be the result of poor data. This is especially true of the

periodic structure above 150 mb in 1978-79, as discussed in the data

analysis section. The generally low values found on the poleward side

of the top of the jet during each season do, however, point to the pos-

sibility of internal instabilities in this region. These low values of

$\overline{q}_y$ are due to two contributing factors: 1) $\partial \overline{u}/\partial z$ is negative on the

top of the jet, and 2) $\beta - \partial^2 \overline{u}/\partial y^2$ is smallest on the poleward flank of

the jet. An instability resulting from (1) would be called baroclinic,

that resulting from (2) barotropic, while the two effects may both

contribute to (3) a combined baroclinic-barotropic instability. The

possibility of this being the main forcing mechanism of the medium-

scale waves was considered during early stages of this work. The charac-
teristics of such an instability would be a) equatorward heat flux in
the region above the jet, to reduce the horizontal temperature gradient
and vertical wind shears there, and b) poleward momentum flux, to re-
duce the large horizontal wind gradients. These wave characteristics
would combine to give a net positive EP flux divergence in the region
where $\bar{q}_y < 0$. The net change of wave enstrophy will be positive, as
Equation 11a shows with $\overline{v'q'} > 0$ and $\bar{q}_y < 0$. The observed medium-scale
wave characteristics make it apparent that this mechanism is not of
major importance in their generation. Such instabilities may, however,
provide a mechanism that prohibits the jet from becoming too sharp.

2.   Time-averaged horizontal structure

To get an idea of the longitudinal structure of the time-averaged
fields, the geostrophic zonal wind at 200 mb is shown in Figures 6a-c
for each of the three seasons. The SH summer exhibits a high degree
of zonal symmetry in mid-latitudes: the 20 m/s contour is nearly
continuous around the globe during each season. The major departure
from zonal symmetry comes from stronger winds in the eastern hemisphere,
south of Africa and Australia. These stronger winds are due to the
stronger latitudinal temperature gradient, which may be attributable to
the high, cold Antarctic plateau in the eastern hemisphere. In addition,
Figures 6b and 6c hint at a wavenumber 3 pattern which appears to be
associated with the 3 continental land masses.

The situation shown in Figures 6a-c is in sharp contrast to that
found in the NH, where large stationary waves result in more pronounced

(a)

(b)

(c)

LATITUDE SOUTH
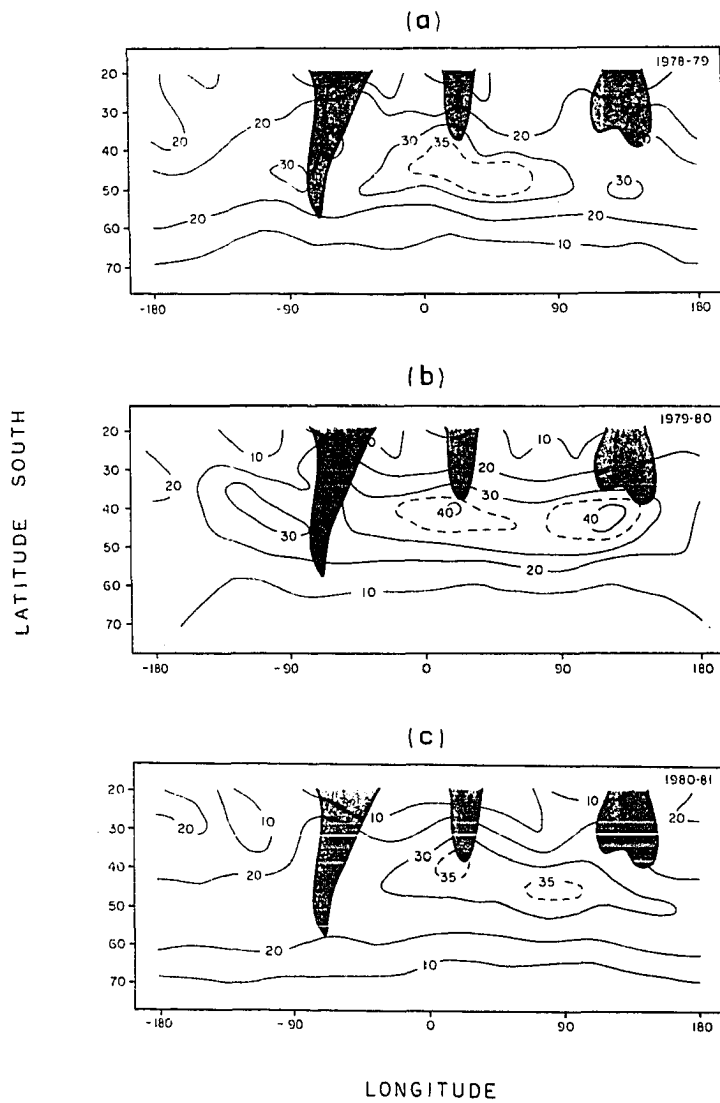
LONGITUDE

Figure 6. Seasonally averaged geostrophic zonal wind at 200
mb (m/s) for a) 1978-79, b) 1979-80, c) 1980-81.
The three continental areas are shaded

localized jet maxima. The longitudinal symmetry observed in the SH

summer encourages the physical applicability of a zonal average analysis,

in addition to its analytical advantages.

B. Zonal Wavenumber Analysis

To study hemispheric circulation patterns, it is convenient to

analyze contour plots of the geopotential height on constant pressure

surfaces. The geostrophic wind is everywhere parallel to these con-

tours, and inversely proportional to their spacing. When one studies

the circulation patterns in the SH summer in this manner, patterns

similar to those seen in Figures 7a-c are often observed. These

figures display the 200 mb geopotential height contours for December

11, 13, and 15, 1979, respectively. During each of these days, a pat-

tern with approximate six-fold symmetry about the south pole is evident.

This configuration is termed a zonal wavenumber 6 pattern, or simply

wave 6. Such waves are the focus of this study.

To facilitate study of these waves, it is helpful to isolate them

from features with different space and/or time scales. One method of

spatial scale separation is to project the geopotential onto orthogonal

functions, such as zonal harmonics, spherical harmonics, or empirical

orthogonal functions. Zonal harmonic analysis on constant latitude

circles is used in this study because it is economic and well-suited to

theory developed for zonal average analyses.

The scale of the wave motions observed in the SH summer may roughly

be divided into three groups — long, medium-scale, and short waves.
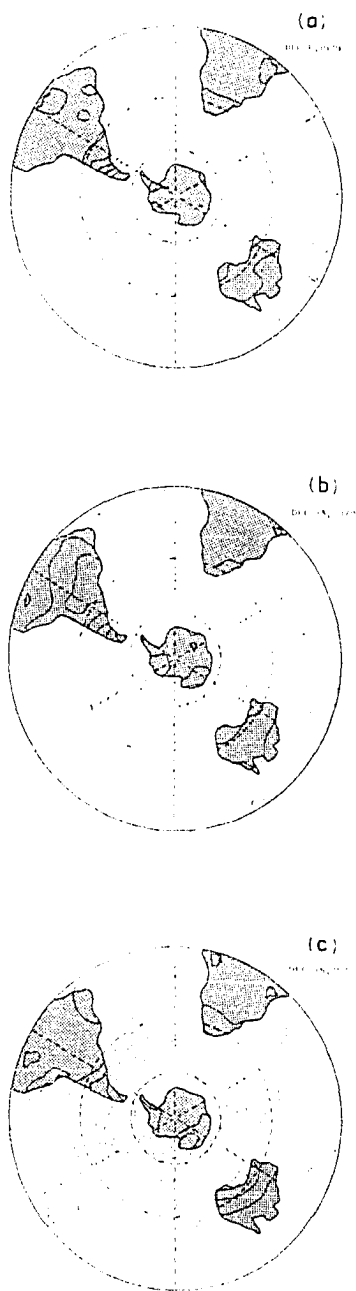
Figure 7. SH polar stereographic projections of the 200 mb
geopotential height contours for three days in
December 1979, based on NMC data. a) December 11,
b) December 13, c) December 15. Contour interval
is 200 gpm. Note the approximate six-fold symmetry
about the pole each day, and the eastward (clock-
wise) movement of the patterns with time

This is summarized in the time-averaged wave energy spectra shown in Figure 8. Each year the spectra are relatively flat for the lowest wavenumbers, with the most energy in wave 1. The dominance of wave 1 can be seen in Figures 6a-c, where the zonal wind exhibits a strong wave 1 pattern. This feature is roughly the same from year-to-year, i.e., it is a climatological mean stationary wave. A relative maximum in the wave energy is reached for waves 4-7, referred to as the medium-scale waves. This is the preferred scale for finite-amplitude baroclinic forcing in the SH summer atmosphere, and the resulting waves are the focus of this study. Above wave 7, the energy spectra falls off at a nearly constant rate (on the log-log plot), which is thought to be a result of turbulent transfer of energy to smaller wave scales (Charney, 1971).

C. Time-Averaged Medium-Scale Wave Characteristics

As will be shown, the medium-scale waves exhibit cycles during which they grow, reach a mature stage, and finally decay. The waves exhibit various amplitude and phase structures corresponding to different stages during these cycles. The nature of how these waves change in time will be discussed later. Here, we wish to consider some general properties of the waves, particularly in relation to the structure of the time-mean jet. We will thus consider time-averaged wave characteristics. Note that 1) the time-average assigns a higher weight to wave structure at times of large wave amplitude, and 2) the time-mean
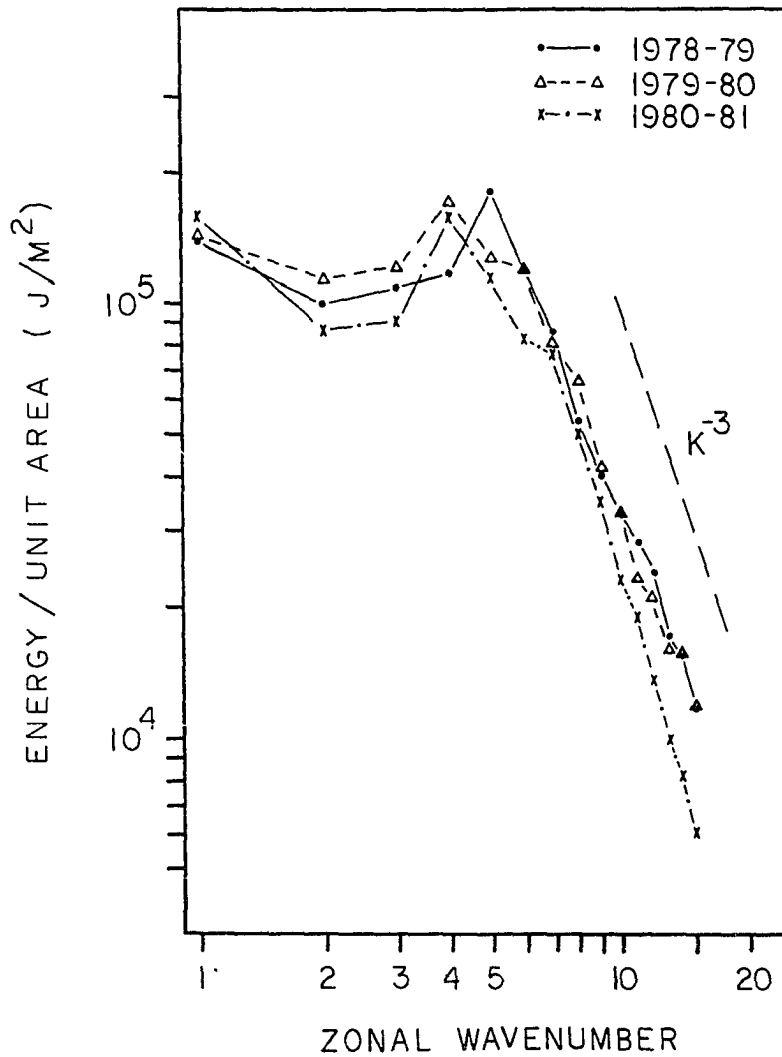
Figure 8. Seasonally-averaged integrated energy as a function of zonal wavenumber for each season in this study. Details of the energetic calculations are found in Section V

wave structure is in general different from the structure of the

time-mean, or stationary, waves.

1. Geopotential amplitude

The seasonal mean medium-scale wave geopotential amplitude for

each of the three seasons is shown in Figures 9a-c. The general struc-

ture is the same for each of the three seasons: a maximum of approxi-

mately 110 geopotential meters (gpm) in the upper troposphere in mid-

latitudes, near the jet core. For comparison, the amplitudes of wave 6

at 40°S latitude in Figures 7a-c are 123, 164, and 134 gpm, respectively.

2. Conservation of wave activity

This section will demonstrate that the relationship between the

medium-scale wave amplitude maximum and background zonal flow is

consistent with the conservation of wave activity. The location of the

wave amplitude maximum near the jet core is not attributable to this

region being the source of wave growth, as $\overline{q}_y$ is large and positive

throughout the region, inconsistent with instability requirements.

In Section V.F, it will be shown that the waves originate in the

lower levels and propagate upwards. As a Rossby wave packet propagates

through a slowly varying medium (away from regions of forcing), the local

wave activity $A_{(m)}$

$$A_{(m)} = r \cdot \cos\,\theta \cdot \rho_s \cdot \frac{\frac{1}{2}\overline{q'^2}}{\overline{q}_y}$$

will tend to be conserved (Equation D4). This implies that, in the

time-mean, $\frac{1}{2}\overline{q'^2}$ will be expected to have a similar meridional structure

to that of $\overline{q}_y$. Figures 10a-c show the meridional sections of the time-
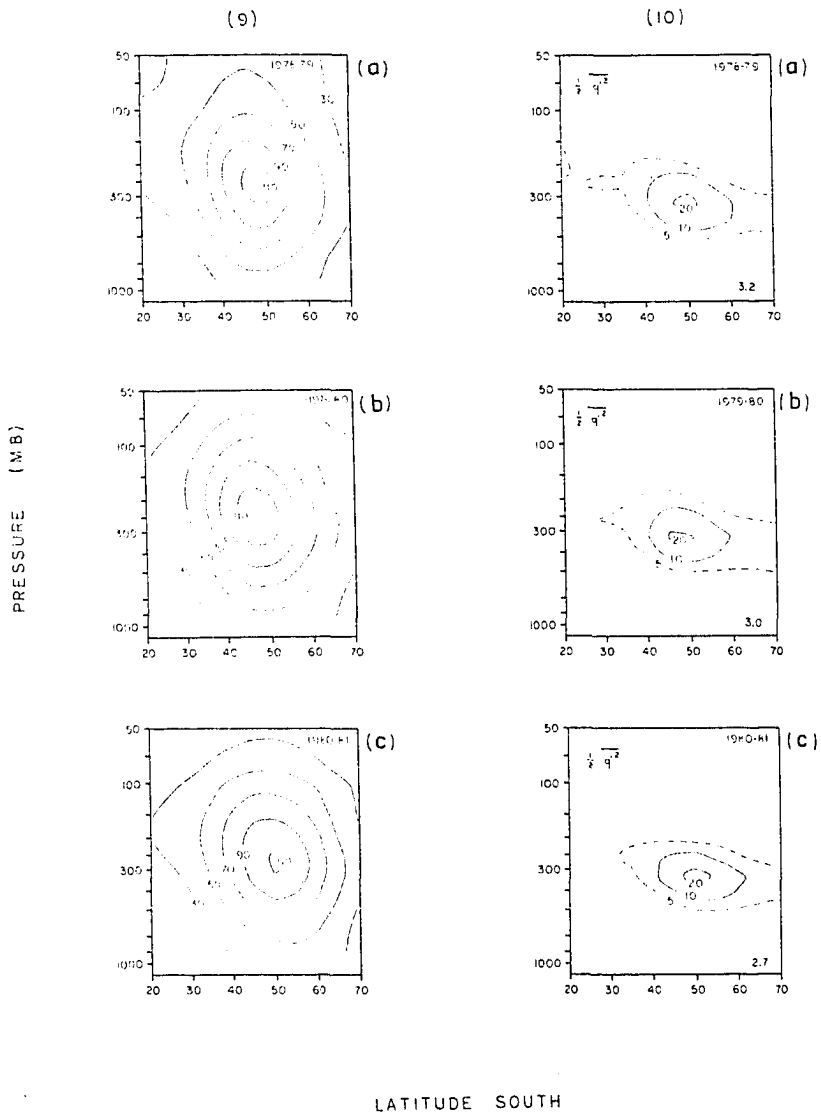
Figure 9. Seasonally-averaged medium-scale wave (k = 4-7) geopotential amplitude (gpm) for a) 1978-79, b) 1979-80, c) 1980-81

Figure 10. Seasonally-averaged medium-scale wave potential enstrophy $\frac{1}{2} \overline{q'^2}$ ($10^{-10}s^{-2}$). Numbers in lower right hand corner are integrated total, in (10^{-6} N/m^3). a) 1978-79, b) 1979-80, c) 1980-81

mean medium-scale wave potential enstrophy, $\frac{1}{2}\overline{q'^2}$ for each season.

Comparison with Figures 5a-c shows that the patterns of $\frac{1}{2}\overline{q'^2}$ are similar

to those of $\overline{q}_y$ for each season, and their 'cores' are nearly coincident.

Interannual differences in $\overline{q}_y$ are also observed in $\frac{1}{2}\overline{q'^2}$; note the broad

latitudinal structure of both quantities during 1980-81.

Figure 11 shows a meridional cross section of the quantity $A_{(m)}$,

based on the time-mean values of $\frac{1}{2}\overline{q'^2}$ and $\overline{q}_y$ for 1979-80 (shown in

Figures 5b and 11b, respectively). The time average of the ratio $\frac{1}{2}\overline{q'^2}/\overline{q}_y$

(calculated for each day) is perhaps more fundamental, although such

calculations show near identical structure to that observed in Figure 11.

The observed $A_{(m)}$ is roughly constant over much of the cross section

where $\frac{1}{2}\overline{q'^2}$ and $\overline{q}_y$ are large. Larger values of $A_{(m)}$ (approximately twice

the value elsewhere) are observed near the cores of $\frac{1}{2}\overline{q'^2}$ and $\overline{q}_y$, and also

poleward of 60°S latitude. The reason for the discrepancy is unclear. The

high number of derivatives involved in these calculations warrants caution

as to the exact results. In addition, other effects (wave forcing, non-

linearity, dissipation) may be involved. Nonetheless, the overall con-

sistency exhibited by $A_{(m)}$ demonstrates that the relative position of the

wave amplitude maximum and background jet structure is qualitatively

consistent with the conservation of local quasi-geostrophic wave activity.

3. Temperature amplitude

Consideration of the temperature structure associated with the

medium-scale waves is in a way redundant, since the temperature is

proportional to the vertical derivative of the geopotential studied

in the last section. The quasi-geostrophic theory applied here deems
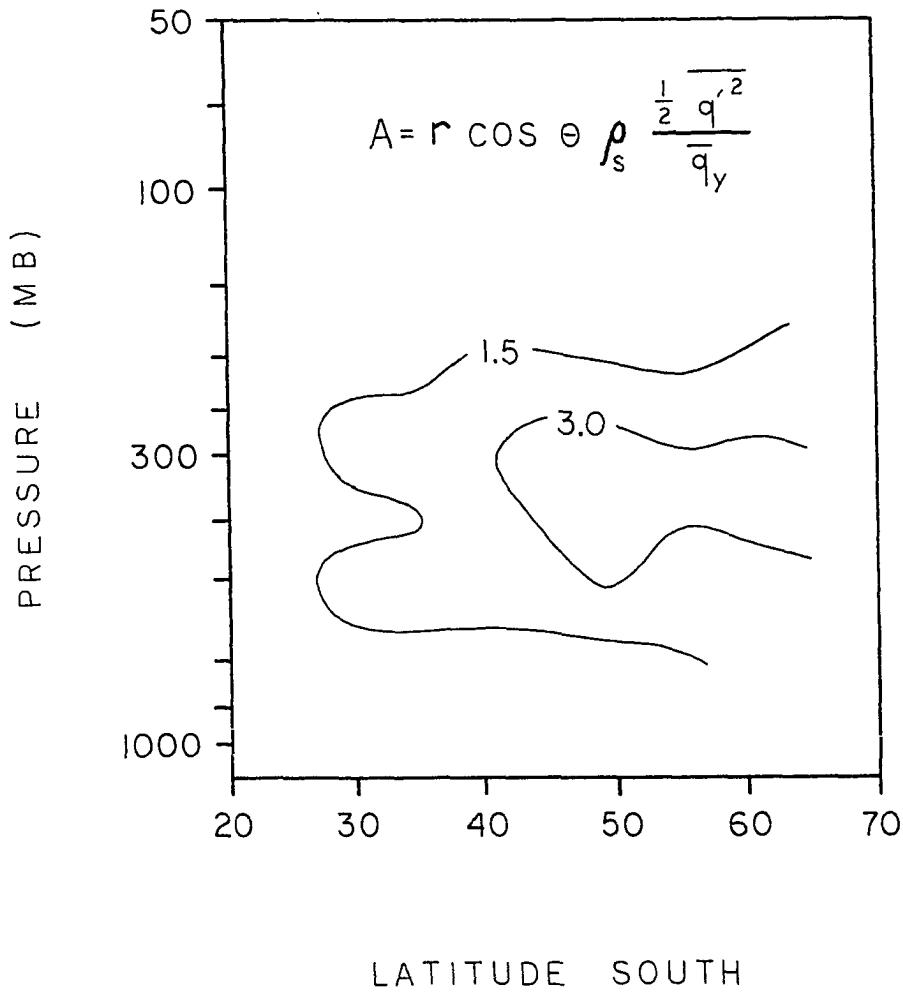
Figure 11. Meridional cross section of the 1979-80 time mean quasi-geostrophic wave activity $A_{(m)}$, defined in Equation D3, based on the time mean values of $\overline{q}_y$ and $\frac{1}{2} \overline{q'^2}$ (shown in Figures 5b and 10b, respectively). Units are 10^7 kg/(m-s)

the geopotential to be the more fundamental quantity, although tempera-
ture is the quantity that is observed in the atmosphere, and thus
also of fundamental importance.

Meridional cross sections of the seasonally-averaged medium-scale
temperature amplitude are shown in Figures 12a-c. A common feature is
the double maxima observed in the lower troposphere (500-700 mb) and in
the lower stratosphere (70-150 mb). These figures represent amplitude
only: the phase structure is such that the two peaks are always out
of phase, i.e., a negative perturbation always overlays a positive one.
This results in the 'buildup' of geopotential in the lower troposphere,
with a peak near the tropopause, and decay with altitude in the upper
levels.

The upper level peak observed during 1978-79 is of similar magni-
tude but positioned lower than the other years, centered near 150-200 mb,
as opposed to near 100 mb. This structure is reflected in the average
geopotential (see Figure 9a) which peaks near the same level (250 mb),
but decays more slowly into the stratosphere.

4. Heat flux

When considering the wave heat and momentum fluxes, it is im-
portant to keep in mind that the actual values change significantly
in time, depending on the maturity of the wave. The time-averaged
medium-scale wave northward heat flux is shown in Figures 13a-c.
Negative values denote heat transport towards the South Pole. Pole-
ward transport, with a relative maximum of approximately 6°K-m/s in
the lowest levels, is apparent each season. Significant year-to-year
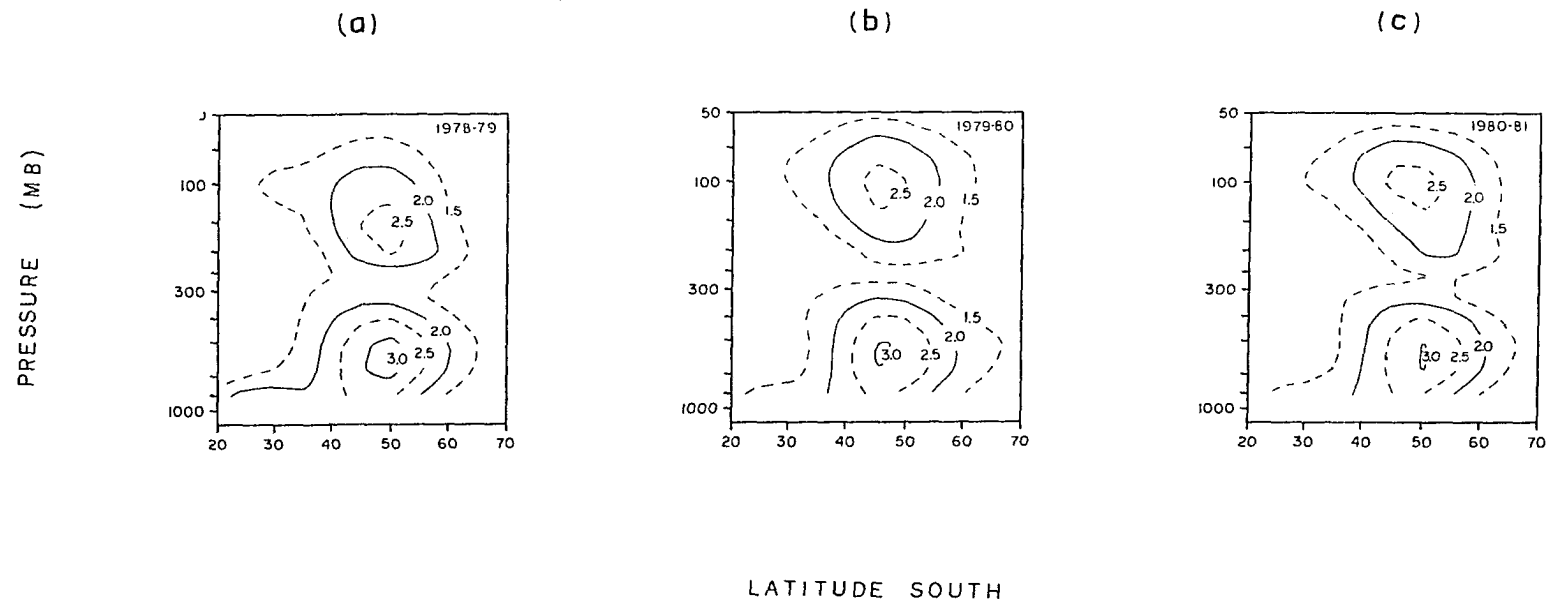
Figure 12. Seasonally-averaged medium-scale wave temperature
            amplitude (^OK).   a) 1978-79, b) 1979-80, c) 1980-81

46
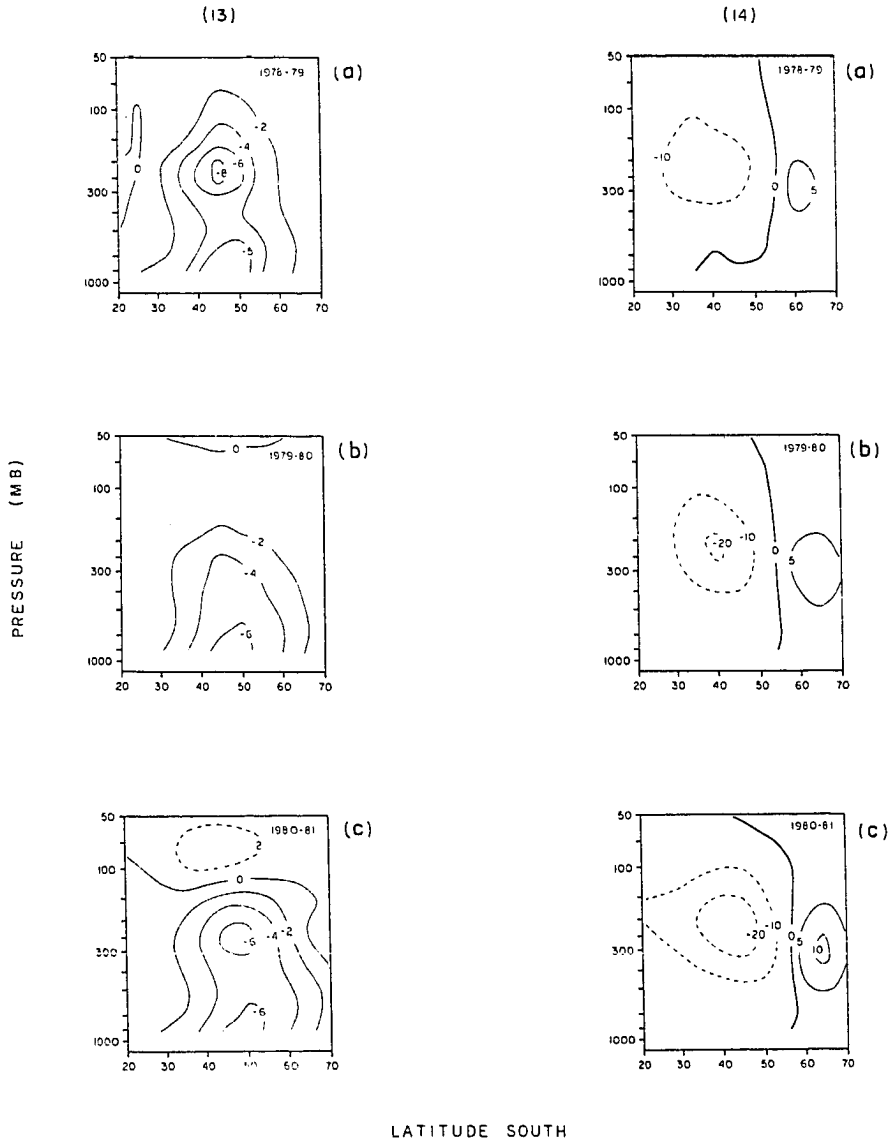
Figure 13. Seasonally-averaged medium-scale wave northward
heat flux $\overline{v'T'}$ ($^{\circ}$K - m/s). Negative values denote
transport towards the South Pole. a) 1978-79,
b) 1979-80, c) 1980-81

Figure 14. Seasonally-averaged medium-scale wave northward
momentum flux $\overline{u'v'}$ (m^2/s^2). Negative values denote
transport towards the South Pole. a) 1978-79,
b) 1979-80, c) 1980-81

variability in the overall structure is evident.

During 1978-79, there is a very strong secondary upper level maximum, centered near 250 mb, with an amplitude that is approximately 1.5 times that of the lowest levels. Note this upper level heat flux is not as effective at net heat transport as that of the lower levels, due to the decreased density in the upper levels. The average 1979-80 heat flux shows a single maximum near the surface, extending into the upper troposphere. During 1980-81, a secondary upper-level maxima is again observed, with approximately the same amplitude as the lower one. Above 100 mb, the heat flus is equatorward during this year, a result that is probably due to erroneous data. Note this coincides with the discontinuation of the use of raob data in the upper level analyses.

The climatological mean heat flux in the SH summer, based on the data of Oort (1983), shows a double maximum in the vertical with similar upper and lower level amplitudes. Similar behavior is observed in the NH summer.

5. Momentum flux

Figures 14a-c show the seasonal-mean medium-scale wave momentum fluxes, with positive values again denoting equatorward transport. The maximum time-mean momentum flux is poleward, centered near the tropopause and somewhat equatorward of the corresponding jet core. A zero line is found 5-10 degrees poleward of the jet core, with a smaller, equatorward transport found further poleward. This configuration produces time-mean convergence of westerly momentum, tending to reinforce the jet structure. Note the position of the zero line

changes in a manner similar to interseasonal changes in the jet posi-

tion. The overall structure is more consistent from year-to-year in

comparison to that of the heat flux. These observed values are in good

agreement with the climatological means of Oort (1983).

D. Latitudinal and Vertical Confinement

It is observed that the wave activity is conserved when Rossby

waves propagate, but where can the waves propagate? This section will

show how the mean wind structure may confine waves that would other-

wise propagate meridionally and/or vertically.

To understand the general nature of this problem, the assumption

is made that variations in the zonal mean flow are slow over the scale

of the wave. (This assumption does not strictly apply here, as we have

seen that the latitudinal and vertical variations of the waves have

similar scales to those of the zonal mean. We will, however, proceed

under this assumption and be guided by general results.) We can then

apply Liouville-Green or WKB theory to the perturbation potential

vorticity equation (Equation 2). A constant stability (N^2) is as-

sumed, and a traveling wave of the form

$$\psi'(x,y,z,t) = \phi'(y,z) \, \exp(\frac{z}{2H}) \, \exp(ik(x-ct))$$

where $i = \sqrt{-1}$. Transforming coordinates as in Palmer (1982), an

equation is obtained for $\phi'(y,z)$:

$$\frac{\partial^2 \phi'}{\partial y^2} + \frac{\partial^2 \phi'}{\partial z^2} + m^2 \phi'(y,z) = 0 \qquad (16a)$$

$$\text{with} \quad m^2 = \cfrac{\left(\cfrac{\overline{q}_y}{(\overline{u} - c)} - \cfrac{f^2}{4H^2N^2} - \cfrac{k^2}{r^2 \cos^2 \theta} \right)}{\sin^2 \theta} \quad (16b)$$

This equation is analogous to a two-dimensional wave equation, with m^2 analogous to a refractive index (squared). Regions with $m^2 > 0$ will permit propagation, while those with $m^2 < 0$ indicate an evanescent solution, that is the amplitude will decay exponentially with distance. Rossby waves will be refracted toward regions of large refractive index (and away from smaller values), analogous to Snell's law in optics. This theory breaks down near critical lines, where the waves' zonal phase speed c is equal to the zonal wind ($c = \overline{u}$). Rossby wave dynamics near critical lines are not well-understood. Generally, the critical lines are thought to act as reflectors or absorbers for Rossby waves.

Figures 15a-c show meridional cross sections of the refractive index (m^2) for three typical combinations of medium-scale wavenumber and phase speed, based on the seasonally-averaged zonal mean wind field during 1979-80 (Figure 4b). Regions of negative m^2 are shaded. A critical line is formed in each case where $\overline{u} = c$, restricting wave propagation to a more limited region for faster moving waves. In particular, vertical propagation is prohibited because of stratospheric easterlies above about 50 mb. Regions of small $\overline{q}_y$ above and on the poleward side of the jet suggest that waves may be restricted from this region. On the other hand, large values of $\overline{q}_y$ in the mid-troposphere result in a favored region for wave propagation, possibly forming a type of Rossby wave guide.

Equation 16b and Figures 15a-c suggest that longer waves (smaller

(a)

(b)

(c)

PRESSURE (MB)

LATITUDE SOUTH
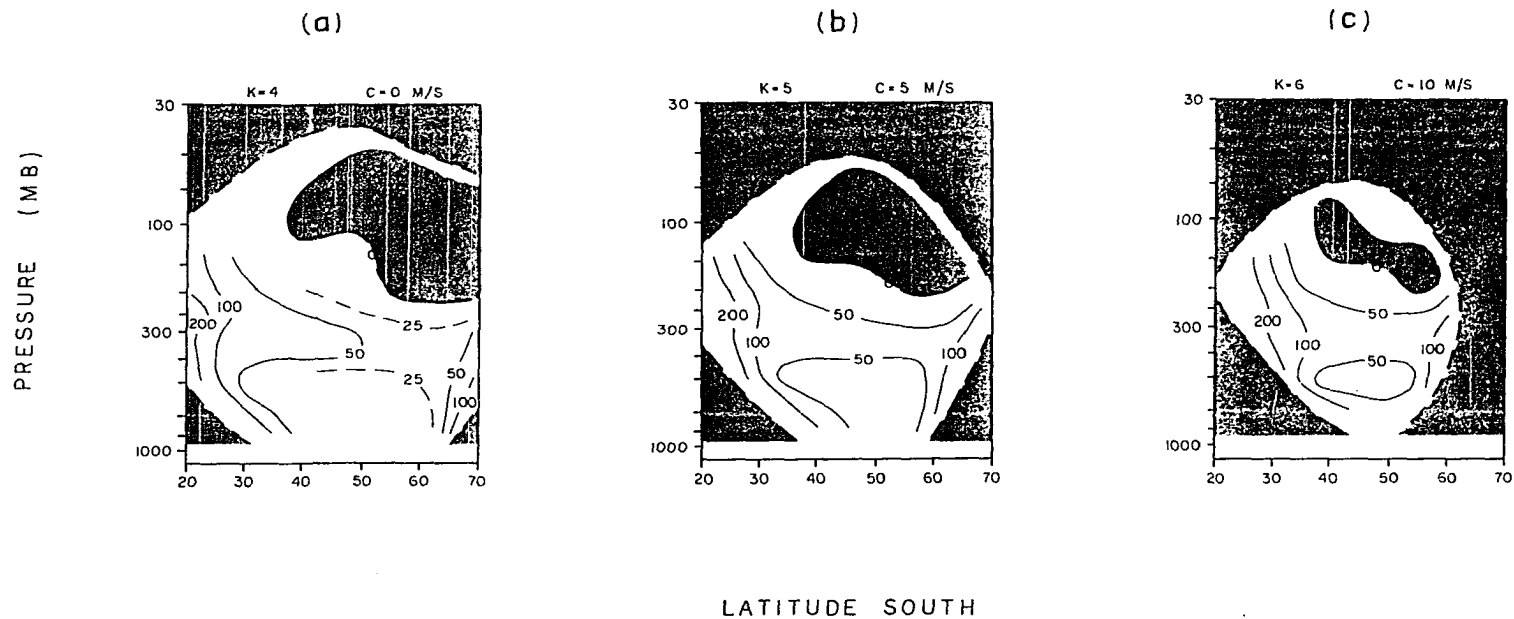
Figure 15. Values of 'refractive index' squared (m^2), based on 1979-80 average zonal mean wind field, for three combinations of wavenumber (k) and phase speed (c). a) k = 4, c = 0 m/s, b) k = 5, c = 5 m/s, c) k = 6, c = 10 m/s. Heavy dashed line in each figure is the critical line, where $\bar{u}$ = c. Shaded regions indicate negative m^2 where propagation is inhibited. Units of m^2 are $10^{-12}m^{-2}$

51

wavenumber k) will propagate relatively higher into the atmosphere than shorter ones. This can be tested by comparing the vertical structure of individual wavenumbers. Figure 16 shows seasonally-averaged temperature amplitudes at 45°S latitude for waves 4 through 7 individually, normalized by the maximum amplitude of each wave. The upper level (30-70 mb) results clearly show that wave 4 extends relatively higher into the atmosphere than wave 5, which extends higher than wave 6, etc. The time-average wave structure thus reflects the characteristics that are expected due to the structure of the background wind field. Note that variations in the zonal wavenumber are perhaps not the most important factor, as the refractive index is more critically dependent on the zonal phase speed. The next section will show that shorter waves generally move faster, and these two effects combine to produce the results seen in Figure 16.

E. Zonal Phase Progression

The latitudinal and vertical phase structure of the medium-scale waves changes as the waves grow and decay, or as they propagate through regions of different wind shear and curvature. In contrast to the vascillating nature of these phase changes, the zonal phase of the waves is observed to change monotonically in time. The wave 6 features in Figures 7a-c are observed to move eastward in time, at a rate of approximately 7 degrees longitude per day — a phase speed near 10 m/s in midlatitudes. This behavior is expected of Rossby waves.

The Rossby wave dispersion relation, Equation 4, shows that these
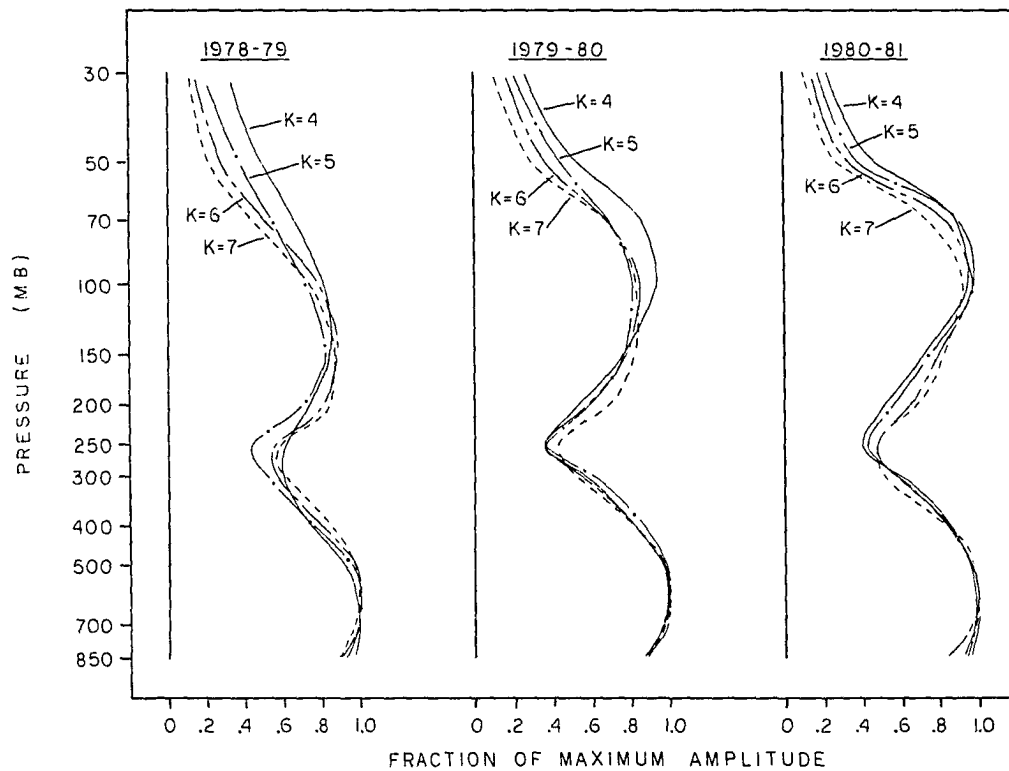
Figure 16. Comparison of the seasonally-averaged vertical
temperature structure for individual wavenumbers.
Plotted is the ratio of temperature amplitude at
each pressure level to the maximum value for each
wavenumber. Note that lower wavenumbers reach
relatively higher into the atmosphere

waves are dispersive: shorter scale waves travel more slowly towards
the west (in the absence of zonal wind). In the presence of a zonal
mean current, the phase speed of Rossby waves are changed in two ways:
1) They are Doppler shifted by the wind, and 2) the northward potential
vorticity gradient ($\bar{q}_y$ in the dispersion relation) is modified by the
zonal wind structure. The Doppler shifting results in shorter scale
waves moving faster towards the east. This characteristic is clearly
exhibited by the medium-scale waves studied here.

Several different methods of studying the zonal phase progression
are possible. Plots of the longitudinal phase vs. time clearly show
the phase progression, but contain no information concerning wave
amplitude. A method which has been used extensively in the past decade,
space-time spectral analysis, incorporates information on the wave
amplitude and separates the wave variance into eastward and westward
propagating waves. This is a statistical approach, assuming constant
wave structure over the time sample length, so that waves which change
in time are not accurately represented. The use of Hovmöller plots for
a band of wavenumbers shows time changes in the phase and amplitude of
the waves, along with information on their zonal structure (to the
degree that can be resolved within the wavenumber band used). These
latter two methods will be applied to the medium-scale waves to il-
lustrate the wave characteristics, along with differences in the analysis
techniques.

1. Space-time spectral analysis

The application of space-time spectral analysis is a statistical

approach to the study of traveling waves in the atmosphere. An extensive

body of literature has been devoted to the development and application

of this technique to atmospheric waves, a summary of which may be

found in Hayashi (1982) and references therein. Briefly, the time

variation for a particular zonal wavenumber is partitioned into east-

ward and westward propagating waves, based on the correlation between

time-dependent zonal sine and cosine coefficients (which for pure

traveling waves are always 1/4 cycle out of phase).

Following Hayashi (1977), consider the time-dependent meridional

wind at a particular pressure and latitude:

$$v(x,t) = \sum_{k} VS_k(t)\ \sin(kx) + VC_k(t)\ \cos(kx)$$

Here VS_k and VC_k are the Fourier sine and cosine coefficients. The

meridional wind variation may also be written as the sum of eastward

$(+\omega)$ and westward $(-\omega)$ propagating waves:

$$v(x,t) = \sum_{k} \sum_{\omega} V_{k,\pm\omega}\ \cos(kx \pm \omega + \alpha_{k,\pm\omega})$$

where $\alpha_{k,\pm\omega}$ is the relative phase. Equating the two representations,

the power per unit frequency associated with eastward or westward

traveling waves (space-time power spectral density, or simply power

spectra) is then given by:

$$P_{k,\pm\omega} = \frac{1}{4}\ (P_\omega(VC_k) + P_\omega(VS_k) \pm 2 \cdot Q_\omega(VC_k, VS_k))$$

where $P_\omega(VC_k)(P_\omega(VS_k))$ is an estimate of the cosine (sine) series

power, and $Q_\omega(VC_k, VS_k)$ is an estimate of the quadrature spectrum

between $VC_k(t)$ and $VS_k(t)$. The quadrature spectrum is a measure of

the phase difference between $VC_k(t)$ and $VS_k(t)$. For finite-length

data sets, both the power and quadrature spectral estimates are given

for discreet frequency ω, but represent the estimates in a band $\Delta\omega$

centered at ω. The bandwidth $\Delta\omega$ depends on the analysis technique.

In this study, spectral power is estimated using the lag-correlation

technique (Bendat and Piersol, 1971). Time series of length 90 days

were analyzed using a maximum lag of 18 days. The resulting spectral

estimates are centered at frequencies

$$\omega_n = n/36 \ (\text{days}^{-1}) \quad n = 1, \ 2, \ \ldots, \ 18$$

with a resulting spectral bandwidth ($\Delta\omega$) of 1/18 (day^{-1}). The re-

sulting spectral estimates are hanned (1/4, 1/2, 1/4 convolution in

frequency) to reduce leakage, which is caused by the finite length of

the data set. This procedure is equivalent to the application of a

standard Tukey window to the lag correlation estimates. A convenient

method of displaying the power spectrum is by contour plotting versus

zonal wavenumber and frequency (or period).

Space-time power spectral density of the meridional geostrophic

wind at 45°S latitude and 200 mb for each of the three seasons is

shown in Figures 17a-c. Almost all of the power is found in the medium-

scale wave regime each year. The general contour patterns are similar

for each season: an elongated power density oriented from waves 3-4

with very long periods, to waves 7-8 moving eastward with periods near
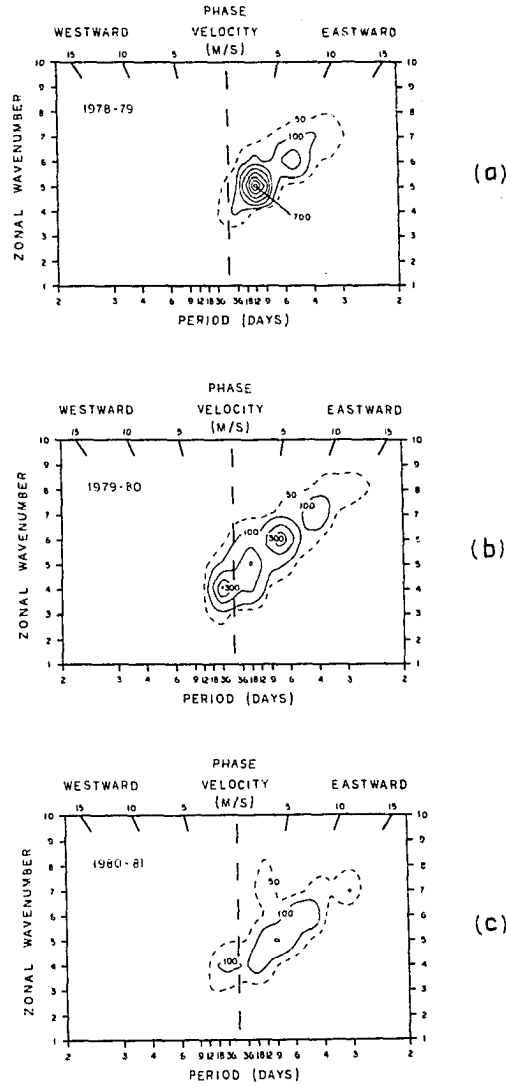
Figure 17. Space-time spectral power density of geostrophic
meridional wind at 45°S latitude and 200 mb for
a) 1978-79, b) 1979-80, c) 1980-81. Power units
are m^2/s^2 $1/\Delta\omega$, with contour intervals (solid
lines) of 100 m^2/s^2 $1/\Delta\omega$

3-4 days. This structure is in good agreement with the results of Fraedrich and Kietzig (1983), who studied 5 summers in the SH (1959-64) based on geopotential heights published by the South African Weather Service. They also demonstrated that these results agree qualitatively with the Rossby dispersion relation.

Year-to-year differences in power spectra are significant. During 1978-79, wave 5 exhibits a remarkably strong peak, corresponding to eastward movement with period near 12 days. A second peak is found, corresponding to an eastward moving wave 6 with a period near 5 days.

The 1979-80 power spectra is less concentrated in wavenumber-frequency space. Four maxima are observed, corresponding to waves 4 (long period westward) through 7 (4 day period eastward). The eastward moving wave 6 feature in Figures 7a-c is embedded in the power peak seen for wave 6 with period between 6-9 days.

The 1980-81 season exhibits a power spectra similar to that of 1979-80, though with smaller overall power and lack of any distinct peaks. This lack of power (in comparison to the other seasons) is in agreement with the time-averaged energy spectrum, Figure 8, which shows the 1980-81 summer to be rather quiet.

2. Hovmöller diagrams

Space-time spectral analysis is a powerful tool for examining seasonal statistics. A major drawback is that waves that change in time cannot be accurately resolved. A way to study the time evolution of wave structure is with the use of Hovmöller diagrams. A Hovmöller diagram is a two-dimensional contour plot with time as one axis, and,

for our use of studying the zonal phase progression, longitude as the

other axis. In order to study just the medium-scale waves, Hovmöller

plots of the meridional wind for waves 4 through 7 at 200 mb and 45°S

latitude are shown for each of the three seasons in Figures 18-20.

In addition, the time-average medium-scale wave is plotted at the

bottom of each figure. Each of these plots contains an enormous

amount of information on the medium-scale waves, and we will consider

them separately.

a. 1978-79   Wave 5 is the predominant feature seen in Figure 18,

usually moving eastward with a regular period near 12 days. Note the

regular downstream development (or redevelopment) of existing wave

structures — in some cases, wave maxima and minima can be traced

continuously around the globe. The zonally-symmetric patterns indicate

that the wave is at times global in nature, rather than a longi-

tudinally isolated wave packet of the same scale as wave 5. This be-

havior results in the sharp spectral peak for wave 5 found in Figure

17a.

The waves are sometimes observed to exhibit slower phase progres-

sion — the most notable case is during January 1-10 (days 30-40).

This slowing is most often noticeable near 90°W longitude, and this is

the region of the largest time-mean wave amplitude (see bottom Figure

18). Wave amplitude is large during the times of slow phase progres-

sion, or when it is in phase with the time-mean wave. This situation

suggests a) stationary-transient wave interference, and/or b) region(s)

of preferred wave amplification. It will be shown (based on a study

of the wave energetics) that this correlation is due to wave inter-
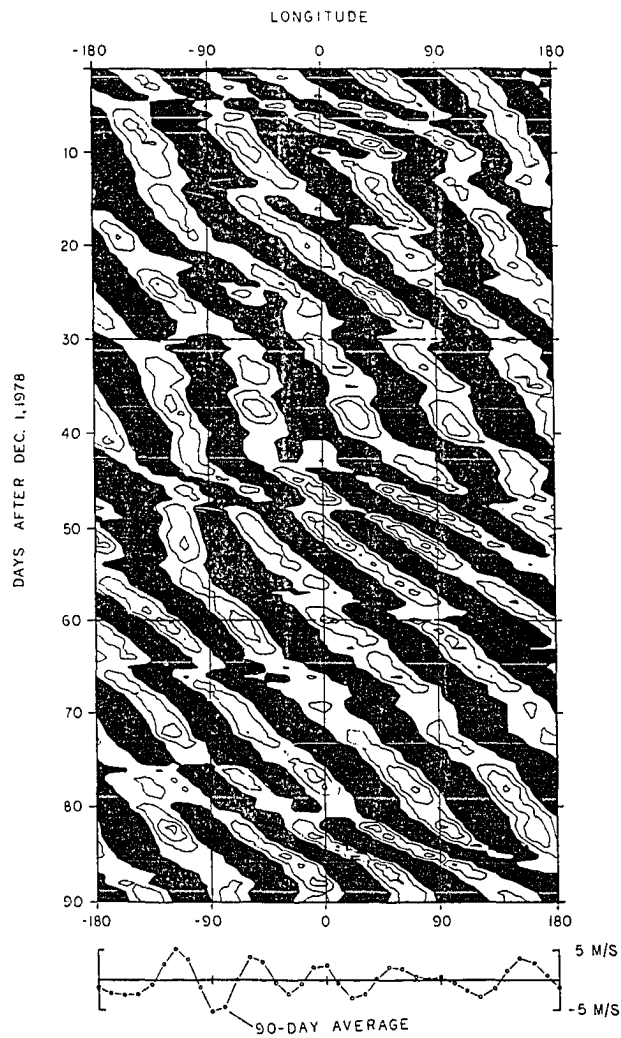
Figure 18. Hovmöller diagram (longitudinal phase vs. time plot) of the meridional wind at 45°S latitude and 200 mb during 1978-79, constructed using zonal wavenumbers 4-7. Contour interval is 10 m/s, with shaded winds southward. 90-day average is plotted at the bottom
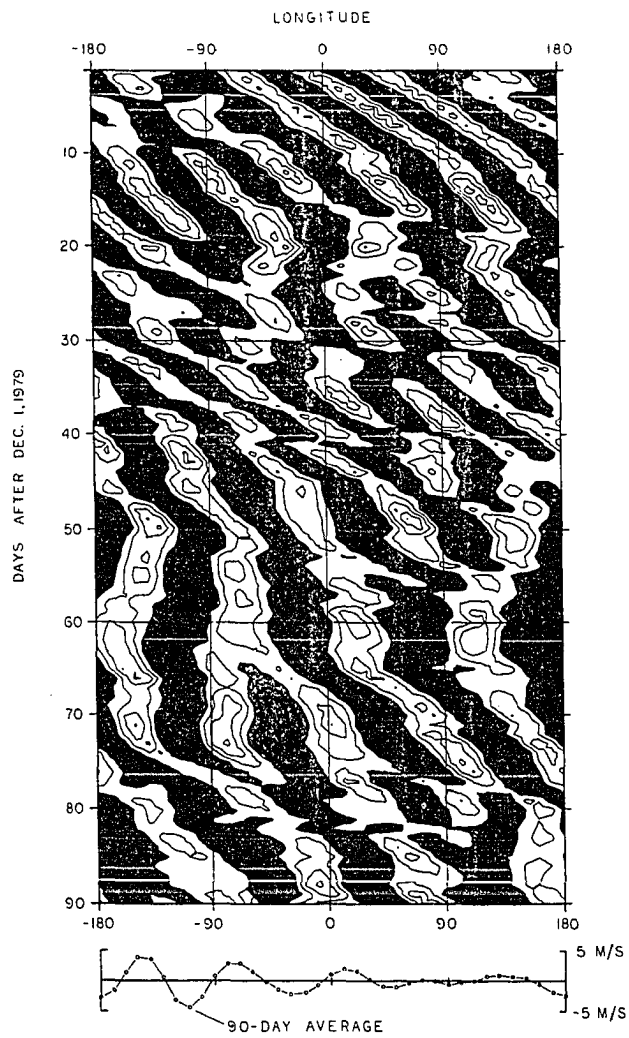
Figure 19. As in Figure 18, but for 1979-80
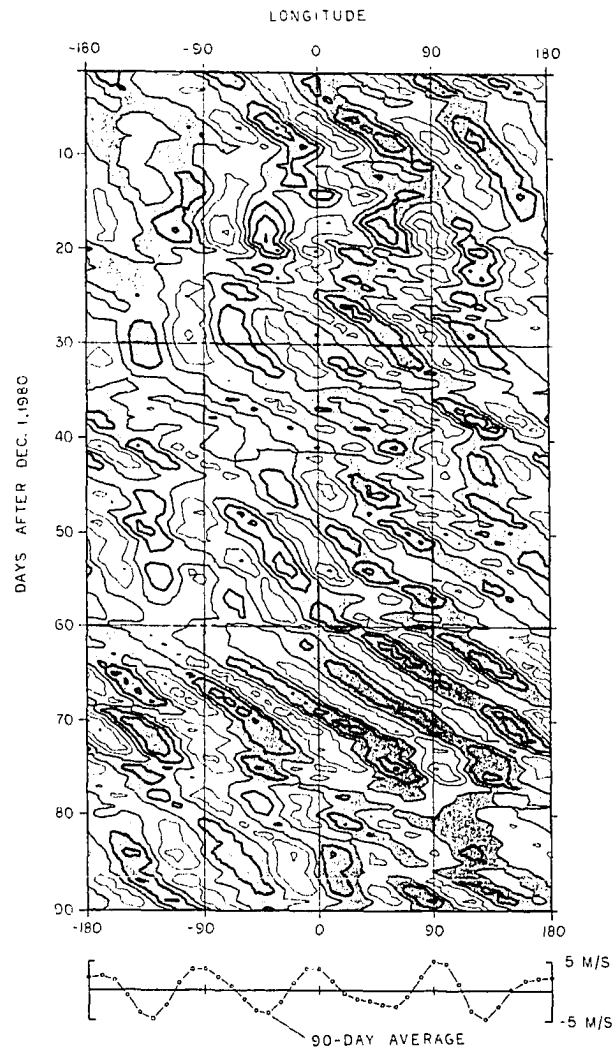
Figure 20. As in Figure 18, but for 1980-81

ference, the subject of a later chapter. (The structure of the time-mean waves will also be discussed there.)

On three separate occasions, shorter waves (waves 6-7) predominate in the region between 0-90°E longitude, the region of the strongest jet (see Figure 6a). These structures occur during days 1-10, 45-55, and 80-90. These features are more longitudinally localized, and exhibit considerably shorter periods near 5 days. It is interesting to note that there is an approximate 40-day periodicity between these events, because there has recently been much interest in large-scale atmospheric oscillations with a 40-50 day period (for example, Lau and Phillips, 1984).

b. <u>1979-80</u>   The same general eastward phase progression for the medium-scale waves is observed in Figure 19, though the overall structure is not nearly as orderly as that of Figure 18. Downstream development of existing waves is also apparent in this figure. The wave 6 features of Figures 7a-c are seen near the top of the figure (between days 10-15), and regular eastward phase progression is clearly observed. This case appears to be a globally symmetric feature, very similar to baroclinic waves observed in laboratory annulus experiments (Pfeffer et al., 1980).

Near the end of January (day 55), a strong wave 4 pattern develops, remaining globally quasi-stationary for a week, and for 3 weeks near 90°W longitude. During this time period, the medium-scale wave energetics exhibit wave interference characteristics similar to those of 1978-79. This case will also be discussed in the interference section.

c. <u>1980-81</u>   Figure 20 shows similar medium-scale wave charac-
teristics to those exhibited during the other years: general eastward
phase progression and downstream development of existing wave features.
Most features observed are longitudinally localized, though the wave 6
feature during the first 10 days of February (days 60-70) does exhibit
a global nature.

3.   <u>Summary of zonal propagation characteristics</u>

Two methods of studying the zonal phase propagation characteristics
of the medium-scale waves have been shown and compared. Space-time
spectral analysis demonstrates the dominant nature of the medium-scale
waves, and shows that they obey the Rossby dispersion relation. The
use of Hovmöller diagrams allows the study of the time evolution of
wave structure, showing remarkably regular eastward phase progression
and frequent downstream development of existing medium-scale wave
patterns. The medium-scale waves at times appear to be longitudinally
localized features; at other times, they resemble truly global-scale
modes. Significant year-to-year variability is observed. Inter-
hemispheric comparisons (Yu et al., 1984) indicate that such global-
scale characteristics are not observed in NH medium-scale waves.

The important question of the forcing mechanism(s) of the medium-
scale waves, as determined by their energetics, is the subject of the
next chapter.

V. ENERGETICS

The conservation of energy is a fundamental constraint on atmospheric motions. This section will focus on characterizing the forcing mechanism(s) of the medium-scale waves and their interaction with the zonal mean flow, based on a study of their energetics. This study will be based on the energy equations for the waves and zonal mean flow (Equations 12-15). These equations show that (in the absence of direct forcing or dissipation), the energy gained by the waves is lost by the zonal mean, and vice-versa. This balance will be tested here, and shown to be valid. By inspection of the baroclinic and barotropic terms individually, and with the use of Eliassen-Palm diagrams, the nature of the wave - mean-flow interaction can be elucidated.

The energy equations will be applied and analyzed in two ways. For studying the various balances, the longitudinally averaged and vertically integrated (hereafter simply integrated) energy and energy conversions are calculated. Latitudinal averages are taken over 25 to 65°S latitude, while the limits of vertical integration are from 850 to 50 mb. The numerical procedure is described in the data analysis section. To closely analyze the interactions, meridional cross sections of time-mean values will show where the main contributions to these integrated results come from. As with other time averages, these must be interpreted in terms of the constantly changing wave structure. A case study of wave growth and decay will detail how the wave structure changes in time.

In order to establish and quantify the association between two

time series $x(i)$ and $y(i)$ with $i = 1, 2, \ldots, N$ (wave energy and zonal

mean energy, for example), the linear correlation coefficient at lag

τ, $r(\tau)$, is calculated and displayed on graphs or tables where two time

series are compared. $r(\tau)$ is given by

$$r(\tau) = \frac{1}{N-1} \sum_{i=1}^{N} \frac{(x(i) - \tilde{x}) \cdot (y(i) - \tilde{y})}{\sigma_x \cdot \sigma_y}$$

where σ_x and σ_y are the standard deviation of the respective series,

and $\tilde{x}$ and $\tilde{y}$ are the respective means.

A problem arises in the use of this statistic when significant

auto-correlations exist for each time series, as is frequently the case

in meteorological investigations. This problem, also known as

persistence or the presence of red noise, can result in nonzero cor-

relation when the two series are actually independent. To establish

significance levels for the correlations presented here, the analysis

of Lau and Chan (1983) is followed. They show that the standard devia-

tion of $r(\tau)$ is given by

$$SD(r(\tau)) = \left[\frac{2}{(N - |\tau|) \cdot (1 - \exp(-(\lambda_x + \lambda_y)))} \right]^{1/2}$$

where λ_x and λ_y are the inverse of the auto-correlation e-folding times

for each series. Auto-correlations for several time series presented

here were used to estimate λ, resulting in an approximate value of

$\lambda \simeq 0.4$. Assuming $\lambda_x \sim \lambda_y$, this suggests that $SD(r(\tau)) \simeq .20$, or

$|r(\tau)| > .40$ are required for significance at the 95% confidence level.

This number is only a general guide — the correlations presented

are usually quite apparent to the eye.

A. Seasonally-Averaged Zonal-Mean and Wave Energy

The seasonal-mean total wave energy (KE + APE) spectrum shown in
Figure 8 clearly shows that the transient medium-scale waves possess
the largest amount of energy during each season (in agreement with re-
sults of the space-time spectral analyses, which are calculated for a
single latitude and pressure). Wave 5 is the preferred scale during
1978-79, while the spectra for 1979-80 and 1980-81 peak at wave 4.
This spectrum is quite different from that in the NH (see, for example,
Wiin-Nielsen, 1967), where ultra-long waves (k = 1-3) contain the
maximum energy. The approximate k-3 dependence found for the higher
wavenumbers is in agreement with energy spectra for the NH (Wiin-Nielsen,
1967), and is predicted for two-dimensional turbulent energy cas-
cade outside the region of forcing (Charney, 1971).

Guided by the above knowledge, the energetic analyses presented
here are divided into 3 wave bands: k = 1-3 (ultra-long quasi-stationary
waves), k = 4-7 (medium-scale transient waves), and k = 8-12 (shorter
scale, smaller amplitude waves). The exact wavenumber cutoffs are
somewhat arbitrary — these choices were made as a result of considering
the overall wave characteristics.

Table 1 shows each of the three seasonal means of KE and APE for
each of the wave bands, along with the zonal mean energies. Values in
parentheses are the ratio of APE to KE for each wave band. Since the
intensity of the circulation changes from year-to-year, this ratio
will be a measure of the relative sizes of these terms.

Similar magnitudes and ratios are observed for the energies for

Table 1. Seasonal averages of zonal mean and wave kinetic energy
(KE) and available potential energy (APE), with values in
10^5 J/m^2. Values in parentheses are the (dimensionless)
ratio of APE to KE for each wave band

Season	Zonal mean		k = 1-3		k = 4-7		k = 8-12	
	KE	APE	KE	APE	KE	APE	KE	APE
1978-79	9.7	16.0	2.0	1.4 (.68)	3.4	1.4 (.42)	1.4	0.3 (.23)
1979-80	9.7	16.3	2.3	1.4 (.60)	3.5	1.4 (.38)	1.5	0.3 (.22)
1980-81	9.2	16.5	2.1	1.3 (.62)	2.9	1.3 (.43)	1.1	0.3 (.24)

each season, though the wave energy during 1980-81 was markedly smaller,
as noted previously. Note the ratio of wave APE to wave KE decreases
along with the horizontal scale of the wave. This can be understood
as follows: if all the waves have similar vertical scales (on the
order of the scale height), the ratio APE/KE is approximately

$$(\frac{f}{N})^2/H^2K^2$$

where K^2 is the total horizontal wavenumber (squared). Shorter waves
(larger K) thus have relatively less APE than longer ones.

The magnitude of the zonal mean APE is considerably less here in
comparison to other global energetic studies (where it is of order 30-40
x 10^5 J/m^2). This is due to the definition of APE as the latitudinal
variance of the zonal mean temperature, and the fact that the limited
latitudinal domain (25-65 degrees) considered here simply chops off
much of this variance. Good agreement in the balances of wave and

zonal mean energy (in time) support these latitudinally restricted APE

calculations.

Cross sections of the seasonal-mean medium-scale wave KE and APE

are shown in Figures 21-22a-c. At the bottom of each figure is the

integrated value of the energy, in agreement with Table 1. Note that

since most of the mass is in the lowest levels, the later are weighted

the most in the integrations. The KE cross sections show a single

maximum in the upper troposphere, similar in structure to that of the

wave amplitude. The APE cross sections display a double maxima, cor-

responding to the two maxima for wave temperature fluctuations observed

in Figures 12a-c. Even though the amplitudes of the temperature

fluctuations are similar, the APE in the lower maximum is much larger

than that in the upper, due to the lower static stability in the

troposphere. In addition, the higher density results in the lower

maximum contributing approximately ten times as much as the upper to

the integrated total.

B. Time Variations

The objective for this section is to study the time-variations in

the integrated zonal-mean and medium-scale wave energetics, along with

the wave - mean-flow interactions. After describing the energetic scheme,

it will be shown that changes in the medium-scale wave and zonal-mean

energies are often complementary, and that the flow vacillates between

highly perturbed and zonally symmetric configurations.

The observed zonal-mean and medium-scale wave energy changes are
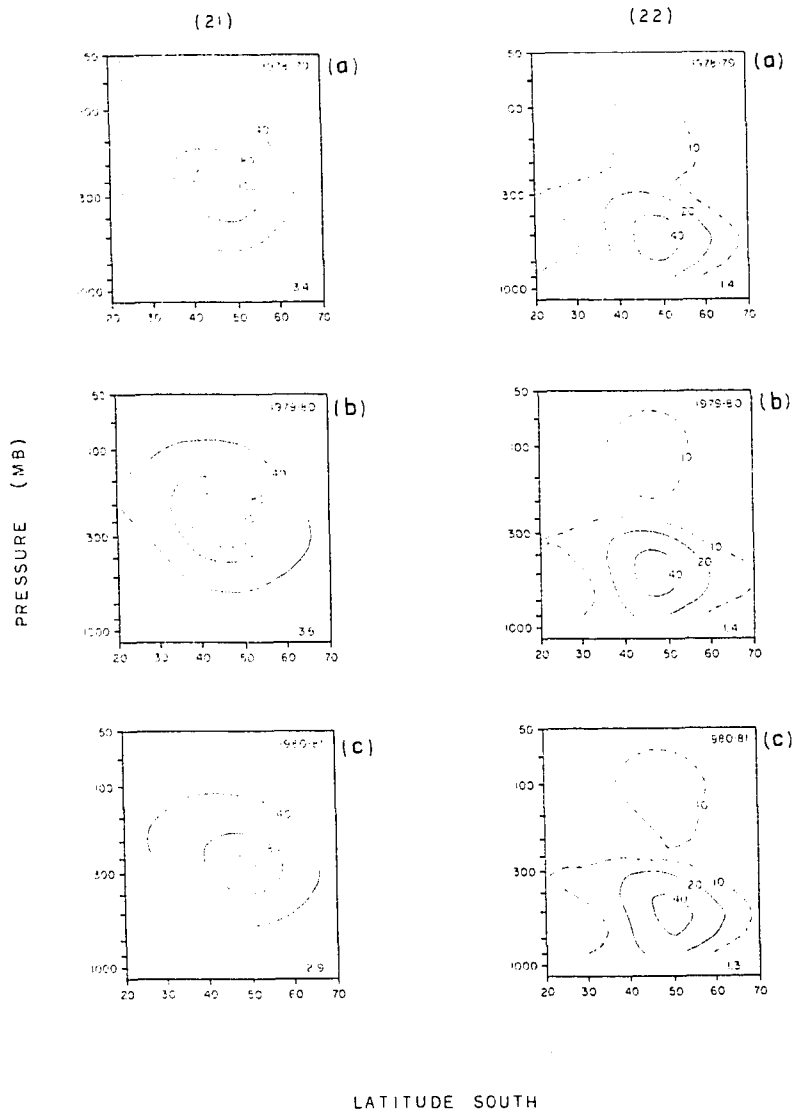
Figure 21. Seasonally-averaged medium-scale wave kinetic energy (m^2/s^2). Numbers in lower right hand corner are integrated total, in 10^5 J/m^2. a) 1978-79, b) 1979-80, c) 1980-81

Figure 22. Seasonally-averaged medium-scale wave available potential energy (m^2/s^2). Numbers in lower right hand corner are integrated total, in 10^5 J/m^2. a) 1978-79, b) 1979-80, c) 1980-81

found to be well-correlated with those predicted due to wave – mean-flow

interactions (calculated as in Equations 14 and 15). This correlation

is studied both for the integrated results and for each particular

latitude and pressure. This agreement prompts the analysis of these

interactions in terms of their separate baroclinic and barotropic

contributions, thus determining the forcing mechanism(s) of the medium-

scale waves.

1. Description of energetic scheme

This section details the proposed wave – mean-flow energy balance

used in the rest of this section. Time variations of the integrated

zonal mean KE and APE are shown for each season in Figures 23a-c.

Variations in APE are observed to be coincidental with variations in

KE, reflecting the thermal wind balance between the zonal mean tempera-

ture gradient and the zonal mean vertical wind shear. Although these

quantities are frequently treated separately in energetic studies,

here they are combined to simplify the discussion. The result is

called simply the zonal mean energy $\bar{E}$. Figures 24a-c show the

integrated KE and APE for waves 4-7 for each season. Since these

quantities are also well-correlated, it is reasonable to combine

them to give the total wave energy E'.

Using the above conventions, the overall balance of energy between

the waves and the zonal mean flow can be represented in a schematic

energy diagram, shown in Figure 25. This simplified view of the energy

cycle neglects energy transport into or out of the area of interest,

and other nonconservative source/sink terms. It does, however, contain
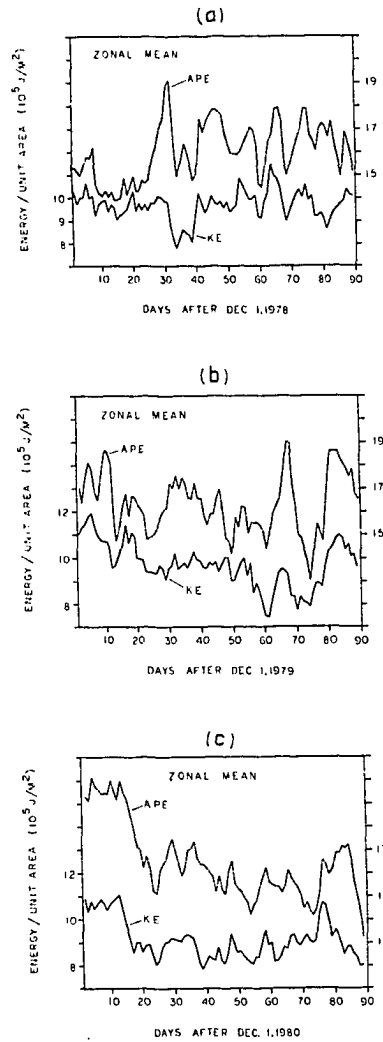
Figure 23. Time variations in zonal mean available potential
            energy (APE) and kinetic energy (KE) for a) 1978-79,
            b) 1979-80, c) 1980-81
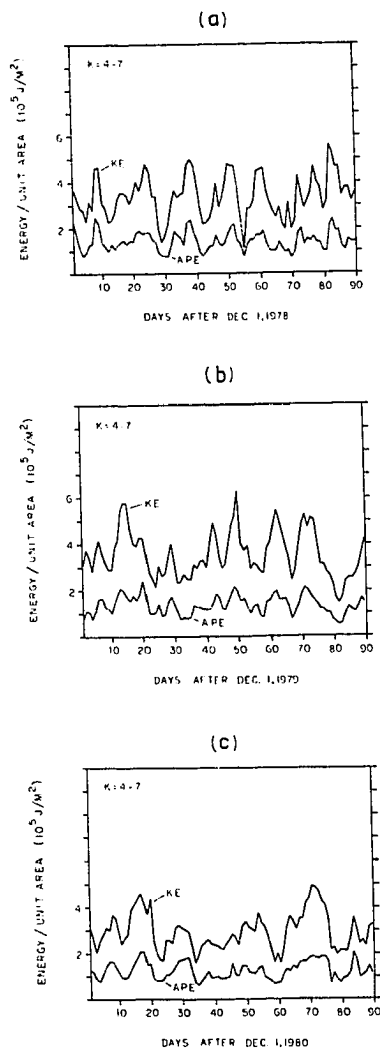
Figure 24. Time-variations in medium-scale wave (k = 4-7)
available potential energy (APE) and kinetic energy
(KE) for a) 1978-79, b) 1979-80, c) 1980-81

GENERATION $\longrightarrow$ | $\overline{E}$ ZONAL MEAN ENERGY | $\overline{U}\cdot DF$ $\longleftrightarrow$ | E' WAVE ENERGY | $\longrightarrow$ DISSIPATION
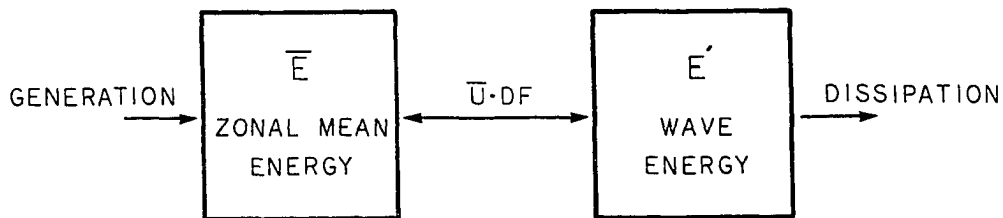
Figure 25. Schematic zonal mean and medium-scale wave energy
diagram. $\overline{U}\cdot DF$ is the wave-mean-flow interaction
term (see Equations 14-15). This simplified diagram
neglects energy transport into or out of the area of
interest, and other nonconservative source/sink
terms. This proposed energy balance is in good
agreement with that observed in the Southern
Hemisphere summer atmosphere

the essential wave−mean-flow interaction term $\bar{u}\cdot DF$, and will be shown
to be in good agreement with the overall observed energy balance in the
SH summer.

2. <u>Zonal-mean</u> <u>medium-scale</u> <u>wave</u> <u>energy</u> <u>balance</u>

Time variations in the zonal mean and medium-scale wave energy for
each season are shown in Figures 26a-c. Large variations in each are
observed. (Time variations in the energy of waves 1-3 and 8-12 are
typically much smaller − they will be discussed shortly.) An obvious
feature is that the growth in medium-scale wave energy is usually as-
sociated with a decrease in zonal mean energy. This anti-correlation
is strongest during 1978-79 and 1979-80, and still observed during
1980-81, even though the correlation coefficient is much smaller.
The steady decrease in zonal mean energy between December 10-20,
1980 (accompanied by an increase in the energy of waves 1-3) may be
one cause for the low correlation during this season.

The important point is that energy is fluctuating between the
zonal-mean flow and the medium-scale waves. Physically this means
that the flow is vacillating between highly perturbed and zonally
symmetric states. This situation is clearly illustrated in Figures 27a-d,
which show two days when the flow is dominated by medium-scale waves
(December 24, 1978 and January 7, 1979) and two days when the flow is
largely zonal (December 30, 1978 and January 12, 1979). These days
correspond to days 24, 38 and 30, 43, respectively, of Figure 26a.
These arguments demonstrate that wave-zonal mean exchange is a valid
concept for describing the SH summer atmosphere.
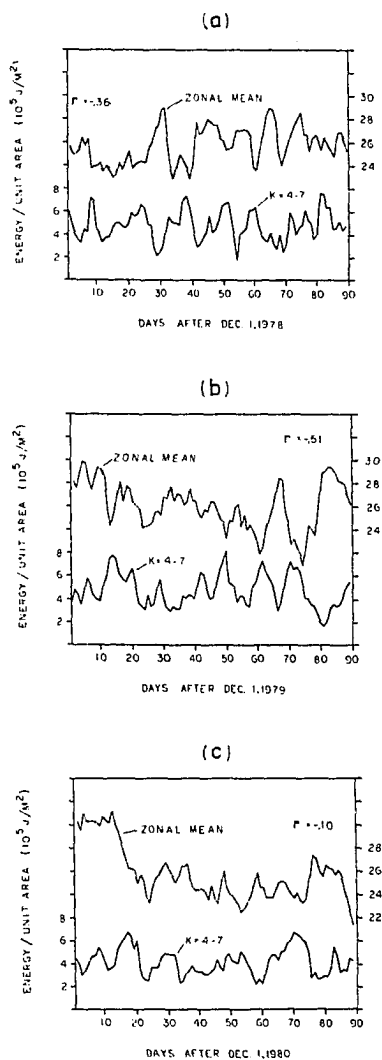
Figure 26.   Time variations in zonal mean and medium-scale wave
(k = 4-7) energy for a) 1978-79, b) 1979-80, c)
1980-81. Linear correlation coefficient (r) is
shown in each figure. A value of r $\gtrsim$ 0.4 is needed
for significance at the 95% confidence level
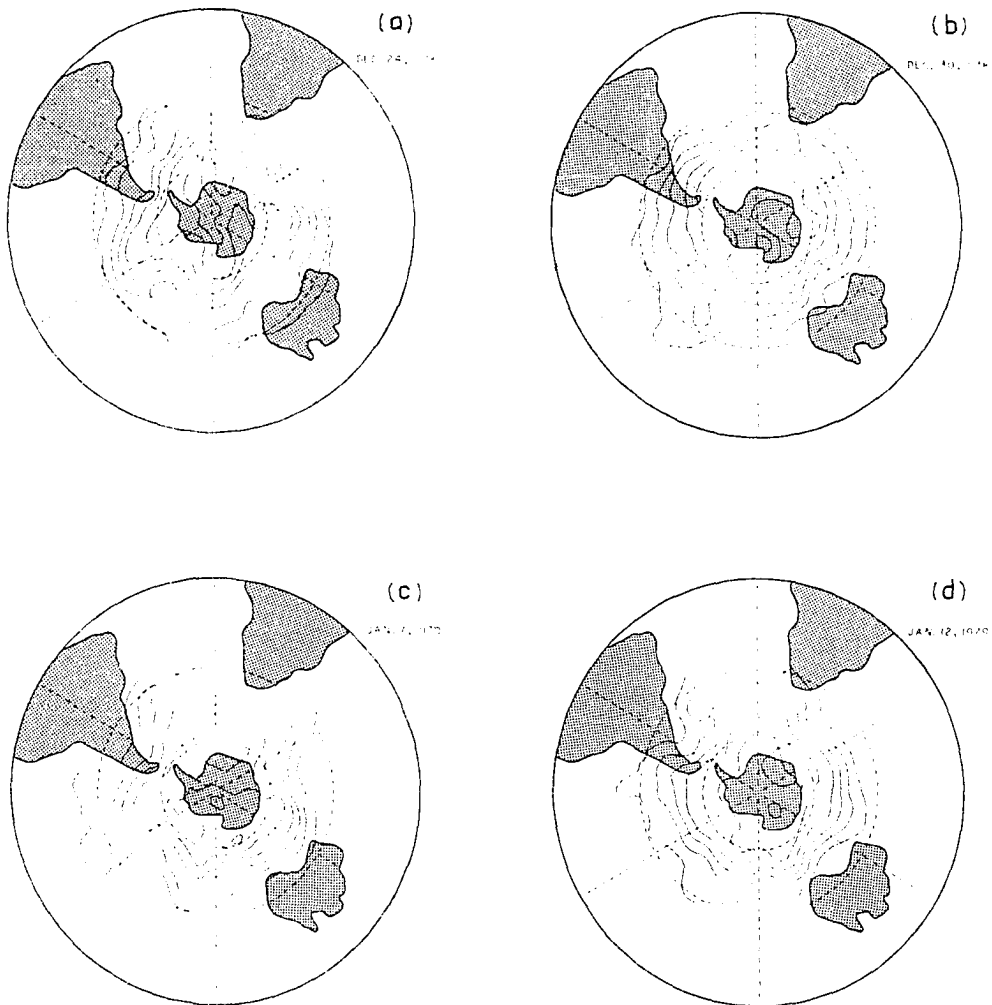
Figure 27. SH polar stereographic projections of the 200 mb
geopotential height contours for two days when the
flow is dominated by medium-scale waves (a and c),
and two days when the flow is zonally symmetric
(b and d). The actual dates are indicated on the
figures; note that the whole sequence (a-d) occurs
in only 20 days. Contour interval is 200 gpm.
Some low-latitude contours have been omitted for
clarity

The next question is: How do the observed time changes in $\overline{E}$ and E'
agree with each other, and with the observed wave — mean-flow interaction
term, $\overline{u} \cdot DF$? Figures 28-30 show: 1) rate of change of medium-scale
wave energy, $\partial E' / \partial t$, 2) rate of change of zonal mean energy, $\partial \overline{E} / \partial t$, and
3) medium-scale wave - mean-flow interaction term, $\overline{u} \cdot DF$, plotted and
correlated in their three possible combinations.

As expected from the time series of $\overline{E}$ and E' just discussed, their
time changes are usually complementary, and a high degree of negative
correlation is observed in the top part of Figures 26-28. The middle
of each figure shows the time changes of $\overline{E}$ along with the medium-scale
wave interaction term (possible values denote loss of zonal mean
energy), the latter calculated from Equation 14b. Significant anti-
correlation is observed during each year: changes in zonal mean energy
may to a large degree be attributed to interactions with the medium-
scale waves. Note that even though the time-changes in these quantities
are of similar magnitude and opposite sign, the time averages are dif-
ferent. That is, while the time average zonal mean energy change is
near zero, the time average of the interaction term is greater than
zero: in the time-average the zonal-mean flow is losing energy to the
medium-scale waves. In the long-term balance, this loss must be com-
pensated by some time-mean generation of zonal mean energy (presumably
due to radiative forcing, as discussed in the Introduction).

The bottom part of Figures 28-30 show the time changes in medium-
scale wave energy, along with the generation of wave energy due to
interactions with the zonal mean flow. The observed high correlations
show that growth and decay of the medium-scale waves can be understood
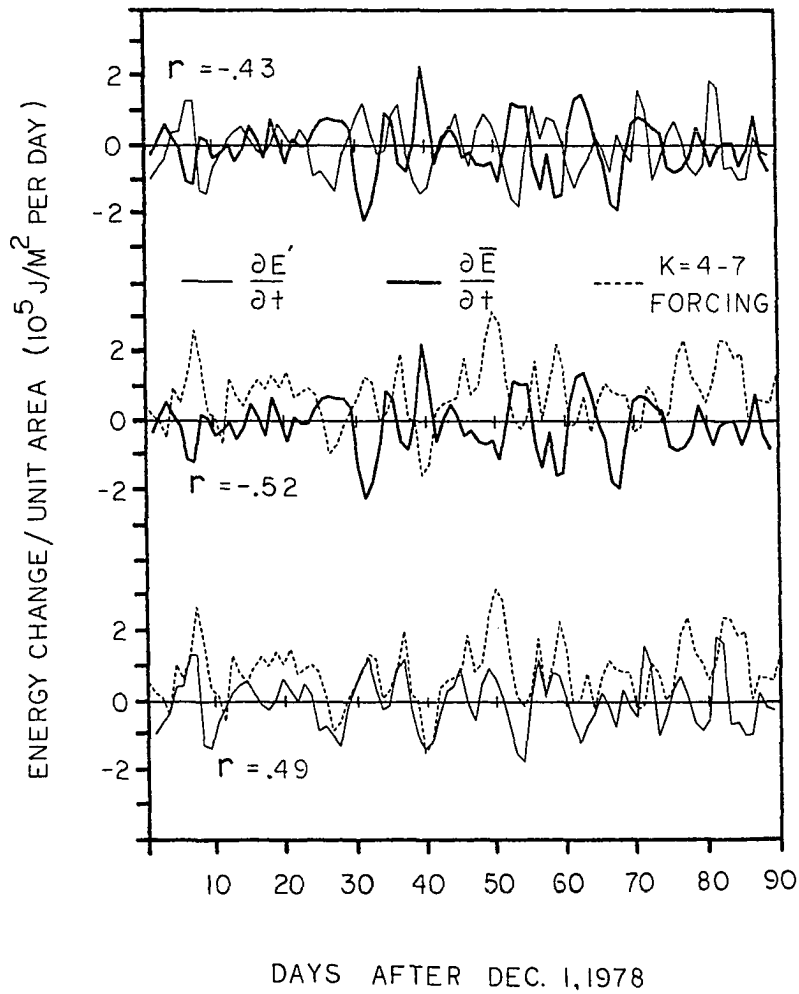
Figure 28. Time rate of change in integrated zonal mean energy ($\partial\bar{E}/\partial t$), medium-scale wave energy ($\partial E'/\partial t$), and zonal mean-medium-scale interaction term (k = 4-7 forcing), given by Equation 14b, plotted in their three possible combinations for 1978-79. Top: $\partial\bar{E}/\partial t$ and $\partial E'/\partial t$; middle: $\partial\bar{E}/\partial t$ and k = 4-7 forcing; bottom: $\partial E'/\partial t$ and k = 4-7 forcing. Linear correlation coefficient (r) is also shown for each part. A value of $r \gtrsim 0.4$ is needed for significance at the 95% confidence level
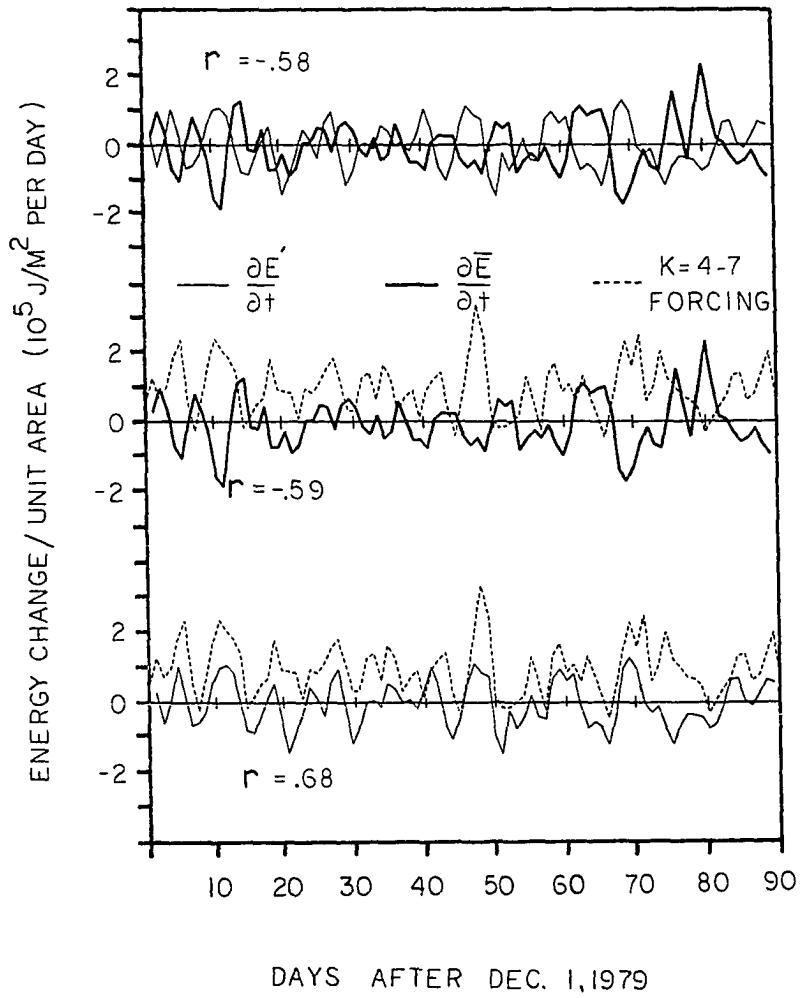
Figure 29. As in Figure 28, but for 1979-80
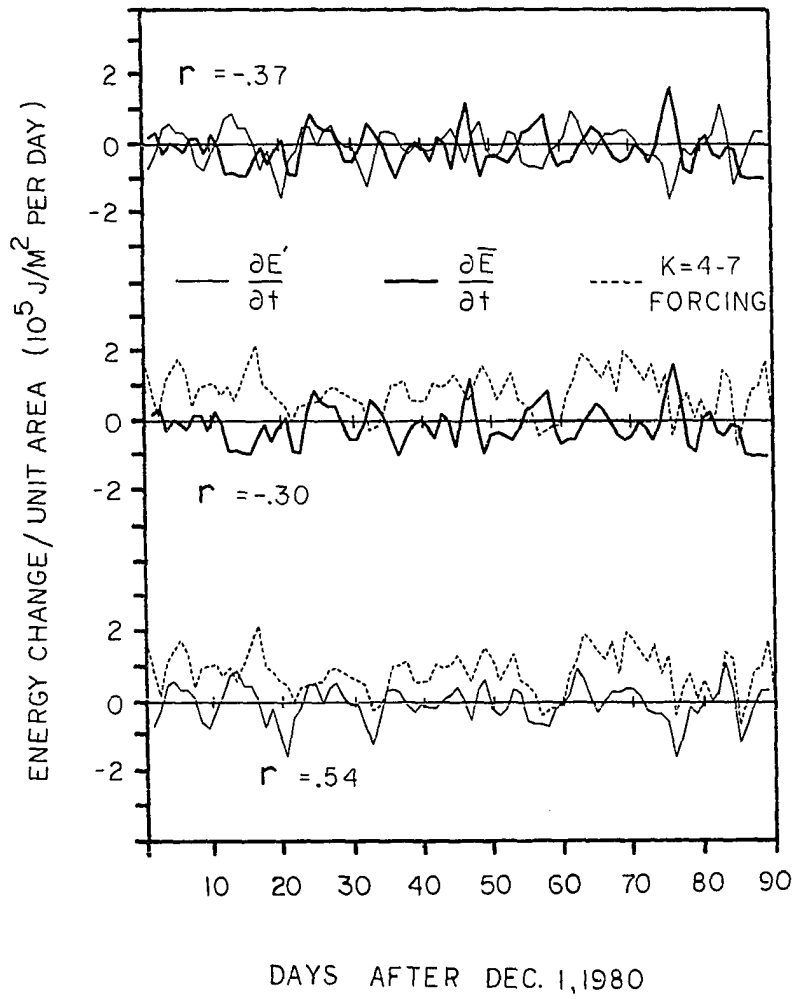
Figure 30.   As in Figure 28, but for 1980-81

in terms of the wave-induced fluxes of heat and momentum, which are central to the interaction term. Note again the time average of wave energy changes are nearly zero, while the wave - mean-flow interaction term has a positive time average. This growth must be balanced by some time mean dissipation of wave energy (approximately equal to the time averaged generation of zonal mean energy).

These results show that the integrated energy changes of the medium-scale waves are compensated by opposing changes in the zonal mean flow, and that this energy exchange can be understood in terms of the integrated wave - mean-flow interaction $\overline{u} \cdot DF$. These results are in good agreement with the schematic energy diagram in Figure 25.

These latitudinally-averaged and vertically integrated results are in good agreement with the proposed energy balance; how well does this zonal average balance work at each particular latitude and pressure? The TEM zonal mean momentum equation is (Equation 8):

$$\frac{\partial \overline{u}}{\partial t} = \overline{fv^*} + DF$$

This shows that zonal mean wind changes are forced by the wave driving term DF, but that the effect of the residual circulation $\overline{v^*}$ must also be taken into account. McIntyre (1982) has shown that the residual circulation will generally tend to mitigate the effect of the wave driving, and that the actual zonal wind changes will be smaller than those anticipated due to DF alone. He has argued that another consequence of the residual circulation is that the response of the zonal wind will tend to be more spread out in the vertical, and narrower latitudinally, than the scale of the actual forcing.

In order to test these ideas, the observed zonal mean wind acceleration ($\partial \bar{u}/\partial t$) and wave forcing (DF) can be calculated for each latitude and pressure. Figure 31a-c show such time series near the jet core for each season. Auto-correlations are significantly smaller for these time series and as a result (following the discussion of Section V.A, lower values of the correlation coefficient r (greater than 0.3) are required for significance at the 95% confidence level. Good correlation is observed, although the magnitude of the forcing is much larger than the observed zonal wind accelerations, as expected from the above discussion. This situation is similar to that observed in the SH winter by Hartmann et al. (1984), who studied this correlation using the wave forcing due to all wave scales.

Meridional cross sections of this correlation coefficient are shown in Figures 32a-c, showing significant correlations throughout much of the mid-troposphere for each season. The best correlations are observed beneath the jet core, near the region of largest zonal-mean potential vorticity gradient ($\bar{q}_y$). The correlations are not large in either the lower troposphere (below 700 mb) or in the lower stratosphere (above 150 mb), where $\bar{q}_y$ is small. This behavior is similar to that in the SH winter shown by Hartmann et al. (1984), who also noted significant correlations in the upper stratosphere (above 10 mb), which they attributed to ultra-long wave processes. The overall continuity exhibited here throughout the region of strongest zonal flow strengthen confidence in the integrated energetic results.
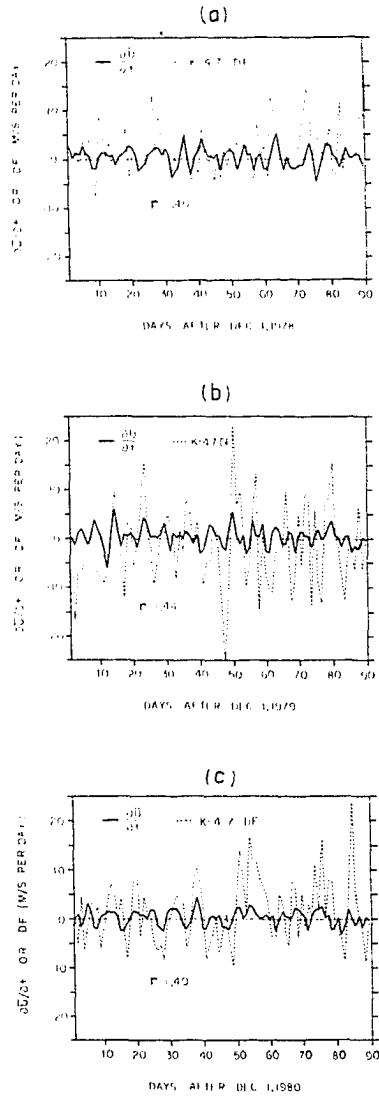
Figure 31. Observed time rate of change of zonal mean wind
($\partial \bar{u}/\partial t$) and medium-scale wave (k = 4-7) forcing at
50°S latitude and 300 mb for a) 1978-79, b) 1979-80,
c) 1980-81. Linear correlation coefficient (r)
is also shown in each figure. A value of r ≳ 0.3
is needed for significance at the 95% confidence
level

PRESSURE (MB)

(a) (b) (c)

LATITUDE SOUTH
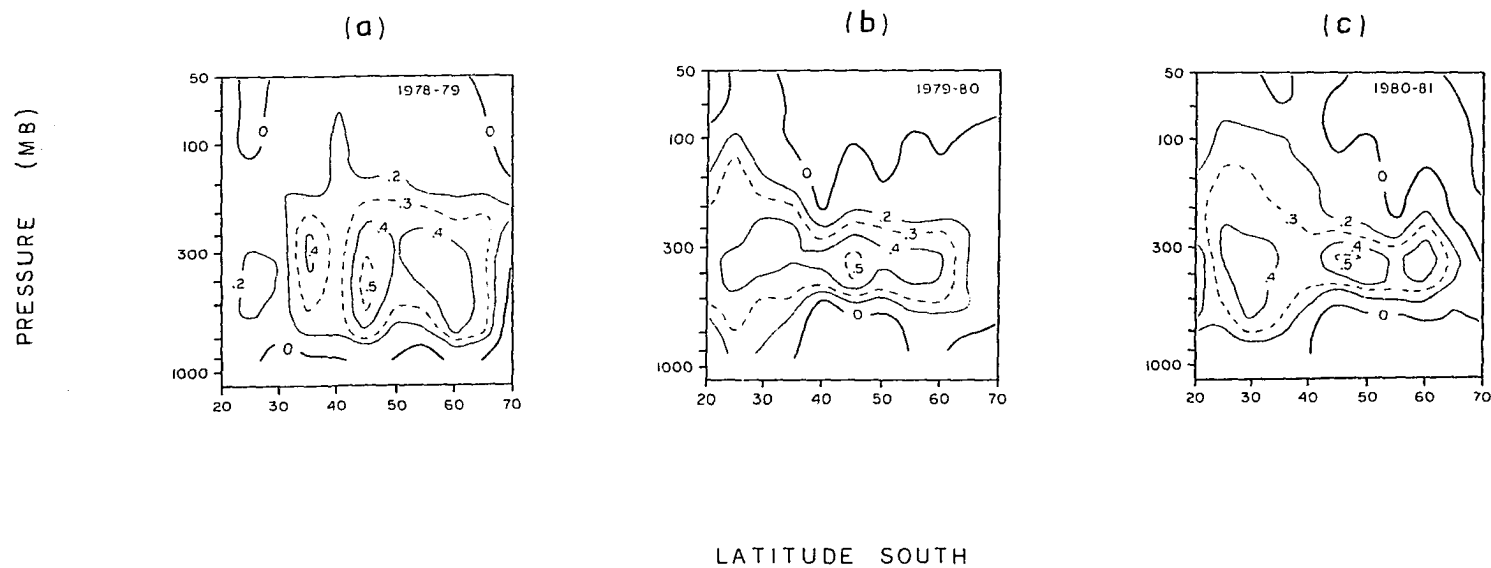
Figure 32. Meridional cross sections of the linear correlation
coefficient between observed zonal mean wind ac-
celeration and medium-scale wave forcing for
a) 1978-79, b) 1979-80, c) 1980-81. A value greater
than approximately 0.3 is needed for significance at
the 95% confidence level

85

3. Medium-scale wave forcing

The observed correlation between time changes in medium-scale wave energy and growth due to wave - mean-flow interaction allows the specific nature of the medium-scale wave forcing to be studied. The mean flow interaction can be split up into baroclinic and barotropic contributions (see Equation 14a), and compared with the wave energy (for reference). Linear correlation coefficients (at different time lags) between the wave energy and baroclinic or barotropic growth terms will quantify how these series are related in time. Such correlation coefficients are shown in Table 2 for different time lags (in days). A negative lag indicates that peaks in wave energy occur ahead (in time) of peaks in wave growth.

Table 2. Lag-correlations between medium-scale wave energy and baroclinic (BC) or barotropic (BT) wave forcing. A negative lag indicates that peaks in wave energy occur after (in time) peaks in wave growth

Lag in days	1978-79		1979-80		1980-81	
	BC	BT	BC	BT	BC	BT
-3	.21	.19	.20	.19	.35	.28
-2	.39	.21	.43	.15	.46	.30
-1	.60	.19	.60	-.01	.65	.17
0	.58	-.01	.48	-.35	.63	-.17
1	.16	-.26	.10	-.49	.34	-.29
2	-.09	-.33	-.18	-.42	.18	-.32
3	-.22	-.28	-.22	-.22	.08	-.33

The medium-scale wave energetics are displayed in this manner in Figures 33a-c. Large fluctuations in wave energy are observed each season, with a time scale between maxima on the order of ten days. Large fluctuations in baroclinic wave forcing are also observed, and peak values in baroclinic growth are clearly observed to be associated with peaks in wave energy. As shown in Table 2, the two series are well-correlated each summer, with largest values of the correlation coefficient seen for time lags between -2 and 0 days (largest at -1). That is, peaks in baroclinic growth occur approximately one day prior to peaks in wave energy. This correlation indicates the medium-scale waves result from baroclinic energy exchanges with the zonal mean flow.

Barotropic energy exchanges are usually negative, indicating the waves lose energy barotropically. Peak (negative) values of barotropic interaction are often observed subsequent to peaks in wave energy; the largest correlations are observed for time lags of 1-3 days. The correlation coefficient is significantly smaller than that between wave energy and baroclinic growth, although the association is clearly observed, particularly during 1980-81 (Figure 33c).

The observed correlations suggest that the energetics of the medium-scale waves may be described in terms of a type of _life cycle_. Baroclinic growth precedes a peak in wave energy by a time on the order of one day. The waves then reach a state of maturity for several days, followed by a maximum in barotropic decay 1-3 days following the energy maximum. This picture arises as a result of statistical estimates of the time varying wave- mean-flow energy exchanges, and individual cases may differ significantly.
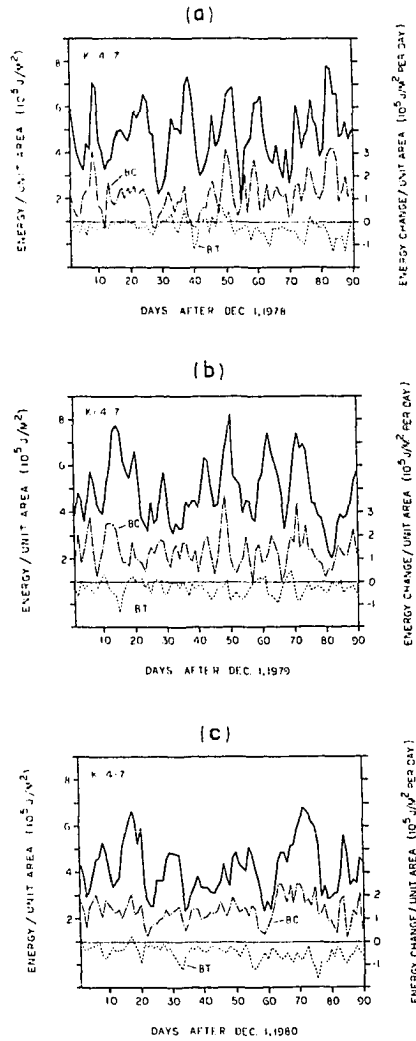
Figure 33. Time variations in medium-scale wave energy (heavy solid line), along with baroclinic (BC) and barotropic (BT) medium-scale wave-mean flow interaction terms, computed from Equation 14a, for a) 1978-79, b) 1979-80, c) 1980-81

A different cycle of energetic exchange is observed during days 25-50 of the 1978-79 season, and also during days 55-70 during 1979-80. During these periods, the medium-scale waves exhibit barotropic growth, in addition to exhibiting near-zero or negative baroclinic inter-actions. These distinct processes are not usually observed in the mid-troposphere, and will be shown in the next chapter to be the result of stationary-transient wave interference.

4. Medium-scale wave heat flux

The observed baroclinic wave growth is dependent upon the poleward heat flux induced by the waves. Time variations in heat flux are thus expected to be correlated with variations in wave energy. Because the calculated heat flux at a particular latitude and pressure tends to be noisy, estimates are made by averaging over several pressure levels and over 40-50°S latitude. Figures 34a-c show time series of the average heat flux in the lower troposphere (850-700 mb) and upper troposphere (200-300 mb), plotted with the medium-scale wave energy for reference. Lag correlations are presented in Table 3, showing the temporal re-lationship between medium-scale wave energy and heat flux. (A 1-1-1 filter in time has been applied to the series plotted in these figures, although correlations are calculated using the unfiltered series.) As expected, the heat flux is observed to be well-correlated with wave energy. Table 3 indicates that the largest heat flux in the lower troposphere occurs 0-1 days prior to wave energy maxima, similar to the baroclinic growth correlations. This is expected since the baroclinic growth depends on the wave-induced heat flux. The maximum heat flux in
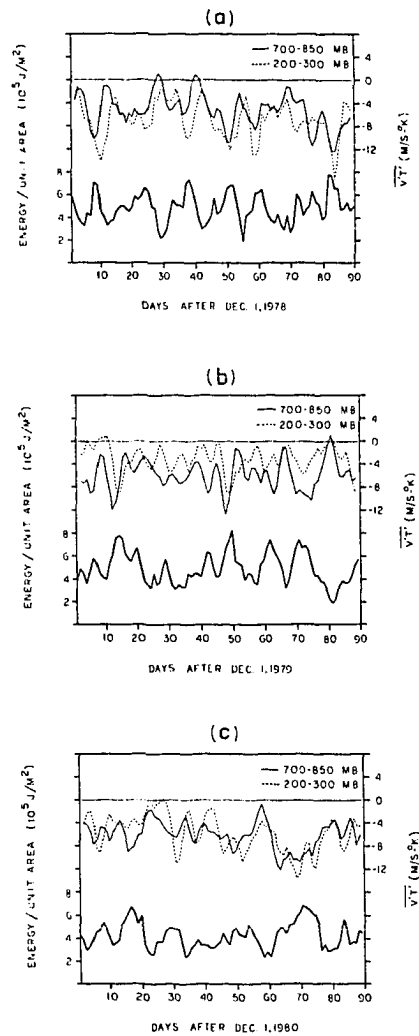
Figure 34. Time variations in medium-scale wave heat flux,
averaged over 40-50°S latitude and the indicated
pressure levels, along with the medium-scale wave
energy (heavy solid line) for reference. A 1-1-1
moving filter has been applied to the heat flux
curves for time smoothing. Negative values denote
transport towards the South Pole. a) 1978-79,
b) 1979-80, c) 1980-81

Table 3. Lag-correlations between medium-scale wave energy and upper
         (200-300 mb) or lower (700-850 mb) tropospheric heat flux.
         A negative lag indicates that peaks in wave energy occur
         after (in time) peaks in heat flux

Lag in days	1978-79		1979-80		1980-81	
	Upper	Lower	Upper	Lower	Upper	Lower
2	-.39	-.20	-.36	-.15	-.44	-.25
-1	-.65	-.34	-.54	-.39	-.62	-.43
0	-.62	-.55	-.39	-.47	-.54	-.50
1	-.17	-.35	-.07	-.34	-.26	-.36
2	.05	-.22	.16	-.13	-.09	-.21

the upper troposphere is best correlated for zero time lag, occurring

when the wave energy is largest. The heat flux in the upper tropo-

shere thus lags that in the lower troposphere by a time on the order

of one day. As will be shown for the case study, this time delay is

probably a result of the upward radiation of the wave as it matures.

Note the yearly variation in upper level magnitudes, as expected from

the time-average values shown in Figures 13a-c.

C. Zonal Mean Temperature Changes

It has been shown that changes in wave energy are associated with

opposite changes in zonal mean energy. The baroclinic growth of the

waves, and associated poleward heat flux, results in changes in the

zonal mean temperature field. These temperature changes, along with

the associated zonal mean thermal wind changes, result in the observed

zonal mean energy changes. It is of interest to consider the zonal

mean temperature changes explicitly. Figures 35a-c show the time varia-

tions in zonal mean temperature difference between 30 and 60°S latitude

at 850 mb, along with the medium-scale wave energy for reference.

Good anti-correlations are apparent in these figures; the medium-scale

wave growth results in a weakening of the zonal mean temperature gradient.

Likewise, when the wave energy decreases, the gradient is often ob-

served to increase, presumably a result of radiative forcing as dis-

cussed in the Introduction.

Figures 36a-c show similar diagrams for the upper troposphere

(200 mb), where the zonal mean temperature gradient is reversed (cold

equator and warm pole). The gradient is occasionally increased by

the presence of the waves (for example, December 12-15, 1979), although

the correlation is not generally as strong as that in the lower levels.

D. Energetics of Long (k = 1-3) and Short (k = 8-12) Waves

Wave-mean-flow energy exchanges may also be studied for waves of

other scales. Figures 37a-c show these exchanges for the long waves

(k = 1-3). The long waves generally exhibit smaller amplitude energy

fluctuations than the medium-scale waves, although there are occasions

of rapid growth. One example is near December 20, 1980, during which

time the zonal mean energy is found to lose a compensating amount of

energy (see Figure 26c). Close inspection reveals occasional anti-

correlations between the medium-scale and long wave energies. Some

examples of this are near days 10 and 85 of the 1978-79 season,
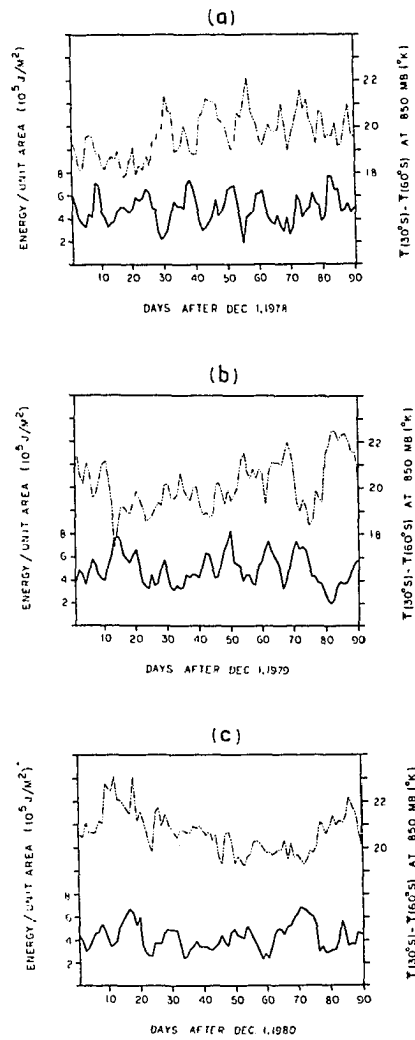
Figure 35. Time variations in the 850 mb zonal mean temperature difference between 30 and 60°S latitude (light dashed line), along with the medium-scale wave energy (heavy solid line) for reference. a) 1978-79, b) 1979-80, c) 1980-81
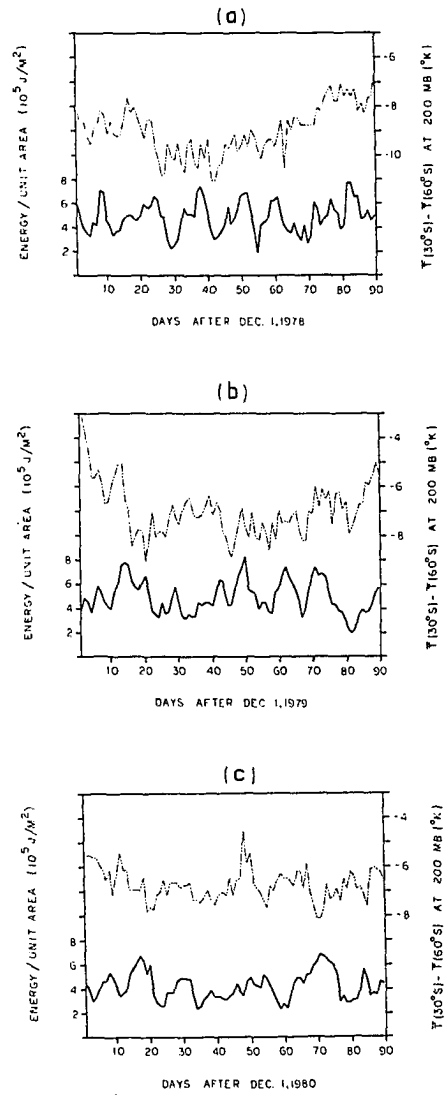
Figure 36. As in Figure 35, but for 200 mb
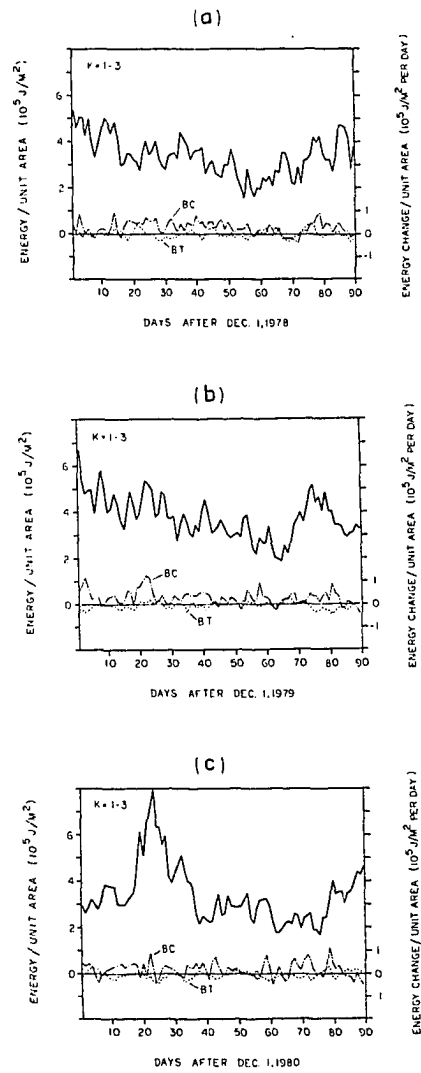
Figure 37. As in Figure 33, but for long waves (k = 1-3)

and days 20 and 85 for 1980-81. Examination of the zonal mean energy changes during these periods (Figures 26a and c) show generally poor anti-correlations with medium-scale wave energy changes. This result suggests the medium-scale waves may at times exchange energy with the longest scale waves instead of (or in addition to) exchange with the zonal mean flow. This is quite understandable if the medium-scale waves during these periods are not global in extent, but rather longitudinally localized. This conjecture if borne out in examination of the Hovmöller diagrams (Figures 18 and 20) during these times, which indeed show the medium-scale waves to be longitudinally localized features. Growth and decay may then occur at the expense of the zonal flow over a less than global scale, resulting in the observed changes in long wave energy.

Direct baroclinic and barotropic exchanges between the zonal mean flow and the long waves is generally small, even at times of large changes in long wave energy. This indicates a different mechanism may be responsible for maintaining these features.

Figures 38a-c show that the energy in the short waves (k = 8-12) is much more constant in time. Baroclinic growth and barotropic decay are again a generally observed characteristic, very similar to the medium-scale waves. Correlations are not strong, and are not shown, due to the noisy nature of these series.
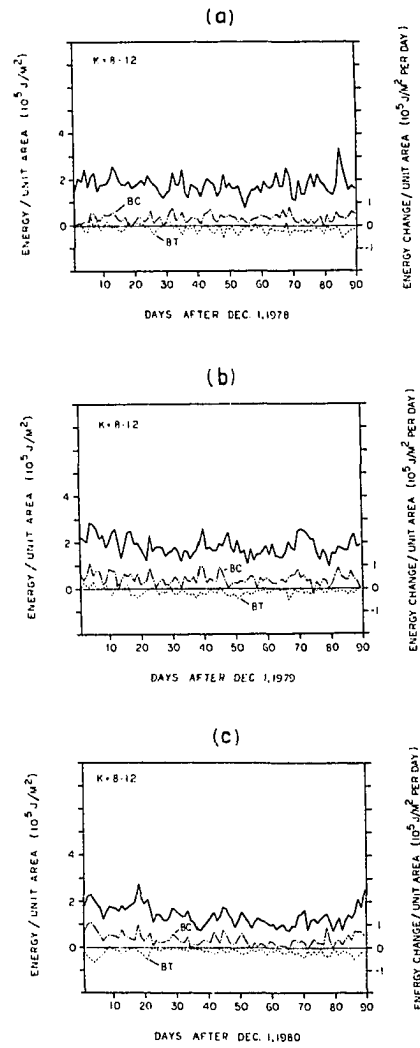
Figure 38.   As in Figure 33, but for short waves (k = 8-12)

E. Time-Mean Energy Changes

Table 4 shows the seasonally averaged integrated energy exchanges for the long, medium-scale, and short waves. Also shown (in parentheses) are the ratios of these exchanges to the magnitude of the respective average KE (from Table 1). This ratio is a measure of the relative 'energy exchange effectiveness.' Some important features seen in Table 4 are:

1) Medium-scale waves are much more effective at baroclinic growth than either the long or short waves.

2) Medium-scale and short waves exhibit similar effective barotropic decay rates.

3) The large medium-scale wave baroclinic growth rate during 1980-81 is accompanied by strong barotropic decay, and the total growth rate is similar to other years.

Figures 39a-c show meridional cross sections of the seasonally averaged baroclinic energy exchange for the medium-scale waves, along with the integrated total in the lower right hand corner (in agreement with Table 4). The largest contributions to these exchanges comes in the upper troposphere, centered near the jet core. This may be partly anticipated since the energy exchanges are proportional to the zonal mean wind (Equation 15), although the structure of the northward heat flux (which exhibits large variations in time) is the more important factor.

Similar structure is observed for the time averaged barotropic energy exchange seen in Figures 40a-c. Here, the largest (negative)

Table 4. Seasonal averages of wave - mean-flow energy exchanges, showing the baroclinic (BC) and barotropic (BT) contributions, and their total (TOT). Values (without parentheses) are in 10^4 J/m^2 per day. Values in parentheses are the ratio of that quantity to the respective wave KE (from Table 1), and represent a measurement of the 'normalized' growth rates

Season	k = 1-3			k = 4-7			k = 8-12		
	BC	BT	TOT	BC	BT	TOT	BC	BT	TOT
1978-79	2.4	-0.3	2.1	11.7	-2.8	8.9	3.0	-1.4	1.6
	(1.17)	(-.14)	(1.03)	(3.44)	(-.83)	(2.61)	(2.10)	(-.97)	(1.13)
1979-80	2.8	-0.7	2.1	13.1	-2.8	10.3	4.1	-1.3	2.8
	(1.20)	(-.29)	(0.91)	(3.71)	(-.80)	(2.91)	(2.74)	(-.84)	(1.91)
1980-81	1.6	-0.6	1.0	13.7	-4.4	9.3	3.5	-2.0	1.6
	(0.78)	(-.29)	(0.49)	(4.65)	(-1.50)	(3.15)	(3.13)	(-1.74)	(1.38)
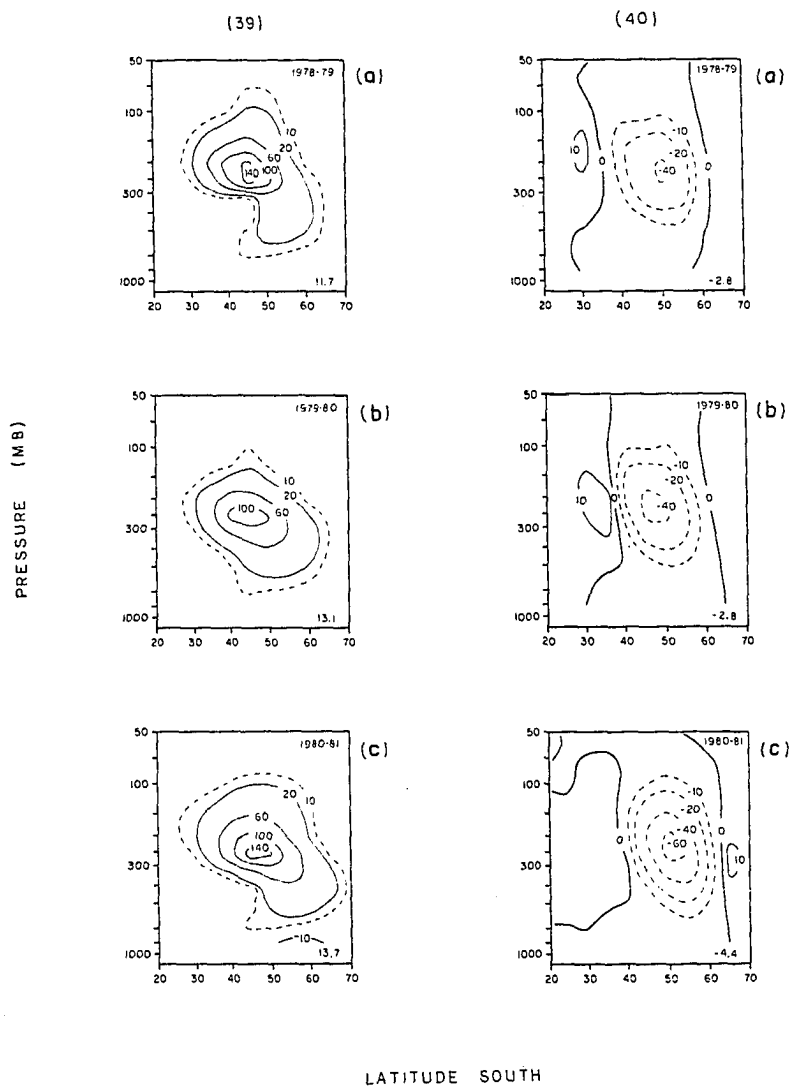
Figure 39. Meridional cross sections of seasonally averaged medium-scale wave baroclinic growth (10 J/m^2 day^{-1} mb^{-1}) for a) 1978-79, b) 1979-80, c) 1980-81. Numbers in lower right hand corner are integrated total, in 10^4 J/m^2 per day

Figure 40. As in Figure 39, but for barotropic growth

values are centered slightly poleward of the corresponding jet core.
In the time mean, barotropic interactions are thus acting to increase
the zonal-mean energy, whereas the baroclinic interactions act to
weaken it.

F. Time-Averaged EP Cross Sections

As discussed in the dynamics section, Eliassen-Palm (EP) flux
diagrams are a fundamental diagnostic for wave-zonal mean flow inter-
actions. They provide information on a) Rossby wave energy propagation,
b) the net effect of the waves on the mean flow, c) potential vorticity
flux, and d) source/sink regions of wave activity. As with the other
characteristics of the medium-scale waves, their EP diagrams exhibit
large changes in time (as will be shown in the case study). Here
time-averaged EP diagrams are considered, which show only the values of
the above diagnostics averaged over several lifetimes of the waves.
These time-averaged patterns are representative of the mechanisms
responsible for the medium-scale waves. The patterns found here are
a signature of the combined baroclinic-barotropic processes which the
medium-scale waves are observed to undergo.

Figures 41a-c show the three seasonal-average medium-scale wave
EP diagrams. A similar overall pattern is observed for each year,
which we discuss here before turning attention to individual seasons.
Rossby wave group velocity propagation is directed upwards, away from
the surface, in the lowest levels. Above 500 mb, the vectors turn
equatorward, with the vectors becoming nearly horizontal above 200 mb.

(a)   (b)   (c)

PRESSURE (MB)

LATITUDE SOUTH

102
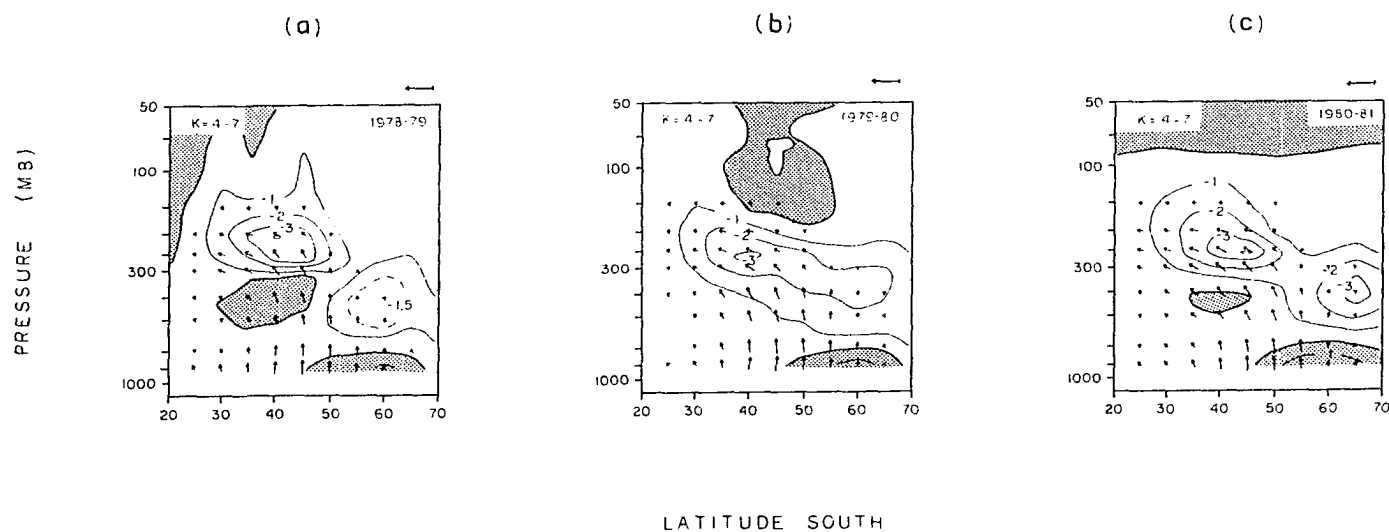
Figure 41.   Seasonally-averaged medium-scale wave Eliassen-
Palm diagrams for a) 1978-79, b) 1979-80, c)
1980-81. Plotting conventions are discussed in
Appendix C. Contour interval of 1 m/s per day

This result is in good agreement with the refractive index calculations

shown in Figures 15a-c. This is clearly illustrated in Figure 42,

where the vectors of Figure 41b are plotted with the refractive index

of Figure 15b. <u>Vertical or latitudinal wave propagation is observed</u>

<u>only in the regions of positive index</u>; in particular, no vertical

propagation is observed above 150 mb. In addition, the vectors are

observed to turn equatorwards, toward regions of larger refractive

index.

The negative contours of EP flux divergence in Figures 41a-c

indicate that in the time mean, the zonal flow is decelerated by the

waves, in the process exchanging zonal mean energy for wave energy.

The actual tendencies for changes in the jet will be different from

these contours, as the residual circulation (with cannot be calculated

geostrophically), $\overline{fv^*}$ in Equation 8, will redistribute the effect of

the forcing (McIntyre, 1982).

The contours also represent the net northward potential vorticity

flux $(\overline{v'q'})$ by the medium-scale waves (Equation 10). The predominantly

negative values indicate downgradient potential vorticity fluxes over

most of the region, because $\overline{q}_y$ is positive. This time-averaged down-

gradient flux agrees with the net time averaged generation of wave

enstrophy, as in Equation 11a.

Regions of positive EP flux divergence (shaded areas) indicate

positive northward potential vorticity flux $(\overline{v'q'} > 0)$. As described

previously, the upper levels (above 150 mb) are suspect and will not

be discussed further here. There is some year-to-year consistency in
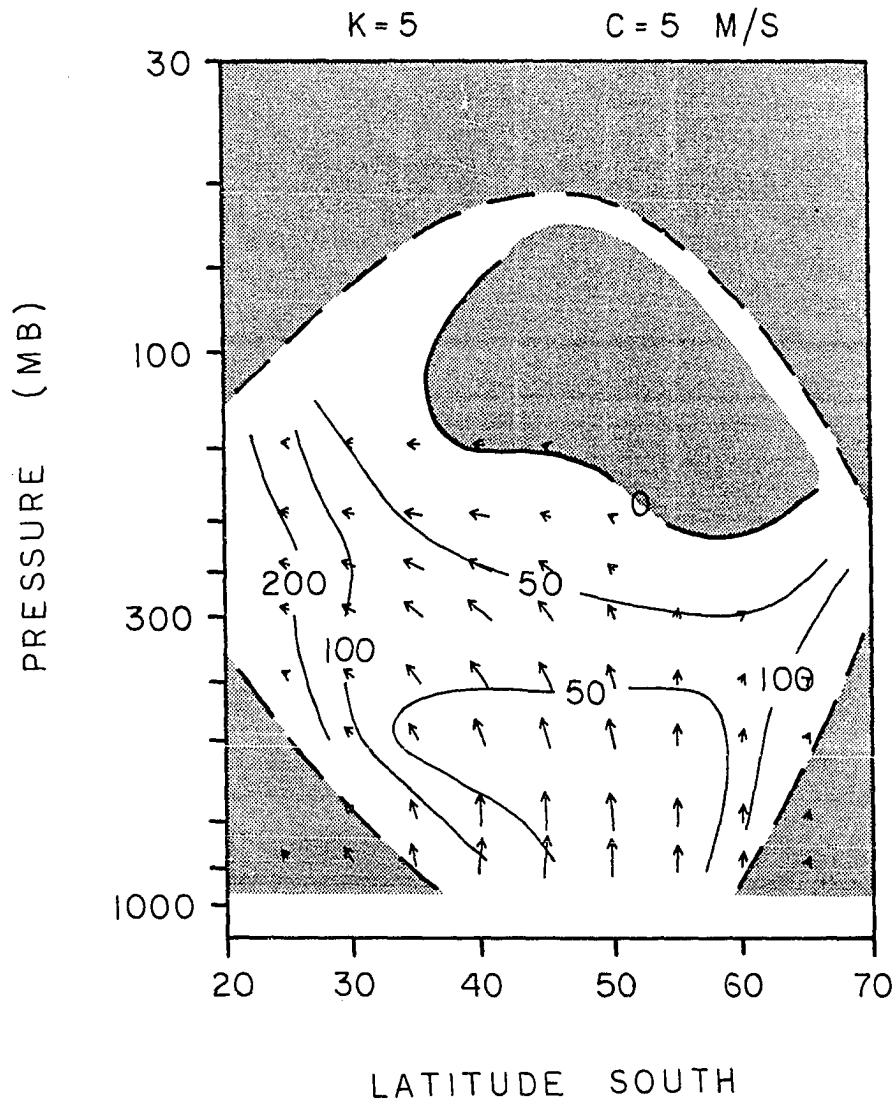
Figure 42. Refractive index contours (as in Figure 15b) along with EP flux or group velocity vectors (from Figure 41b). This shows the agreement between observed wave propagation characteristics and that expected due to the background wind structure

the positive areas in the lower and mid-troposphere, and these deserve some attention.

A prominent region of positive $\overline{v'q'}$ is seen in the lower troposphere, poleward of 50°S latitude. A similar feature was observed in EP diagrams for NH transient waves and modeled results, both reported by Edmon et al. (1980). They explained this as being the time average result of large fluctuations in $\overline{v'q'}$ and $\overline{q}_y$ in this region. As the baroclinic wave grows, the decrease in the meridional temperature gradient and increase in static stability cause the term $\rho_s^{-1} \frac{\partial}{\partial z} (\rho_s \frac{f}{N^2} \frac{\partial \overline{u}}{\partial z})$ in the expression (Equation 3b) for $\overline{q}_y$ to become strongly negative in this region. Large positive $\overline{v'q'}$ is observed when $\overline{q}_y$ is slightly negative, with the resulting flux still being downgradient. The time average $\overline{v'q'}$ shows positive values, while the time average $\overline{q}_y$ is only slightly negative here, poleward of 60°S latitude (see Figures 5a-c). Friction and diabatic effects may also influence the sign of $\overline{v'q'}$ when $\overline{q}_y$ is small.

A second area of positive $\overline{v'q'}$ is observed during 1978-79 and 1980-81 in the mid-troposphere (near 400 mb), centered near 35-45°S latitude. This feature is associated with the secondary heat flux maxima in the upper troposphere observed in Figures 12a and c. Cross sections of $\overline{q}_y$ show positive values throughout this area, and the nature of this feature is unknown.

Time-averaged EP cross sections for long waves (k = 1-3) are shown for each season in Figures 43a-c. As noted previously, the long waves are primarily quasi-stationary, climatologically-mean features, and the wave characteristics do not change drastically in time. The
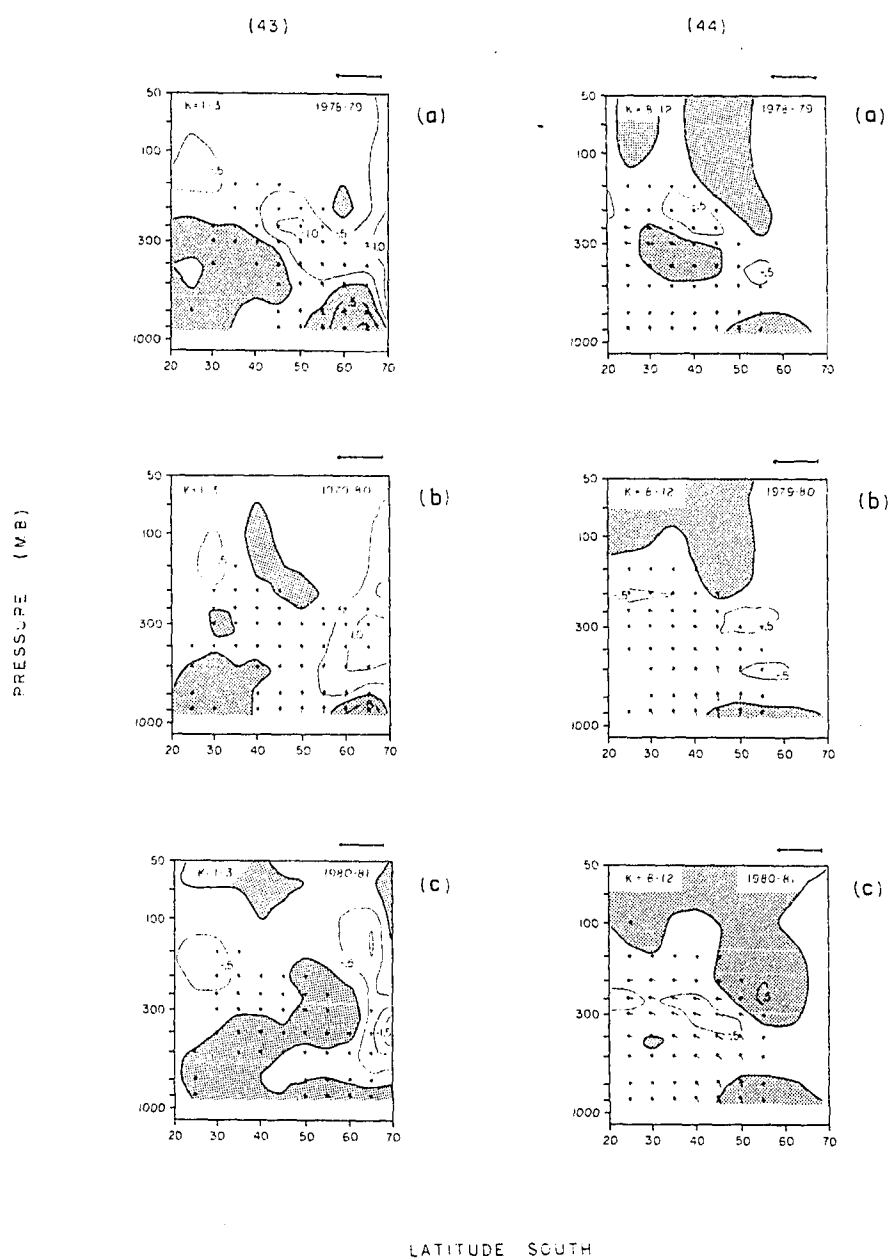
Figure 43. As in Figure 41, but for long waves (k = 1-3)

Figure 44. As in Figure 41, but for short waves (k = 1-3)

EP flux divergence contours in Figures 43a-c suggest that the climatological long waves decelerate the zonal-mean flow poleward of 60°S latitude each season.

The short wave (k = 8-12) EP flux diagrams in Figures 44a-c show very similar structure to the medium-scale wave diagrams for each season, with reduced amplitudes throughout. This similarity suggests the short wave contributions may reflect medium-scale wave structure which is not completely resolved in the k = 4-7 wave band. This situation is also partly suggested in the long wave EP diagrams, as the arrow patterns are again similar.

G. Modeled Baroclinic Waves

It is appropriate here to briefly review some results of modeled baroclinic waves. The simplest analytic models to capture the fundamental physics were developed by Eady (1949) and Charney (1947). Both of these models assumed latitude-independent motion linearized about a mean zonal wind which varied linearly in altitude. Normal mode analysis revealed that small amplitude waves would grow exponentially in time, drawing their energy from the (constant) basic state. Phillips (1954) found similar baroclinically growing solutions for a linearized two-layer model. The characteristics of these unstable waves included: a) zonal wavelengths near 4000 km, b) growth time scales of the order 2-3 days, c) eastward phase progression, and d) westward tilt with height, and associated northward heat transport. The agreement between the features of these simple models and the transient waves of mid-

latitudes prompted the identification of the observed waves as finite amplitude baroclinic instabilities. They are sometimes referred to as Charney modes.

Aside from these much-simplified models, analytic solution of the potential vorticity equation, subject to the appropriate boundary conditions, becomes intractable. These equations may be solved numerically, however, using computer models incorporating realistic basic states. Extensive efforts have been undertaken to simulate the observed characteristics of atmospheric baroclinic waves (although the characteristics of the baroclinic waves may be difficult to isolate). A moderate degree of success has been realized, although the results of such models based upon linear theory differ significantly from the observed wave characteristics. In particular, linear models predict short zonal wavelengths ($k > 10$) to be the most unstable, and the largest disturbance amplitude to be found near the surface (Gall, 1976). More realistic results were obtained with the use of a nonlinear model developed by Simmons and Hoskins (1978) (hereafter HS). Some aspects of their modeled baroclinic waves are presented here.

HS studied the finite amplitude evolution of baroclinic waves using a spherical, primitive equation spectral model. The initial state consisted of a midlatitude jet centered in the upper troposphere in midlatitudes (very similar to the observed SH summer jet) upon which is superimposed a small amplitude, zonally symmetric wave 6 perturbation of normal mode (linear or Charney type) form. Forward integration in time shows this unstable wave to exhibit a well-defined life cycle, as shown in Figure 45, adapted from HS. Baroclinic growth precedes a peak
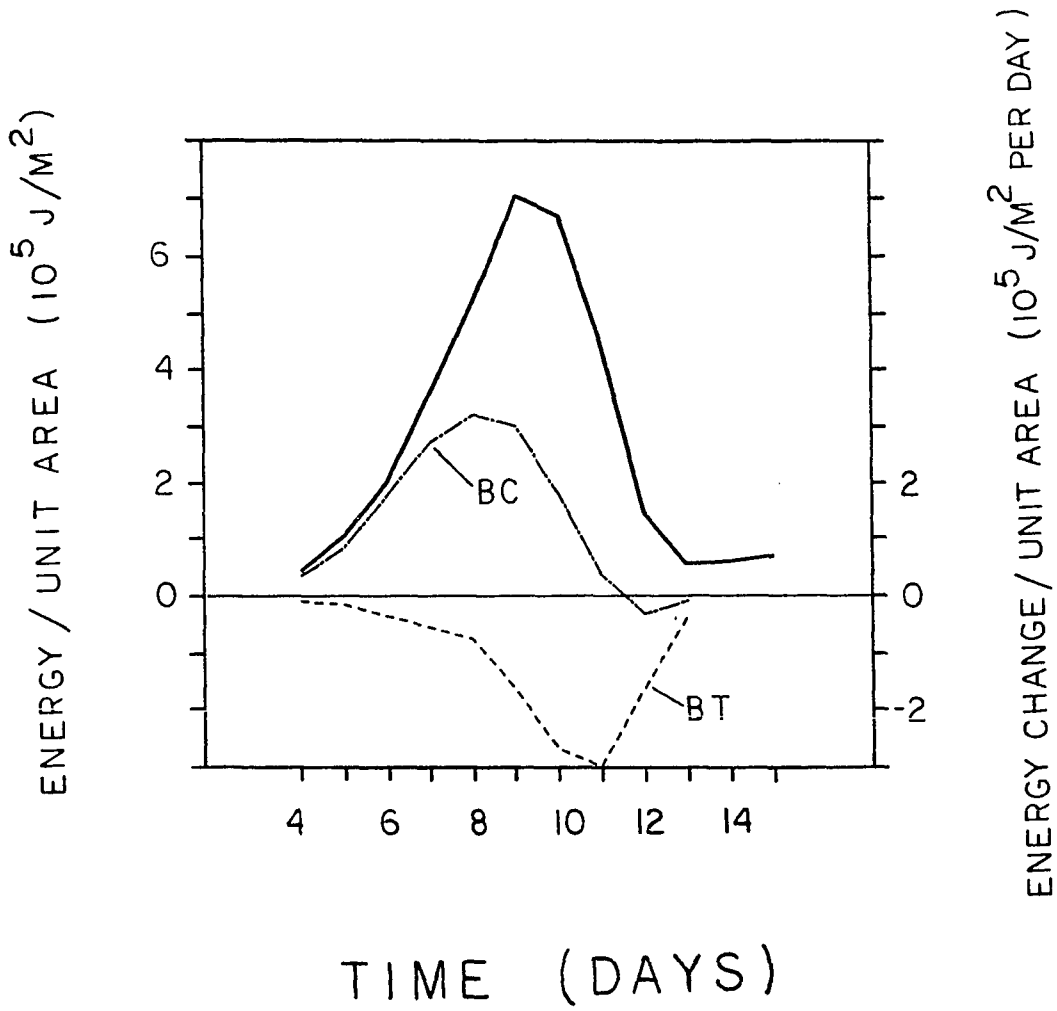
Figure 45. Life-cycle energetics of modeled baroclinic wave, after Simmons and Hoskins (1978). Shown are the wave energy (heavy solid line), along with the baroclinic (BC) and barotropic (BT) growth terms

in wave energy by approximately one day, and the wave energy then decays due to barotropic interactions. HS explain the barotropic decay to result from longitudinal variations in the phase speed of the wave, which they show are determined by local variations in $\bar{u}$ and $\bar{q}_y$. This life cycle is similar to that observed in this study for the medium-scale waves, particularly in the time lags between growth, maturity, and decay.

Net changes in the zonal mean temperature gradient in the HS model are confined to the lower troposphere, resulting in an increase in static stability in the lowest levels. These changes in static stability, along with frictional effects, limit the growth of shorter scale waves ($k > 8$), which are primarily surface waves. As a result, the longer waves ($k = 5$-7), which extend over a greater depth of the atmosphere, continue to grow in the upper levels and reach much larger amplitudes. Nonlinear effects are crucial in the development of finite amplitude baroclinic waves. Similar results were noted by Gall (1976) in a different nonlinear model.

Figure 46 shows the life-cycle averaged EP diagram for this model, adapted from Edmon et al. (1980). Although the vertical scale is linear in pressure and the plotting conventions (as described in Edmon et al., 1980) are different from those employed here, the essential characteristics are unchanged. Wave propagation is upwards in the lowest levels, turning equatorward above 300 mb. Large convergence is centered near 35-40° latitude (approximately 10 degrees poleward of the average jet) and 200-150 mb (slightly above jet core). Positive EP divergence is found in the lowest levels, centered near 50-60° latitude,
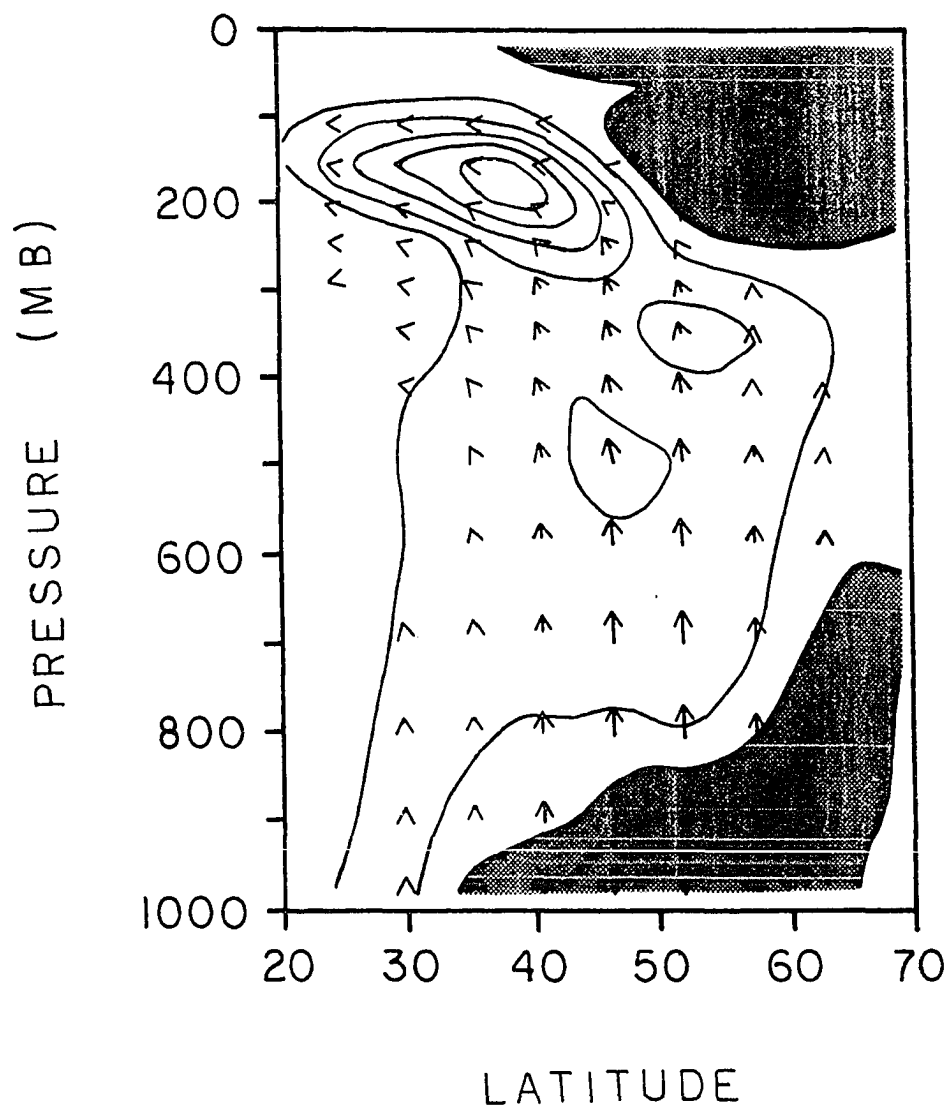
Figure 46. Life-cycle averaged EP flux diagram for modeled
baroclinic wave, after Edmon et al. (1980). Al-
though the vertical coordinate is linear in pressure,
and the plotting conventions (discussed in Edmon
et al.) are different than those employed for other
EP flux diagrams here, the essential features remain
unchanged. Shaded regions denote positive EP flux
divergence

this being a result of the time averaging as noted earlier.

The observed medium-scale wave EP diagrams (Figures 41a-c) show a high degree of agreement with these modeled results. In particular, the maximum EP convergence in the upper troposphere is 5-10 degrees equatorward of the corresponding time-averaged jet (Figures 4a-c). The observed cross sections show a secondary convergence region on the poleward jet flank region, whereas there is only a hint of a similar feature in the modeled results. Low level regions of positive EP divergence are observed in both cases.

The excellent agreement between the observed and modeled results, in particular the energy cycle and life-cycle averaged EP cross sections, lend confidence to both the model results and the identification of the medium-scale waves as finite amplitude baroclinic instabilities.

H. Enstrophy Calculations

The energy calculations presented here confirm the conservation of energy as a fundamental principle in medium-scale wave dynamics. A second fundamental conserved quantity for large-scale atmospheric motions is one-half the square of the potential vorticity, called the potential enstrophy. The conservation of wave potential enstrophy is found in Equation 11a, which is derived directly from the potential vorticity equation. It is important to note that this derivation is independent of any energetic considerations.

The fundamental quantity DF (or $\overline{v'q'}$) appears as a forcing in the wave potential enstrophy equation (Equation 11a), similar to the wave

energy equation:

$$\frac{\partial}{\partial t} \left(\frac{1}{2} \overline{q'^2}\right) = \overline{v'q'} \cdot \overline{q}_y$$

In fact, the similarity of the energy and potential enstrophy equations initially prompted the analyses presented in this section. The results presented here will corroborate the conclusions derived from the energetic analyses.

As shown by Palmer (1982), the quantity $\frac{1}{2} \overline{q'^2}$ based on geostrophically evaluated winds is not exactly conserved for planetary scale motions. This is due to the fact that for very large scale (in latitude) motions, the geostrophic wind is divergent (on the sphere). He suggests a slight modification to correct this; his result is given in Appendix D and is used in these calculations. Cross sections of medium-scale wave potential enstrophy were discussed in Section IV.C and shown in Figures 10a-c. Integrated values are given by the same procedure as used in the energetic analyses.

Figure 47 shows the time-variations in the integrated medium-scale wave potential enstrophy for 1979-80, along with the medium-scale wave energy for comparison. <u>Variations in wave potential enstrophy are almost identical to variations in wave energy</u> (depending on the plotting scales used), and little new information is obtained. Similar results are found for other years. Since the wave potential enstrophy is proportional to $K^4 \psi^2$ (where K is the total wavenumber and ψ the wave amplitude) and the wave energy proportional to $K^2 \psi^2$, the identical behavior seen in Figure 45 indicates the wave amplitude is the important varying quantity (as opposed to the total wavenumber K).
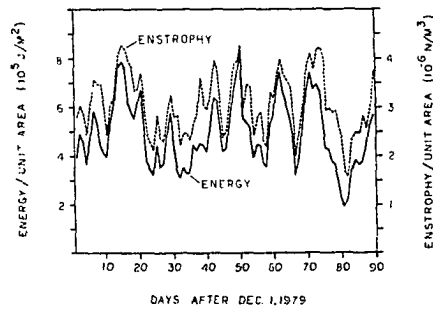
Figure 47. Time variations in the integrated medium-scale wave
potential enstrophy and energy during 1979-80
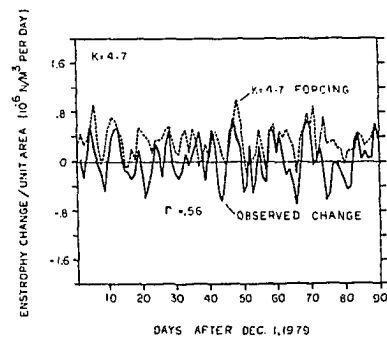
Figure 48. Observed rate of change of medium-scale wave poten-
tial enstrophy, along with medium-scale wave forcing,
for 1979-80. The linear correlation coefficient
(r) is also shown. A value of r ≳ 0.4 is needed
for significance at the 95% confidence level

Equation 11a is now employed to determine if observed enstrophy

changes are in agreement with changes resulting from the wave-induced

flux of potential vorticity. These calculations are identical to the

wave energy calculations (Equation 15), with $\bar{u}$ replaced by $\bar{q}_y$. Figure

48 shows the medium-scale wave induced changes, along with the actual

measured changes. The good agreement is apparent, and this figure is

overall very similar to that for the wave energy (bottom Figure 29).

Again, the time-mean generation is greater than zero, this presumably

being balanced by some mean enstrophy dissipation.

The agreement between observed and calculated changes allows the

specific nature of the enstrophy forcing to be studied. The baroclinic

and barotropic forcing terms are plotted in Figure 49, along with the

wave enstrophy for reference. Peaks in wave enstrophy are preceded

by baroclinic growth and followed by barotropic decay, similar to the

energy calculations. These associations are quantified by the lag-

correlations shown in Table 5. Comparison with the corresponding energy

calculations (Figure 33b and Table 2) shows near identical behavior:

little new information is obtained from the enstrophy calculations.

Similar behavior is found each year. This agreement, along with the

symmetry of Equations 11a and 15, confirm the fundamental nature of DF

in the medium-scale wave dynamics. This was anticipated, as changes

in $\bar{u}$ and $\bar{q}_y$ are generally small, whereas DF exhibits large fluctuations

and often changes sign.

The time-average baroclinic enstrophy generation cross section is

shown in Figure 50a. The largest generation is in the upper troposphere

(near 250 mb), concentric with the baroclinic energy generation seen in
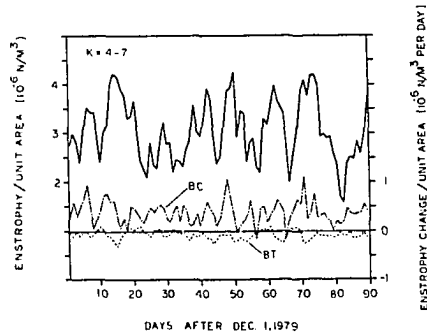
Figure 49.   Time variation in medium-scale wave potential
             enstrophy (heavy solid line), along with baroclinic
             (BC) and barotropic (BT) growth terms, during
             1979-80
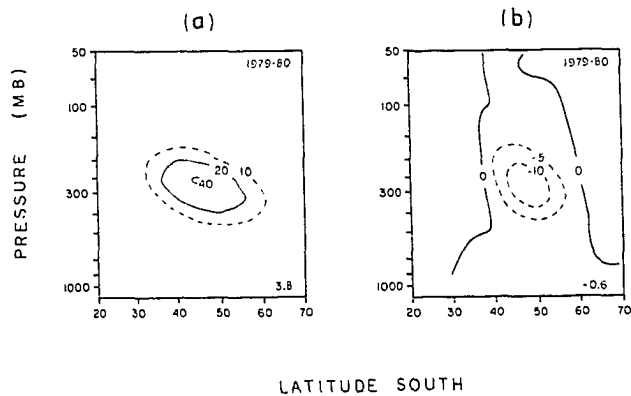
Figure 50.   Seasonally-averaged medium-scale wave potential
             enstrophy generation due to a) baroclinic and b)
             barotropic wave-mean flow interactions (10^{-10}
             N/m^3 day^{-1} mb^{-1}). Numbers in lower right hand
             corner are integrated total in 10^{-6} N/m^3 per day

Table 5. Lag-correlations between medium-scale wave potential enstrophy and forcing due to baroclinic (BC) or barotropic (BT) wave— mean-flow interactions, for the 1979-80 season. A negative lag indicates that peaks in wave potential enstrophy occur after (in time) peaks in growth terms

Lag in days	BC	BT
-3	.24	.09
-2	.35	-.02
-1	.47	-.16
0	.31	-.37
1	-.09	-.45
2	-.28	-.31
3	-.22	-.11

Figure 39b. The pattern is similar to that of $\bar{q}_y$, although slightly higher in the atmosphere. The time-mean barotropic exchange cross section in Figure 50b is centered lower than that of the barotropic energy exchange (Figure 40b), although similar overall. Each year shows similar characteristics.

Potential enstrophy calculations presented here reinforce the conclusions derived from the energetic analyses, but provide little new information. Because the enstrophy budget is derived independently of energetic considerations, this puts further confidence in the energetic results, and again illustrates the fundamental importance of the Eliassen-Palm flux divergence.

I. Case Study

The energetic calculations illustrate the episodic or life-cycle nature of the medium-scale waves. The characteristics of the waves are constantly changing in time, and thus far, only time-averaged values of various diagnostics, such as time-mean EP diagrams, have been examined. To better understand the changes exhibited during a typical life-cycle, this chapter will conclude by closely examining a particular case of the medium-scale wave growth and decay.

The case chosen occurs during mid-December 1979, and is chosen because it is apparently a 'clean' example. This is the same example we have referred to throughout this work, i.e., that of Figures 7a-c. It is primarily a wave-6 feature, facilitating direct comparison with the modeled results of HS, which are for a zonally-symmetric wave-6 baroclinic instability. Both the integrated energetics and daily cross sections will be presented.

1. Integrated energetics

The integrated energetics are shown in Figure 51 for both wave 6 along and waves 5-7 combined. Most of the energy and most of the baroclinic growth are in wave 6 alone. This spectral purity indicates that the wave grows baroclinically in a zonally symmetric fashion, perhaps indicative of a preferred zonal model for instability. The barotropic decay, on the other hand, is spread over several wavenumbers, and is thus more localized longitudinally. Keeping these facts in mind, we refer to waves 5-7 for the rest of this discussion. December 13, 1979, the date of the peak in wave energy, is chosen as 'day 9,'
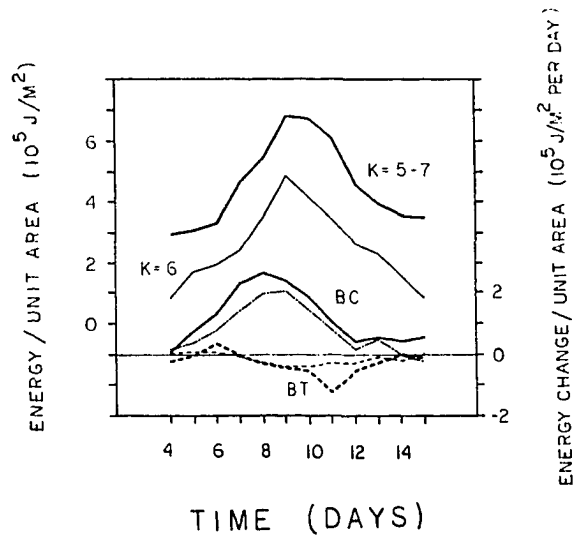
Figure 51. Time variations in integrated energetics during
case study. Shown are the wave energy (solid lines),
along with the baroclinic (BC) and barotropic (BT)
growth terms, for both wave 6 alone (light lines)
and waves 5-7 combined (heavy lines). 'Day 9' is
December 13, 1979
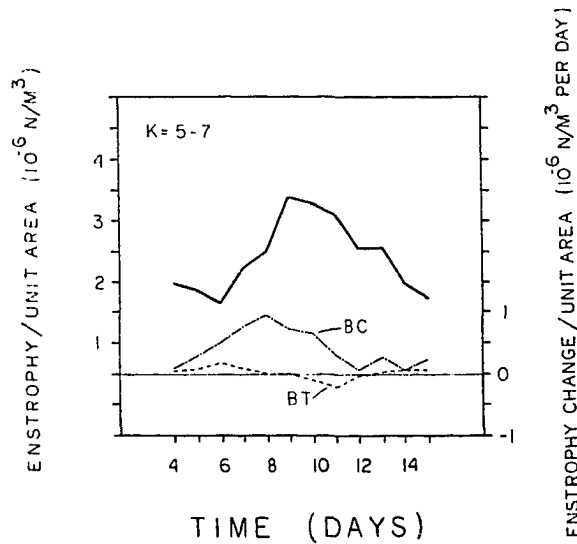
Figure 52. Time variations in integrated potential enstrophy
(heavy solid line), along with baroclinic (BC) and
barotropic (BT) generation terms, for the case study

this being for comparison with the HS model results.

The life-cycle (days 5-14) averages of wave energy, along with baroclinic growth and barotropic decay rates, are very similar to the seasonal medium-scale wave averages found in Tables 1 and 4. The peak in baroclinic growth precedes the energy peak by one day, whereas the largest barotropic decay occurs approximately two days following the energy maximum. These results are in agreement with the lag-correlation results calculated for each season, and also the modeled results of HS (see Figure 45). The maximum barotropic decay rate (on day 11) is roughly one-half as large as the maximum baroclinic growth rate (on day 8). In comparison, the HS model results show similar growth and decay rates.

The integrated wave potential enstrophy and wave-mean-flow interaction terms are shown in Figure 52, displaying much the same characteristics as the energy budget.

The zonal mean energy exhibits compensating energy changes during this period, as shown in Figure 53. This zonal mean energy change is due to a reduction in the lower tropospheric temperature gradient, resulting from the poleward heat flux of the waves. The zonal mean temperature difference between 30 and 60°S latitude in the upper (200 mb) and lower (850 mb) troposphere is plotted in Figure 54, clearly showing the wave-induced changes. The 850 mb gradient is weakened as the wave grows, echoing the zonal mean energy change. The (reversed) gradient at 200 mb is initially weakened, whereas after a lag of approximately 3 days, it is increased strongly (becoming more negative) as the wave reaches maturity. As will be seen by studying the daily wave structure, this
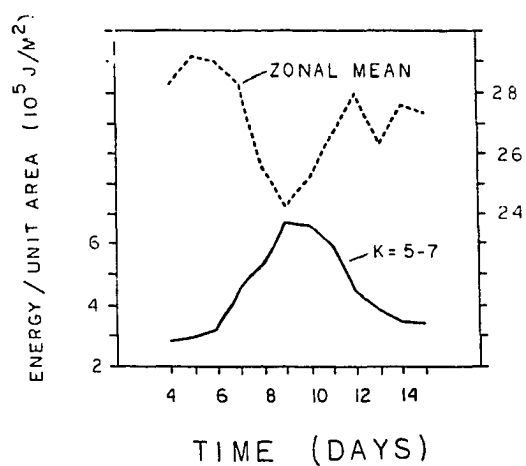
Figure 53. Time variations in integrated zonal mean and wave energy during case study
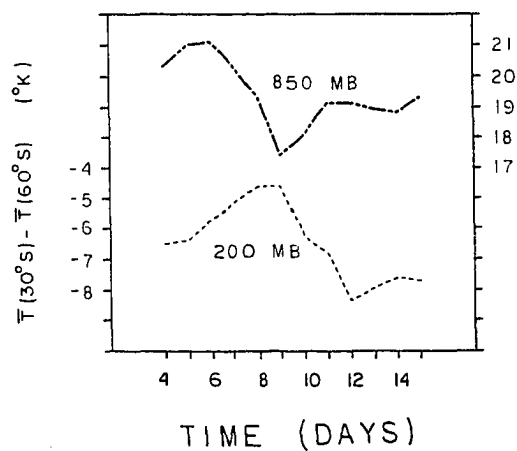
Figure 54. Zonal mean temperature difference between 30 and 60°S latitude, for 850 mb (top) and 200 mb (bottom), during case study. Note the 200 mb differences increases between days 9 and 12

time lag can be understood in terms of the upward propagation of the wave.

2. Daily cross sections

The daily structure and evolution of both the baroclinic wave and the zonal mean flow are now examined. This discussion is based on the daily EP flux cross sections (for waves 5-7) shown in Figure 55, along with daily cross sections of $\bar{u}$ and $\bar{q}_y$ shown in Figure 56. Because the daily EP diagrams tend to be rather noisy, a 1-2-1 smoothing filter in latitude is applied to the geopotential Fourier coefficients before further calculations. In addition, some zero contour lines have been omitted for clarity.

The initial jet is rather broad, centered near 35-40°S latitude (Figure 56). The structure of the instability during the first several days shows maximum heat flux in the lowest levels near 40-45°S latitude, with predominantly vertical propagation and convergence throughout much of the mid-to-upper troposphere (250-500 mb). As the wave grows, the jet core maintains its position and intensity, while the vertical shear in the lower levels over 45-50°S latitude decreases. This results in a much narrower jet by day 9, along with a stronger $\bar{q}_y$ area below the core region. The instability achieves its largest baroclinic growth rate on day 8, with largest (negative) DF in the upper troposphere (250-300 mb) near 35-45°S latitude. Note this is the region of largest $\bar{u}$ and $\bar{q}_y$; the wave thereby maximizes both energy and enstrophy generation. The wave is also starting to propagate equatorward on day 8.

The instability reaches maturity near day 9, with heat flux now
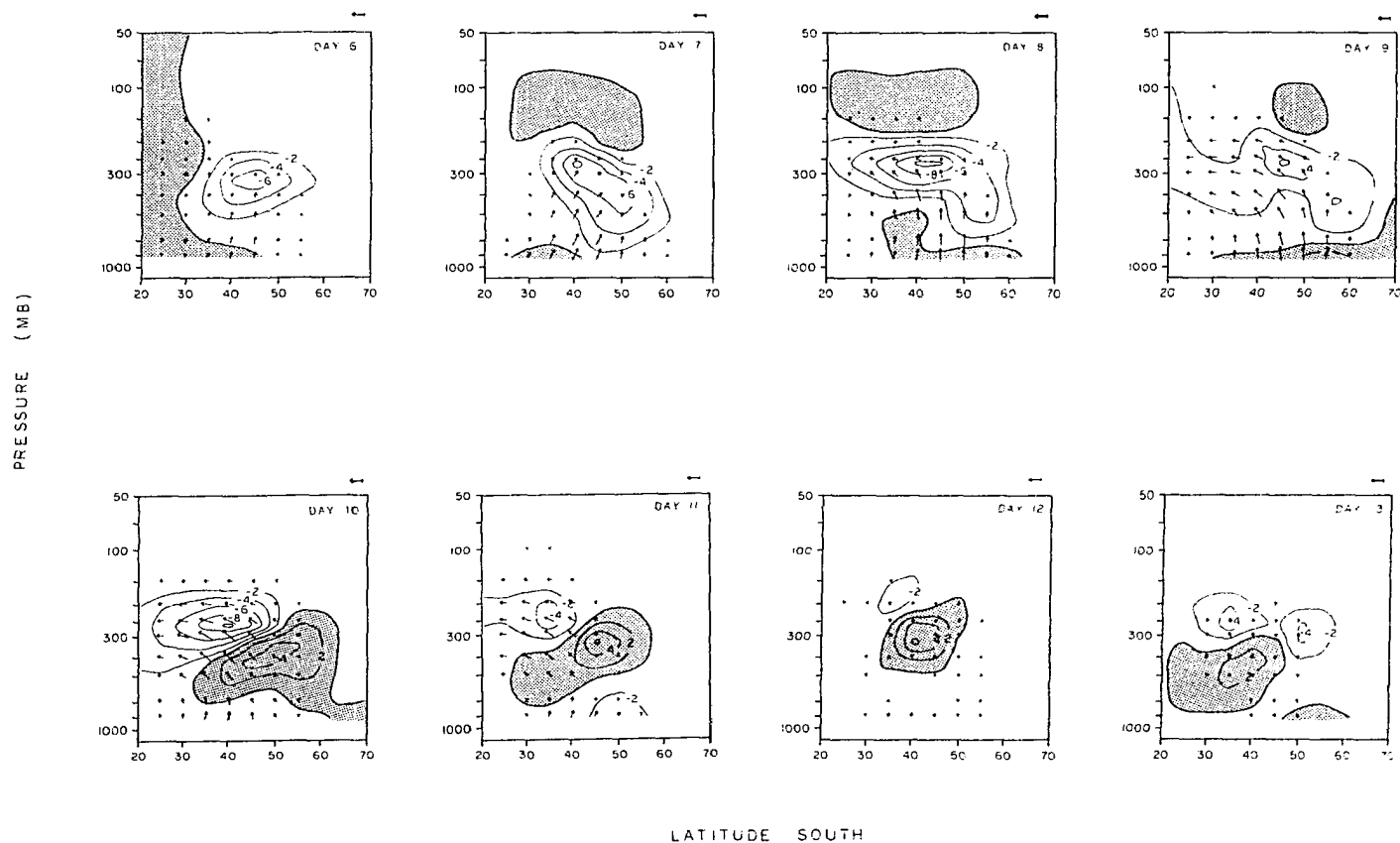
Figure 55. Daily EP flux diagrams for days 6-13 during case
study. Individual days are labeled in the upper
right hand corner. Plotting conventions are given
in Appendix C. Contour interval is 2 m/s per day

123

PRESSURE (MB)

LATITUDE SOUTH
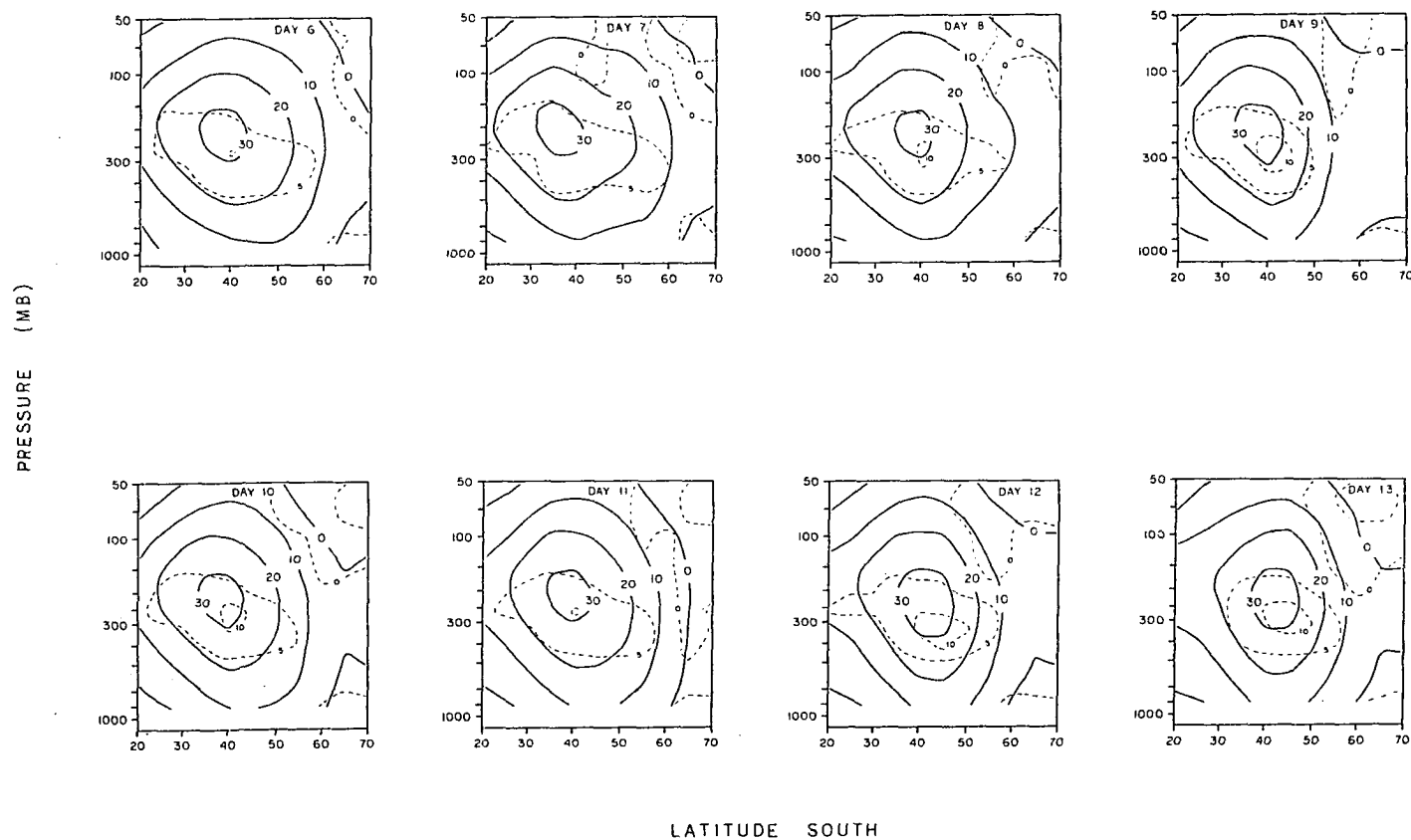
Figure 56. Daily cross sections of zonal mean wind (solid
lines-contour interval of 10 m/s) and zonal mean
potential vorticity gradient (dashed lines-contour
interval of $5 \cdot 10^{-11}$ (m-s)$^{-1}$ for days 6-13 during
case study. Individual days are labeled in the
upper right hand corner

extending throughout the entire troposphere. This extension results in less convergence in the upper troposphere, associated with a slower barotropic growth rate. During the following days, the heat flux lessens in the lower levels, maintaining a maximum in the mid-to-upper troposphere. The upper level poleward heat flux results in an increase in the 200 mb zonal mean temperature gradient after day 9, as shown in Figure 54.

After day 8, the upper level arrows turn increasingly equatorward. This equatorward propagation is associated with poleward momentum flux and the start of barotropic decay. The wave momentum flux convergence results in a broadening of the jet structure between days 9-11. A large source of wave activity is found in the mid-troposphere starting on day 10, associated with the Rossby wave radiation toward the tropics. This leads to positive or upgradient potential vorticity flux in mid-latitudes, centered near 45°S latitude. The barotropic decay and EP flux divergence reach a maximum on day 11. As the main divergent region on this day (near 45°S latitude) is rather narrow, the latitudinal filter has smoothed the peak value (which is near 12 m/s per day with no smoothing). A small amount of poleward propagation is observed during the late stages (days 11-13). The final jet structure is centered near 40-45°S latitude, approximately 5 degrees poleward of the initial state. Comparison with the initial structure shows the final jet to have a much more barotropic structure.

The ten-day average EP cross section is shown in Figure 57. This figure is very similar to the seasonal averages shown in Figures 41a-c. This is expected because the seasonal mean is the average over many similar life cycles of medium-scale waves. Note the canceling effects
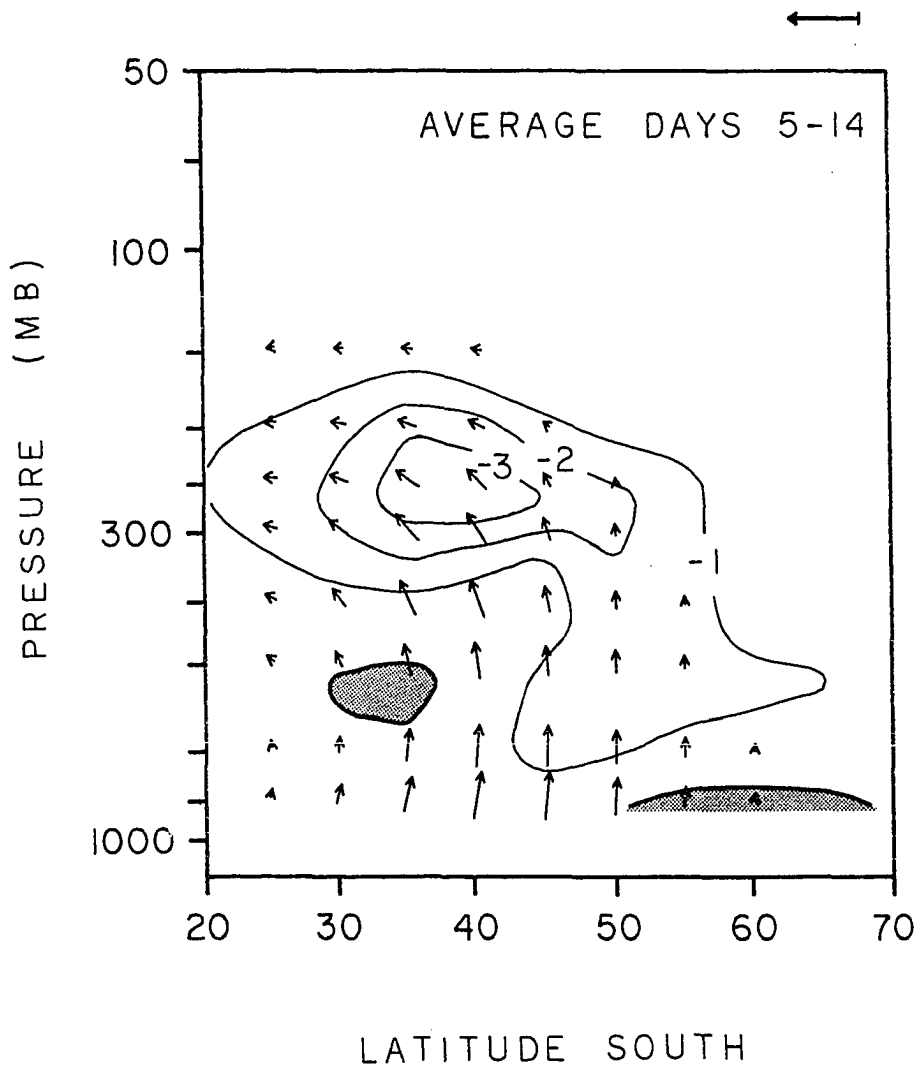
Figure 57. Life-cycle (days 5-14) averaged EP diagram for case
study. Plotting conventions given in Appendix C.
Contour interval of 1 m/s per day

of the negative and positive EP flux divergence in the mid-troposphere between growth and decay stages. It is the residual of this cancellation that appears in the time-averaged picture.

Comparison of these observed cross sections with those of HS are very favorable. Their EP cross sections for day 5 (from Edmon et al., 1980) show similar behavior with the early stages here, although their day 8 shows the large divergent region throughout much of the troposphere not observed here until day 10. As shown before (Figure 46), their life-cycle averaged result is very realistic. Their zonal mean jet moves approximately 5 degrees poleward over the life cycle, in agreement with the results here.

Figure 58 shows the evolution of the vertical phase structure of wave 6 at 40°S latitude throughout this episode. The largest phase tilt is below 500 mb for the first several days (in agreement with the low level heat flux), while the tilt is evident throughout the troposphere by day 8. Note the decay stage produces an eastward tilt with height (downward propagation) on day 12. The phase progression is slower during the growth phase (average of 7 m/s over days 6-8) as compared to that over the decay stage (average 13 m/s over days 10-12). Pfeffer et al. (1974) have noted similar characteristics for baroclinic waves in laboratory annulus experiments. This effect may be due in part to the Doppler shifting of the wave phase speed in the (wave-induced) changing background wind.

128
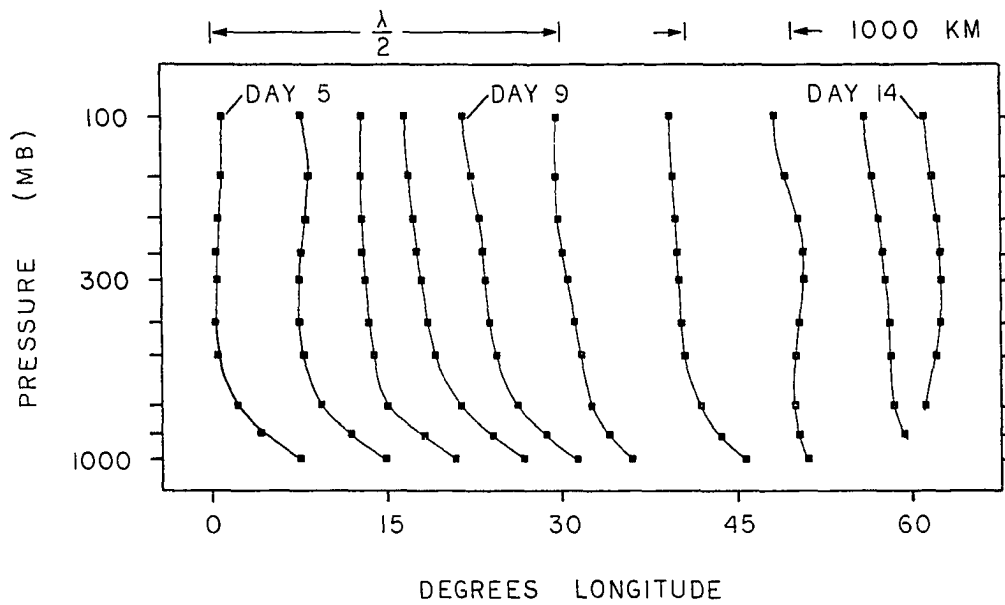
Figure 58. Daily vertical phase structure for wave 6 at 40°S
latitude throughout the case study. Longitudinal
scale at bottom, while one-half wavelength and 1000
km scales are shown at the top for reference

3. Summary: Life-cycle of a baroclinic wave

In summary, this case study has produced the following picture of the medium-scale wave life-cycle. A strong initial zonal mean temperature gradient is associated with a baroclinically growing wave. The wave's poleward heat flux, found initially in the lowest levels, radiates upward, reaching large values in the upper levels several days later. Reduction of the strong meridional temperature gradient in the lower troposphere is associated with smaller heat fluxes there, and baroclinic growth begins to slow. The wave reaches its largest amplitude approximately one day after its maximum baroclinic growth rate. At maturity, the heat flux is predominantly in the upper levels, and the wave begins propagating strongly equatorward. This equatorward propagation is presumably due to the latitudinal phase shift induced in the wave by latitudinal shears of the background zonal flow, as discussed by Simmons and Hoskins (1978). The barotropic decay reaches a maximum approximately two days following the wave amplitude maximum, resulting in a strengthening of the zonal mean jet. The final jet is much more barotropic than that found initially.

VI. STATIONARY-TRANSIENT MEDIUM-SCALE WAVE INTERFERENCE

The first part of this section will describe exactly how it is
determined that stationary-transient medium-scale wave interference is
indeed observed. The characteristics and possible origin of the sta-
tionary or time-mean waves will then be discussed. A simple analytical
model of interfering waves will be introduced, and finally, some of the
observed interference characteristics will be analyzed in terms of this
model.

A. Identification

1. <u>1978-79</u>

The first clue that stationary-transient wave interference is
occurring is the semi-regular appearance of medium-scale wave amplitude
maxima during 1978-79. Figure 59 (bottom) shows the wave energy (same
data as Figure 33a), along with the phase of transient wave 5 (top).
Wave amplitude maxima are observed each time the transient wave phase
is in a particular position — within the shaded region. This correla-
tion between wave amplitude and phase suggests a) stationary-transient
wave interference, and/or b) preferred region(s) of wave amplification
(for example, a localized highly baroclinic region that enhances baro-
clinic wave growth). Hamilton (1983) noted that the amplitude of wave 5
frequently varied on the same time scale as its period in the other SH
summers that he analyzed.

This amplitude-phase correlation can be clearly observed in the
Hovmöller diagram for this year (Figure 18). Each time the transient
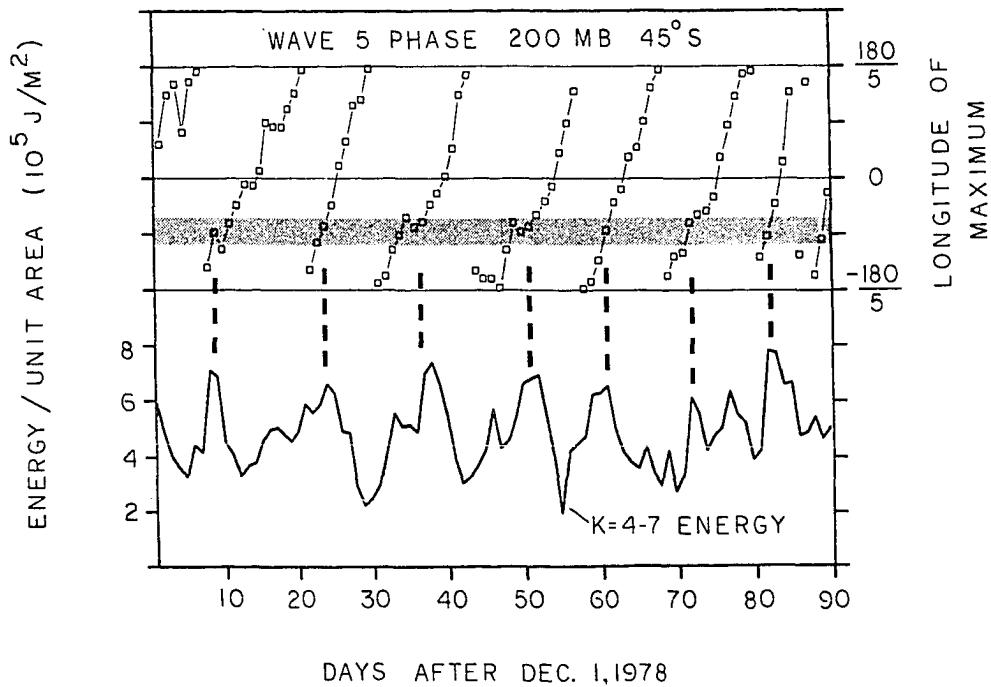
Figure 59. Top: Phase of wave 5 at 45°S latitude and 200 mb during 1978-79. Bottom: Medium-scale wave energy during 1978-79. Note that wave energy maxima are observed each time the phase of wave 5 is near the shaded region

wave meridional wind is towards the south in the region near 90°W longitude, it is observed to have large amplitudes. Slower phase progression is occasionally observed in this region, for example, January 1-10 (days 30-40) and January 18-25 (days 48-55). This region near South America is the region of the largest time-average wave (see bottom Figure 17).

Even though the amplitude-phase correlation (Figure 59) is apparent throughout the 1978-79 summer, close study of the energetics reveals that the transient-stationary interaction is clearest during the first several weeks of January 1979 (days 30-55). This is perhaps a result of the stationary waves achieving their largest amplitude during this time. Figure 60 details the energetics of waves 5-7 during this time. Wave 5 is completely dominant during January 1-10, whereas waves 6-7 are largest from January 15-25. The Hovmöller diagram (Figure 18) shows faster, shorter waves in the eastern hemisphere during this second period, whereas a wave-5 scale feature is observed in the western hemisphere, especially near South America.

The energetic diagram (Figure 60) reveals that during this period, there are two major differences from the 'usual' baroclinic growth-barotropic decay scheme. The waves are observed to grow barotropically on days 32-33 and 48-49, and decay baroclinically on days 27-28 and 39-41. In addition, baroclinic growth and barotropic decay are also observed. This indicates the transient waves are undergoing their 'usual' energy cycle, and at the same time interacting with the stationary wave (which may in turn modify the 'usual' growth-decay scheme).

Eliassen-Palm cross sections are shown in Figures 61a-b for two
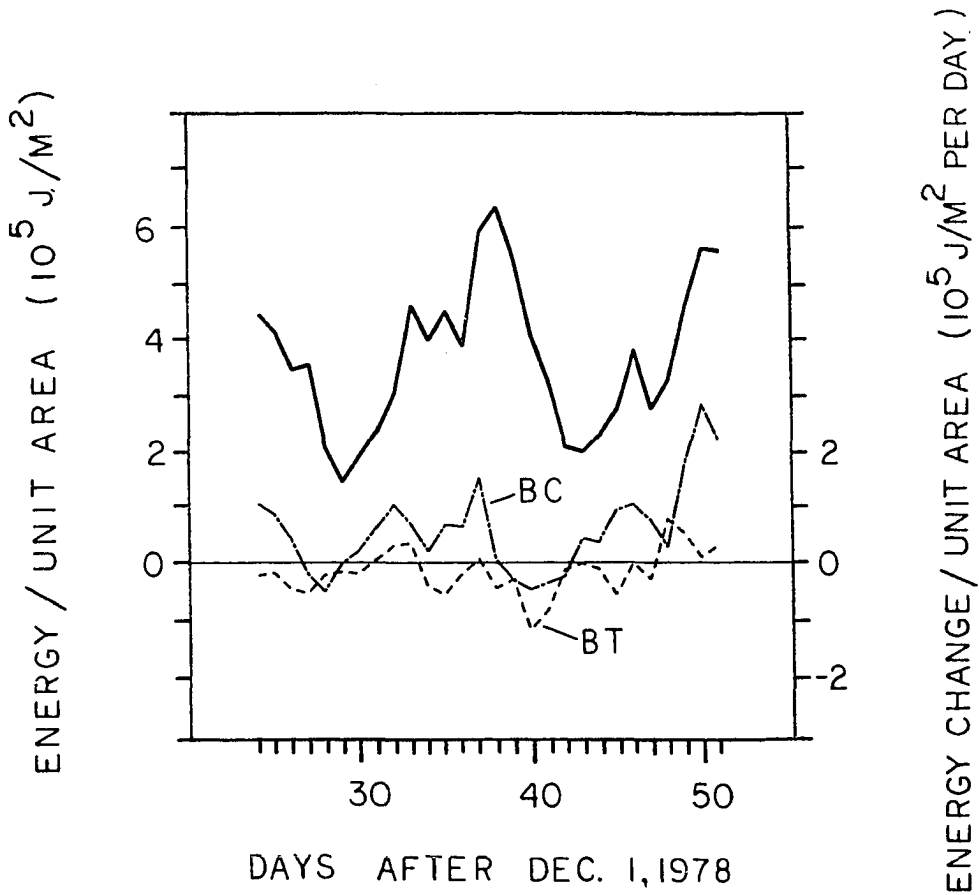
Figure 60. Detail of energetics of waves 5-7 during 1978-79
            interference episode. Heavy solid line is wave
            energy, plotted along with changes due to baro-
            clinic (BC) and barotropic (BT) wave-mean flow
            interactions. Note barotropic growth near days 33
            and 48, and baroclinic decay near days 28 and 40
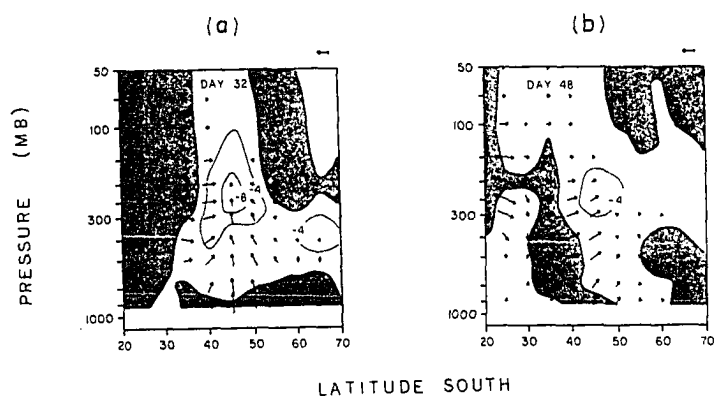
Figure 61. EP flux diagrams for two days during interference-
            induced barotropic growth. a) day 32, b) day 48 of
            1978-79. Plotting conventions are given in Ap-
            pendix C. Contour interval is 4 m/s per day
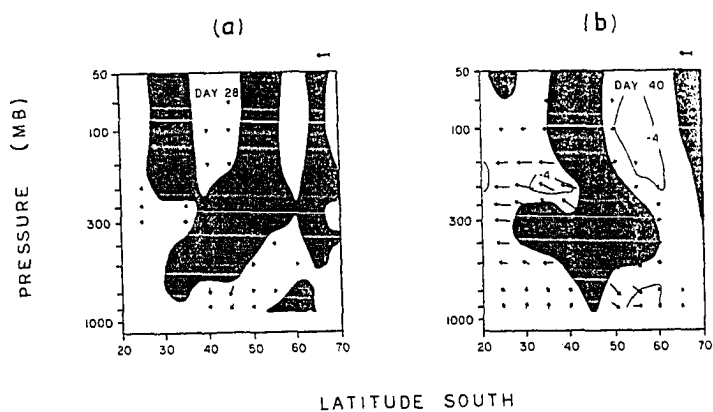
Figure 62. EP flux diagrams for two days during interference-
            induced baroclinic decay. a) day 28, b) day 40 of
            1978-79. Plotting conventions are given in Ap-
            pendix C. Contour interval is 4 m/s per day

days during the barotropic growth periods. The momentum flux is directed away from the jet core (which is near 45°S latitude and 250 mb) during both days, resulting in a decrease in jet intensity. This decrease in background wind results in a decrease in the (apparent) phase speed of the wave: this can be observed on the top of Figure 59, where wave 5 slows down near days 35 and 47. This behavior was also noted on the Hovmöller diagram (Figure 18). Direct calculation shows the jet core to decrease 7 m/s (from 33 to 26 m/s) between days 31 and 34, and 3 m/s (from 35 to 32 m/s) between days 44 and 47. This is in agreement with the near stationarity of the wave during these periods, as wave 5 exhibits a typical phase speed near 6 m/s. Note the largest source(s) of wave activity during the days in Figure 61 are in the mid-to-upper troposphere in low latitudes, as opposed to forcing near the surface during the 'usual' wave growth.

Figures 62a and b show EP cross sections for two days which exhibit baroclinic decay. There is now a source of wave activity near the jet core (much larger in Figure 60b due to the additional barotropic decay). The downward pointing arrows indicate equatorward heat flux during these days. Similar behavior was observed during the decay period of the case study (in Section V.I) as the wave radiated away from the jet, although not nearly as large as that observed here. Equatorward heat transport is observed at 850 mb in Figure 34a near days 30 and 40, although at no other time during the season. The simple wave interference model (to be introduced later in this chapter) will show that this equatorward heat flux is a consequence of the stationary-transient wave interference.

2.   <u>1979-80</u>

The identification of wave interference during this season comes
as a result of a study of the wave energetics during a period when
quasi-stationary waves were present. Figure 63 shows the energetics for
waves 4-5 from late January to mid February 1980 (days 50-75). Peaks
in wave energy are preceded by barotropic growth (on days 59-61 and
69-70), and baroclinic decay is observed on days 57 and 67. Again, the
'usual' baroclinic growth-barotropic decay is also observed. The a
amplitude-phase correlation apparent during 1978-79 is not evident
during this time period, as a single wavenumber is not dominant. Rather,
the Hovmöller diagram for this season (Figure 19) shows that during this
period, quasi-stationary waves are present, with structure hinting of
stationary-transient wave interference. This interference apparently
does not contribute as much to the dynamics as during 1978-79; it is a
smaller effect, and the interference is not as 'clean' as that observed
during the previous year. Further discussions will, therefore, center
on the 1978-79 observations to understand the interference-induced
dynamics.

B.   Time-Mean Wave Characteristics

Climatological mean stationary waves in the SH have been studied by
van Loon and Jenne (1972), van Loon et al. (1973), and Trenberth (1979),
based upon various data sets. Their results show that during the summer,
the stationary waves are of planetary scale (k = 1-3) and much weaker
than those in the NH, consistent with the character of the ultra-long
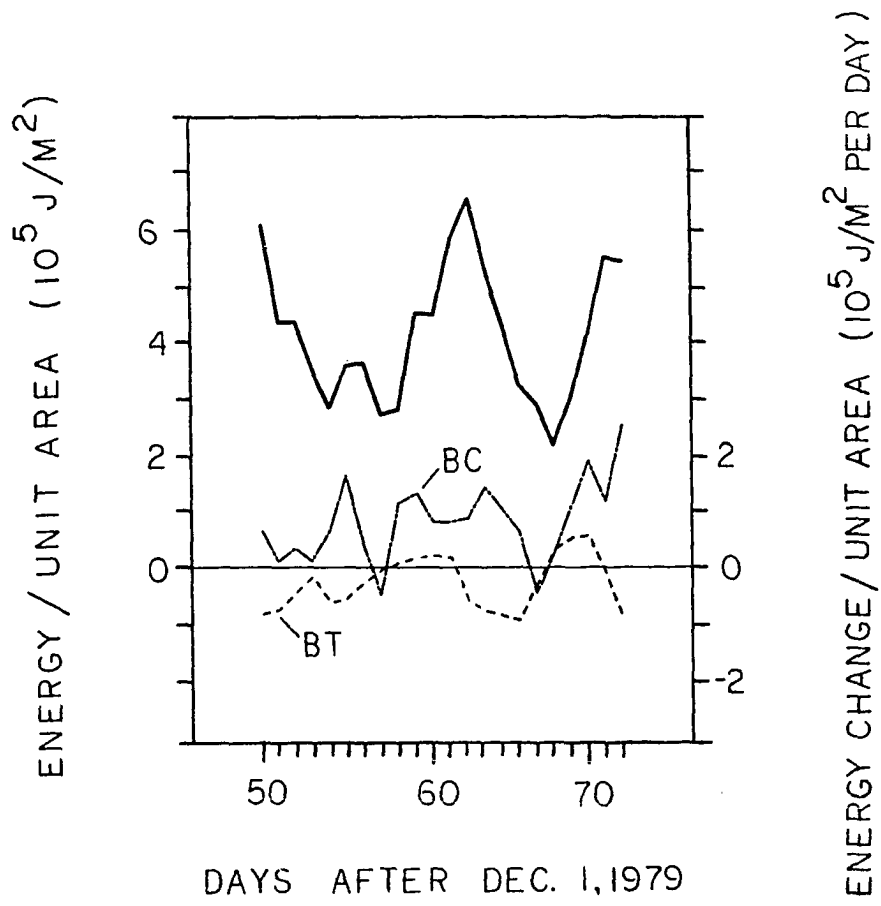
Figure 63. As in Figure 60, but for waves 4-5 during 1979-80

wave described earlier for this data. Occasionally, quasi-stationary (or time-mean) medium-scale waves are observed, in addition to the transient modes. This section discusses some of the characteristics of these low frequency oscillations observed during 1978-79.

A prominent problem arises when trying to study the structure of the stationary waves: it is found that the stationary waves in fact change in time, except with a longer time scale than that associated with the transient waves. This feature distinguishes them from truly climatological-mean waves. An additional problem arises because the transient waves are continually interacting with the stationary waves, complicating attempts of isolating either one. A zeroth-order estimate of the stationary wave structure is the time average over some reasonably long period, and this method is used here. Averages are taken over two complete cycles of stationary-transient interference (based upon energetic analyses), thus attempting to average out the transient waves.

The horizontal structure of the 28-day mean stationary wave is shown in Figure 64. This structure is calculated using only waves 5-7. The largest amplitude is localized between longitudes $135^{\circ}W$ and 0, a structure suggestive of a Rossby wave packet. This localized nature is in agreement with the Hovmöller diagram (Figure 18), which showed the largest time-mean amplitude and clearest evidence of interference in this region. The horizontal tilt of the waves in Figure 64 is from NE to SW, indicative of poleward latitudinal group velocity (Equation 5b with $k > 0$ and $\ell < 0$). Because the zonal group velocity of stationary Rossby waves is always eastward, this orientation shows that these waves are propagating from NW to SE.
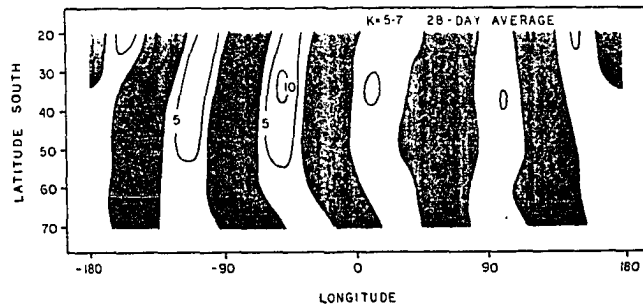
Figure 64. 28-day average (days 24-51) of the meridional wind
at 200 mb, using waves 5-7. Time period covered
is from December 24, 1978 to January 20, 1979.
Shaded winds are southward. Note the wave packet
behavior in the western hemisphere
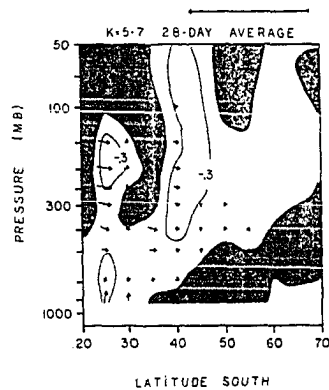
Figure 65. EP flux diagram for 28-day average (days 24-51)
wave structure, using waves 5-7. Plotting conven-
tions are given in Appendix C. Contour interval is
0.3 m/s per day. Note the low latitude, upper
tropospheric source regions

Figure 65 shows the time-mean EP signature of these waves. The poleward propagation is quite apparent, with a large source region equatorwards of 25°S latitude. In addition, there is a mid-tropospheric source region near 35°S latitude. This structure shows that the stationary wave does not originate near the surface, as an orographically or thermally forced feature might. An internal instability in this region is ruled out since the background potential vorticity gradient is large and positive throughout this region. Instead, the structure of this feature is suggestive of a source outside of southern mid-latitudes.

The time-varying nature of these low frequency waves can be seen in the different structure observed for different averaging periods. The January 1979 average found in Figure 1 of Randel and Stanford (1983) exhibits evidence of three separate Rossby wave trains. Two are found in the western hemisphere with similar structure to that observed in Figure 63. A third group is found in the eastern hemisphere with a group velocity vector oriented from SW to NE, suggestive of a high latitude source or reflection from high latitude barriers (such as negative refractive index regions in Figures 15a-c).

C. Origin of Stationary Medium-Scale Waves

To consider the origin of these observed low-frequency waves, one must know the dispersion characteristics of stationary Rossby waves. Theoretical studies of planetary-scale Rossby wave dispersion have been studied by several authors. Hoskins and Karoly (1981) and Held

(1983) have shown that, away from the region of forcing, dispersion characteristics are very similar to those given by barotropic models. Hoskins et al. (1977) studied the barotropic dispersion of a localized vorticity source on the sphere, incorporating various background zonal mean flows. A vorticity source at 30°N latitude produced a downstream splitting of the wavetrain, with long waves propagating poleward and shorter (medium-scale) waves moving equatorward. If easterly zonal winds at the equator are used (as suggested by climatology), the equatorward-moving waves were reflected, and there was little net response in the SH. If westerlies were used at the equator, however, cross-equatorial propagation resulted, and the largest long-term response was found near the source's anti-nodal point in the SH. Webster and Holton (1982) studied propagation in a more realistic zonally-varying basic state. They found that if this mean state included a 'duct' in which the zonal winds were westerly, waves of zonal scales less than that of the westerly duct could propagate from one hemisphere to another.

This cross-equatorial propagation may be part of the explanation for the observed stationary medium-scale waves during 1978-79. As shown by Kalnay and Paegle (1983), during January 1979, the usual tropical belt of easterlies at 500 mb was broken in the central Pacific (between 180 and 130°W longitude). They attribute this to anomalously large convective heating in this region. During February 1979, weaker tropical heating was associated with tropical easterlies, which (according to this explanation) restricted meridional propagation. The

February time-mean structure shows much smaller amplitude medium-scale waves.

The observed wave structure and basic state propagation characteristics are consistent with arguments that these stationary waves result from a source external to SH midlatitudes. The exact source is unknown, though Kalnay and Paegle (1983) argue that this wave train is also the result of the anomalous heating in the central Pacific.

D. Simple Interference Model

A simple analytical model of interfering transient and stationary waves is presented here to help understand this interaction. Although this is a grossly simplified model, it will demonstrate important features that can result from interference. In the next section, it will be shown that the observed interference can be partially understood in terms of this model.

This two-dimensional model assumes one purely transient wave and one purely stationary wave, both of the same zonal wavenumber and having arbitrary vertical structure. The streamfunctions for each are given by:

$$\phi_T(\lambda,z,t) = A_T(z) \sin (k\lambda - \sigma t) \qquad \text{(transient)}$$

$$\phi_S(\lambda,z) = A_S(z) \sin (k\lambda) \qquad \text{(stationary)}$$

Here k and σ are the zonal wavenumber and angular frequency, respectively. The total stream function is simply

$$\phi_{TOT}(\lambda,z,t) = \phi_T(\lambda,z,t) + \phi_S(\lambda,z).$$

The waves are in phase at time t = 0. It is obvious that the total wave energy is harmonic in time, with the same period as that of the transient wave.

Of interest here is the zonal-mean northward heat flux resulting from interference (note that in this model neither wave alone has any net transport):

$$\overline{v'T'}_{int}(t) = (\frac{g^2 \cdot H \cdot k}{2Rfr \cos \theta}) \sin (\sigma t)(A_S \frac{\partial A_T}{\partial z} - A_T \frac{\partial A_S}{\partial z})$$

Several important points to be noted include:

1) The heat flux is harmonic in time, with the period of the transient wave.

2) The heat flux depends on differing structures for the two waves. If the waves are identical, no interaction results.

3) Even though the individual waves exhibit no phase tilts with height, their interference can result in the net transport of heat.

The last point is an important one: two equivalent barotropic waves can interact baroclinically!

As a more realistic example, consider the same example where the waves have amplitude varying in the vertical but constant phase tilts with height:

$$\phi_T(\lambda,z,t) = A_T(z) \sin (k\lambda + m_T z - \sigma t) \quad \text{(transient)}$$

$$\phi_S(\lambda,z) = A_S(z) \sin (k\lambda + m_S s) \quad \text{(stationary)}$$

Here, m_T and m_S are the vertical wavenumbers of the transient and stationary waves, respectively. The vertical tilt of both waves results in (time-independent) heat transport for each:

$$\overline{v'T'}_{S,T} = (\frac{g \cdot H^2 \cdot k}{2Rfr \cos \theta}) \, m_{S,T} A^2_{S,T} \tag{17}$$

while the interference of the waves results in the following contribution:

$$\overline{v'T'}_{int}(t) = (\frac{g \cdot H^2 \cdot k}{2Rfr \cos \theta})(-(m_S + m_T)A_S A_T \cos ((m_S - m_T)z + \sigma t)$$

$$+ (A_S \frac{\partial A_T}{\partial z} - A_T \frac{\partial A_S}{\partial z}) \sin ((m_S - m_T)z + \sigma t)) \tag{18}$$

This result will be applied to the 1978-79 interference results in the next section.

E. Application of Model

In this section, an estimate of the interference-induced heat flux will be made based on the observed 1978-79 interference. This result will then be compared to that estimated from the simplified model, using Equation 18. The results are in modest agreement, and suggest that interference is the cause of the observed equatorward heat flux during decay of the interfering waves.

The observed interference will be studied between the limits shown in Figure 60 (i.e., between days 24 and 51), during which time approximately two complete interference cycles are observed. Each interference episode thus lasts approximately 14 days. The interference model predicts a harmonically-dependent interference-induced heat flux.

The actual heat fluxes at 40°S latitude, 250 mb and 50°S latitude, 500 mb are shown in the top and bottom, respectively, of Figure 66, along with the second harmonic of the time series at each position. The second harmonic, which accounts for approximately 40% of the variance at these positions, will be used as an estimate of the interference-induced contribution to the total heat flux. Similar analyses at each latitude and pressure result in meridional cross sections of the amplitude and phase (in time) of the interference-induced heat flux. These are shown in Figures 67a and b. The phase (time of the maximum poleward heat flux) is measured such that zero refers to the two waves constructively interfering. A value of -90 degrees thus refers to the maximum poleward heat flux at that position occurring one-quarter cycle before the waves are in phase.

Close inspection of the amplitude and phase plots reveals two separate areas where the interaction is 'coherent' in time: 1) 35-40°S latitude, 200-300 mb and 2) 45-55°S latitude, below 300 mb. The phase diagram (Figure 67b) indicates that the upper-level (1) maximum poleward heat flux occurs when the two waves are nearly in phase, while the lower (2) maximum occurs approximately one-quarter cycle before the waves are in phase. The center of these two areas are out of phase by approximately 110 degrees (0.31 cycle, or 4.3 days), in agreement with the phase difference between the dashed curves in Figures 66.

To apply Equation 18, estimates must be made for the vertical wavenumbers m_S and m_T. As shown in the case study in Section V.I, the vertical slope of the transient wave changes in time; here, we only want a rough estimate. This is done by applying Equation 17, i.e., relating
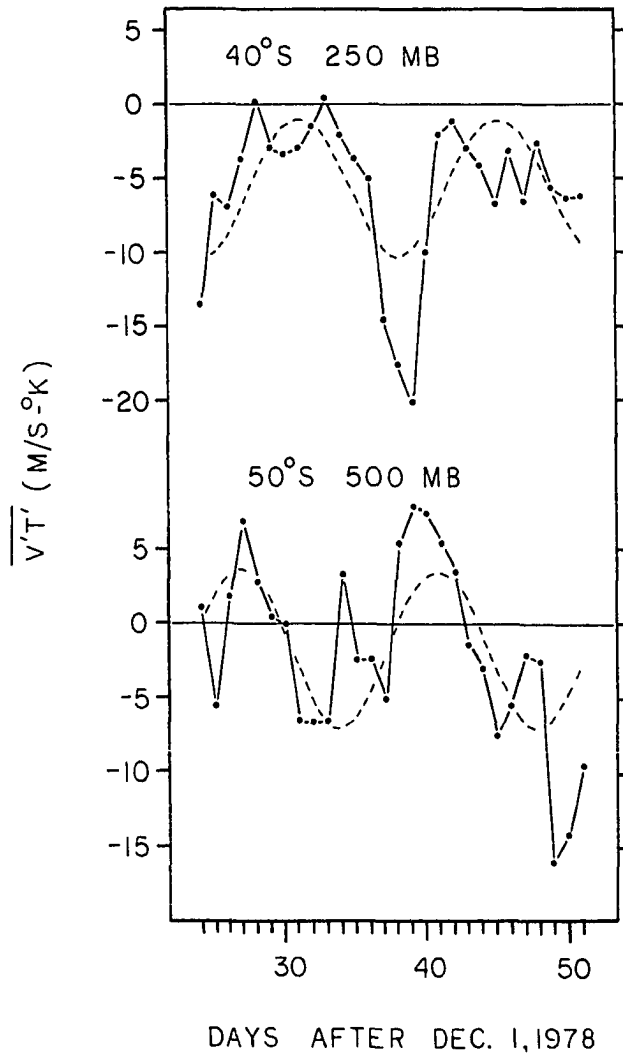
Figure 66. Zonally-averaged northward heat flux for each day
during two cycles of stationary-transient wave
interference. Top: 40°S latitude, 250 mb;
bottom: 50°S latitude, 500 mb. Individual values
are given by the dots, while the second harmonic
of each series is shown by the dashed line
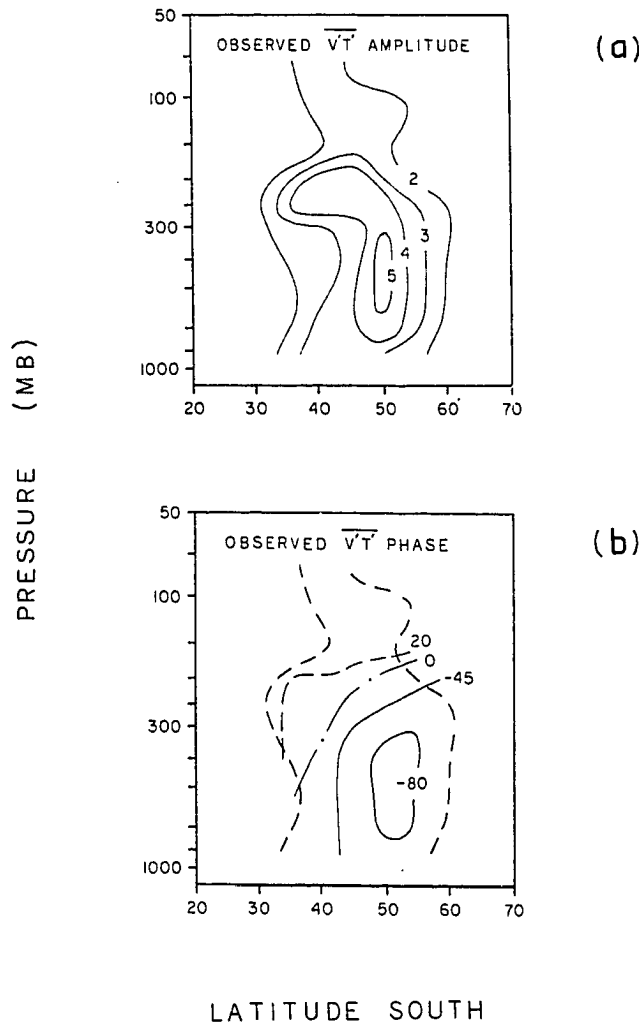
Figure 67. Meridional cross sections of the observed amplitude
(a) and phase (b) of the interference-induced heat
flux. Estimates are made by using the second har-
monic of the heat flux time series at each latitude
and pressure, as in Figure 66. Units in (a) are
(^{O}K - m/s), while the phase (time of maximum poleward
heat flux) in (b) is in degrees. The phase is
measured such that zero refers to the two waves
constructively interfering. A value of -90 degrees
thus refers to the maximum poleward heat flux at
that position occurring one-quarter cycle before the
waves are in phase

the observed heat flux to the time-averaged transient and stationary waves over this period. This turns out to be a poor estimate for the transient wave below 300 mb (constant tilt with height is a poor approximation), and difficult to apply to the stationary wave because of its complicated heat flux structure. For simplification, we assume $m_S \simeq m_T$, and choose $(m_S + m_T) \approx 0.3/H$ as a rough estimate.

Figure 68a shows the time-mean stationary wave amplitude (A_S), while Figure 68b shows that to the transient wave (A_T). It is important to note the differing meridional structures of these waves, which results in their possible interaction. Figure 68c shows the overlap term $(A_S A_T)$, while Figure 68d shows the meridional difference term $(A_S \, \partial A_T/\partial z - A_T \, \partial A_S/\partial z)$. The amplitude and phase of the estimated heat flux are given by (using Equation 18, with $m_S = m_T$):

$$amp = (OV^2 + MD^2)^{1/2}$$

$$phase = \tan^{-1} \left(\frac{OV}{MD}\right),$$

where

$$OV = - \left(\frac{g \cdot H^2 \cdot k}{2Rfr \cos \theta}\right)(m_S + m_T)(A_S A_T),$$

$$MD = \left(\frac{g \cdot H^2 \cdot k}{2Rfr \cos \theta}\right) \left(A_S \frac{\partial A_T}{\partial z} - A_T \frac{\partial A_S}{\partial z}\right).$$

Such calculations at each latitude and pressure result in the estimated amplitude and phase cross sections shown in Figures 69a and b. The model structure is seen to be similar to the observed cross sections (Figure 67). The amplitude structure hints at double maxima: near 50°S latitude in the mid-troposphere (400-500 mb), and near 40-45°S latitude in the upper troposphere (200-250 mb). The estimated phase structure
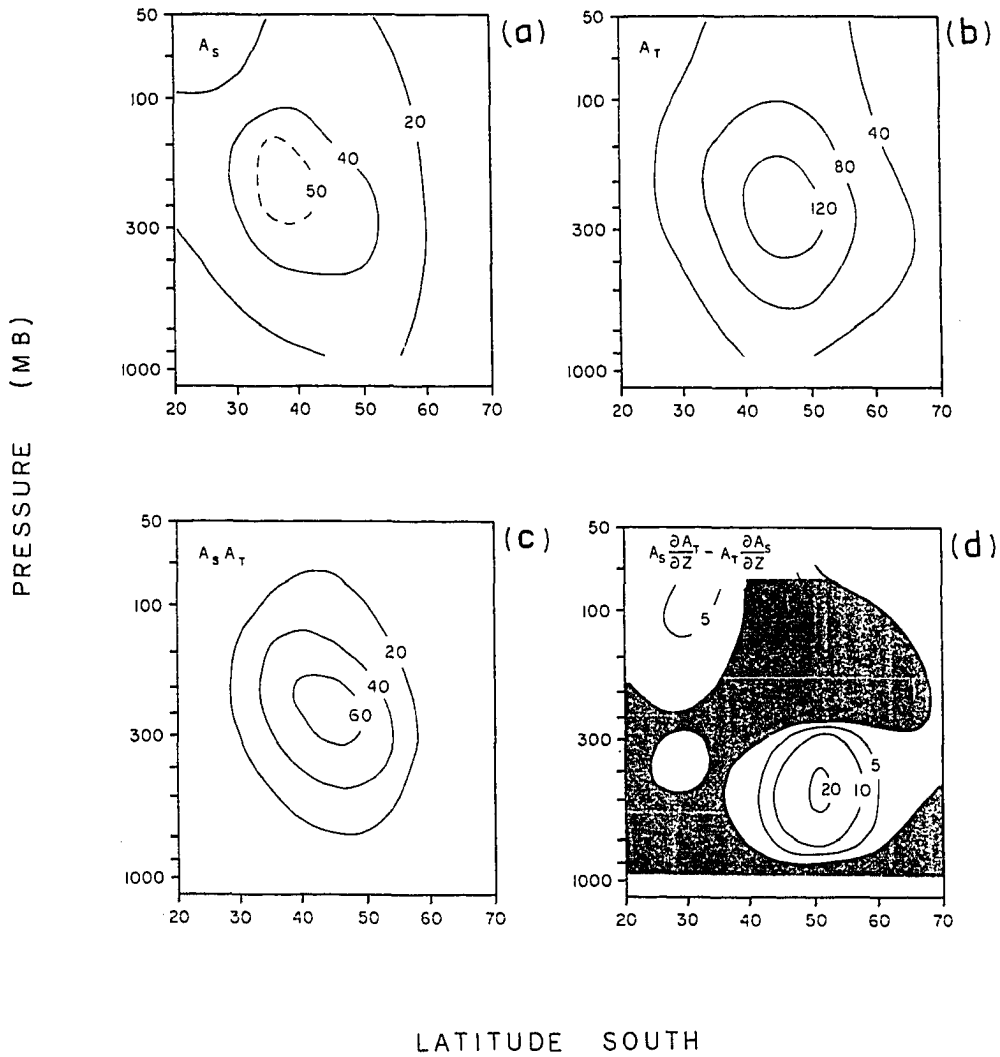
Figure 68.   Meridional cross sections of the time-average sta-
tionary (S) and transient (T) wave structure over
interference episode. a) stationary wave amplitude
(gpm), b) transient wave amplitude (gpm), c)
stationary-transient overlap (OV term in text -
10^2 gpm), d) meridional difference (MD term in text -
10^2 gpm H^{-1})
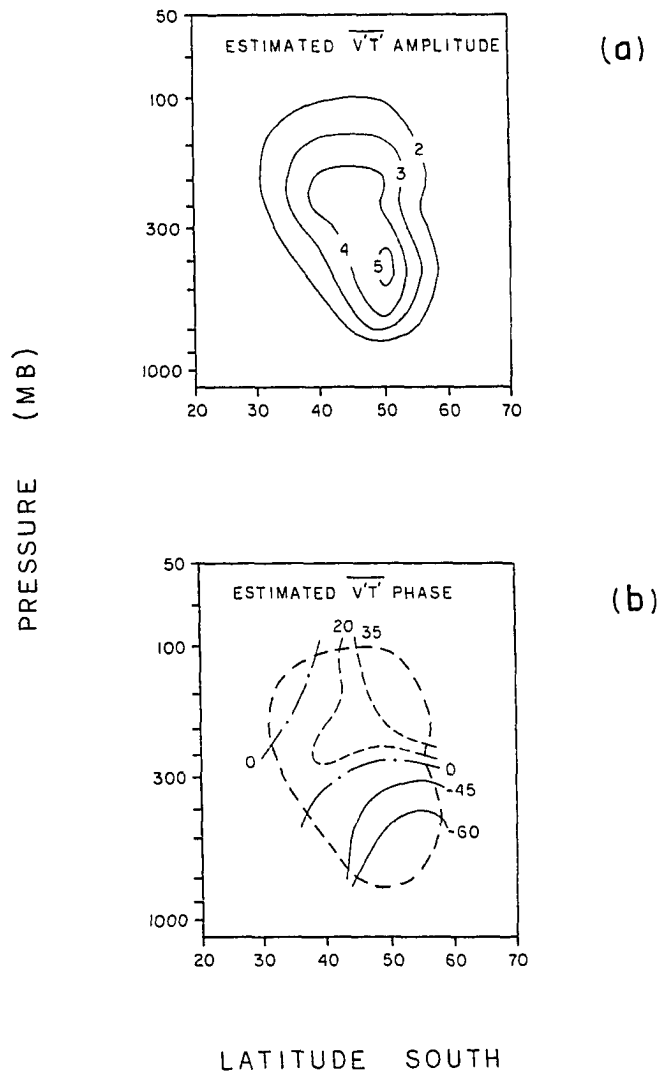
Figure 69. As in Figure 67, but for estimated heat flux amplitude (a) and phase (b), based on simple interference model calculations. Figure 67 gives the observed distributions

further delineates the two areas, as each is roughly coherent (in time). The estimated phase difference between these two regions is approximately 100 degrees, very close to the observed value. This agreement allows the underlying physics of this part of the interference interaction to be understood in terms of the simple model. The upper-tropospheric heat flux maximum is the result of the direct overlap of heat flux from each wave separately, thus reaching a maximum when the waves are in phase. This agrees with the large negative time-mean value throughout the interference (top of Figure 66).

The lower heat flux maximum is a result of the differing vertical structures of the transient and stationary waves. This is shown schematically in Figure 70. When the transient wave lags the stationary wave by one-quarter cycle, the stationary waves' advection of the transient waves' temperature perturbation $(v_S' T_T')$ is larger than the transient waves' advection of the stationary waves' temperature perturbation $(v_T' T_S')$. The average over a complete wavelength is thus positive. Half a cycle later, when the transient wave leads the stationary wave by one-quarter cycle, the situation is reversed, and the net heat flux is equatorward. The time-average in this situation is close to zero (as compared to the overlap case), in good agreement with the bottom of Figure 66.

The data and simple model results describe how the interference of these waves causes an equatorward heat flux, which would not otherwise occur. This heat flux results in the increase of the zonal mean temperature gradient, or baroclinicity of the zonal mean flow. This flow is then more susceptible to baroclinically unstable waves: the
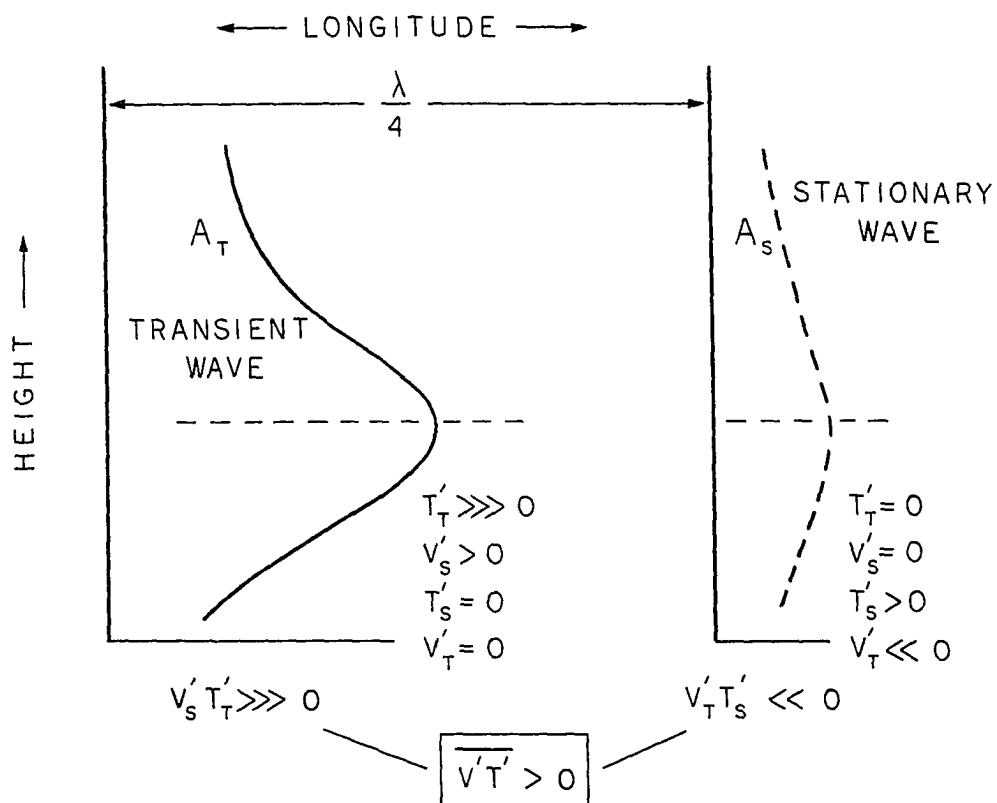
Figure 70. Schematic illustration of differing vertical structures of stationary and transient waves, and resulting net wave heat flux. This heat flux is maximized when the two waves (of the same zonal scale) are one-quarter cycle out of phase, as indicated in the top of the fiture. Perturbation velocities and temperatures associated with each wave are indicated, and their relative sizes are indicated by the number of 'greater than' signs for each

transient waves will grow (perhaps initiated by the poleward heat flux associated with interference!), and interfere again with the stationary wave. This feedback mechanism may account for the regular occurrence of the wave 5 structures during the summer of 1978-79. The important ingredient (and major difference from the other years) is the presence of the (externally forced — see Section VI.B) stationary medium-scale wave during this year.

Attempts to use a similar model to understand the momentum fluxes associated with interference were generally unsuccessful. This is perhaps due to the fact that a model with constant latitudinal phase tilts is a poor approximation, compared to the assumption of constant vertical structure. Similar analyses for the 1979-80 interference episode do not give such good results. In particular, the second harmonic does not explain much of the heat flux variance, i.e., there are other dynamics at work. Nonetheless, barotropic decay is observed in connection with the interference, although at no other time during the season. It is thus reasonable to assume it is a result of the interference, as during 1978-79.

VII. SUMMARY

In conclusion, this chapter will list the most important results
garnered from this study, and describe how they relate to some previous
studies. Suggestions will be made for future work.

A. Summary of the Most Important Results

1.   <u>Wave-zonal-mean exchange is a valid concept for describing the</u>
<u>SH summer atmospheric circulation.</u>   As stated in the Introduction, re-
cent emphasis in global atmospheric circulation studies has moved away
from zonal averaging to averaging locally in time. Such studies have
demonstrated marked zonal asymmetries in NH circulation statistics,
i.e., regions of frequent baroclinic activity (storm tracks) and low-
frequency variability (teleconnection patterns). A different situation
is evident in the SH summer, where a high degree of zonal symmetry is
observed, and the flow vacillates between highly perturbed and zonally
symmetric states. This vacillation was first noted by Webster and
Keller (1975) in the study of data from the EOLE constant density balloon
experiment conducted between August 1971 and July 1972. They found
quasi-periodic fluctuations in their 'zonal index' (ratio of wave KE to
zonal mean KE) with an apparent period near 20 days, although they could
not attribute these fluctuations directly to wave-mean flow interactions.
The energetic analyses presented here confirm this to be the underlying
principle behind their observations (at least during the SH summer).

2.   <u>Medium-scale waves in the SH summer result from finite ampli-</u>
<u>tude baroclinic instabilities.</u>   These waves exhibit a clearly defined

life-cycle of baroclinic growth, maturity, and barotropic decay.

Baroclinic growth is accompanied by a maximum of poleward heat flux in

the lowest levels (with associated upward propagation of the wave) and

a reduction in the mid-latitude zonal mean temperature gradient. At

maturity, the wave has started to decay barotropically, a process which

maximizes several days later. This decay is associated with strong

equatorward energy propagation, and (because the latitudinal phase and

group velocities of Rossby waves are oppositely directed) poleward

phase progression. The poleward movement of decaying cyclones in the SH

has been a long noted feature (Taljaard, 1972), although it is not clear

that the associated dynamics have been fully appreciated.

The lack of large amplitude stationary waves in the SH summer is

probably an important factor in the dominance of the medium-scale waves.

This is in agreement with studies of Hayashi and Golder (1983), who

compared results of NH general circulation model simulations with and

without mountains, and noted a marked increase in eastward moving waves

4-6 when the mountains were removed. This zonal symmetry is also un-

doubtedly basic to the similarity of the observed medium-scale wave

characteristics with those of modeled results (Simmons and Hoskins,

1978) and baroclinic waves in laboratory annulus experiments (Pfeffer

et al., 1974).

3.   The time-mean medium-scale wave structure is consistent with

the basic state wave propagation characteristics and conservation of

wave activity. The use of basic state propagation characteristics was

first employed by Charney and Drazin (1961) in explaining the absence

of all but the longest scale features in the stratosphere. It has since

been proven to be a quite useful concept in understanding Rossby wave propagation, and is in good agreement with the zonal-mean and medium-scale wave characteristics observed here. The peak of wave geopotential amplitude near the tropopause is quite consistent with the conservation of wave activity. This point has perhaps been silently understood, although not previously (to the author's knowledge) demonstrated observationally.

4.   The stationary medium-scale wave during 1978-79 exhibits clear linear interference characteristics with the transient waves. The excellent agreement between the simple interference model and observational results encourages a simplified understanding of a complex atmospheric process. In addition, this mechanism may account for the regular occurrence (and spectral purity) of medium-scale waves during the summer of 1978-79. This demonstrates how 'low-frequency' transients may affect entire hemispheric circulation patterns. One may speculate that a similar mechanism underlies the quasi-regular wave amplitude vacillations observed by Hamilton (1983) and Webster and Keller (1975), although periodic wave growth is also observed in laboratory annulus experiments with no standing waves present (Pfeffer et al., 1974).

B.   Suggestions for Future Research

The overriding theme of this research has been that a good deal of fundamental understanding of the atmosphere can be gained by studying the less well-known SH. It is, therefore, not surprising that future

SH observational studies are recommended, with emphasis on the following points:

1.   This study has detailed the wave characteristics during the SH summer. An obvious extension is to apply similar techniques to study the other seasons. In particular, what is the observed seasonal variation in wave characteristics? Are large year-to-year variations observed, and if so, can they be related to a physical mechanism such as the presence or absence of stationary waves? Are wave - mean-flow interactions regularly observed?

2.   Case studies provide detailed information on large-scale dynamics. Are baroclinic instabilities different in the SH winter? Can barotropic instability be observed in the SH?

3.   Low-frequency wave patterns (teleconnections) have recently received much attention in the NH and equatorial belt. It has been shown here that such features may also affect SH circulation patterns. What is the character of such features, and how do they compare with their NH counterparts? (It must be noted that an extremely long data base may be necessary for isolating such patterns, and the relatively short period of global SH observations may hinder such a study.)

The emphasis in this study (and these suggestions) has been on large, global-scale dynamics. The SH atmosphere undoubtedly exhibits unique phenomena on more localized scales, and much of it waits to be uncovered. It is hoped that the success met with in this study will serve as an impetus for further observational studies of the atmosphere of the SH.

VIII. BIBLIOGRAPHY

J. S. Bendat and A. G. Piersol, Random Data: Analysis and Measurement
   Procedures (Wiley-Interscience, New York, 1971), 407 pp.

K. H. Bergman, 1979: Mon. Wea. Rev. 107, 1423 (1979).

J. G. Charney, J. Meteorol. 4, 135 (1947).

J. G. Charney, J. Atmos. Sci. 28, 1087 (1971).

J. G. Charney and P. G. Drazin, J. Geophys. Res. 66, 83 (1961).

J. G. Charney and M. E. Stern, J. Atmos. Sci. 19, 159 (1962).

E. T. Eady, Tellus 1, 33 (1949).

H. J. Edmon, B. J. Hoskins, and M. E. McIntyre, J. Atmos. Sci. 37,
   2600 (1980).

F. G. Finger, H. M. Woolf, and C. E. Anderson, Mon. Wea. Rev. 93,
   619 (1965).

K. Fraedrich and E. Kietzig, J. Atmos. Sci. 40, 1037 (1983).

R. Gall, J. Atmos. Sci. 33, 374 (1976).

G. Hadley, Philos. Trans. R. Soc. London 39, 58 (1735).

E. Halley, Philos. Trans. R. Soc. London 16, 153 (1686).

K. Hamilton, Atmos. Ocean 21, 40 (1983).

D. L. Hartmann, C. R. Mechoso, and K. Yamazaki, J. Atmos. Sci. 41,
   351 (1984).

Y. Hayashi, J. Applied Met. 16, 368 (1977).

Y. Hayashi, J. Meteorol. Soc. Japan 60, 156 (1982).

Y. Hayashi and D. G. Golder, J. Atmos. Sci. 40, 941 (1983).

I. M. Held, in Large-Scale Dynamical Processes in the Atmosphere (Academic
   Press, London, 1983), p. 127.

B. J. Hoskins and D. J. Karoly, J. Atmos. Sci. 38, 1179 (1981).

B. J. Hoskins, A. J. Simmons, and D. G. Andrews, Q. J. R. Meteorol. Soc.
   103, 553 (1977).

E. Kalnay and J. Paegle, in First International Conference on Southern Hemisphere Meteorology (American Meteorology Society, Boston, 1983), p. 89.

K.-M. Lau and P. H. Chan, J. Atmos. Sci. 40, 2751 (1983).

K.-M. Lau and T. J. Phillips, J. Atmos. Sci. (1984), in press.

E. N. Lorenz, Tellus 7, 157 (1955).

M. E. McIntyre, J. Meteorol. Soc. Japan 60, 37 (1982).

R. D. McPherson, K. H. Bergman, R. E. Kistler, G. E. Rasch, and D. S. Gordon, Mon. Wea. Rev. 107, 1445 (1979).

C. R. Mechoso, Mon. Wea. Rev. 109, 2131 (1981).

A. H. Oort, Global Atmospheric Circulation Statistics, 1958-1973 (U.S. Department of Commerce, Rockville, Md., 1983), 180 pp.

T. N. Palmer, J. Atmos. Sci. 39, 992 (1982).

J. Pedlosky, Geophysical Fluid Dynamics (Springer-Verlag, New York, 1979), 624 pp.

R. L. Pfeffer, G. Buzyna, and W. W. Fowlis, J. Atmos. Sci. 31, 622 (1974).

R. L. Pfeffer, G. Buzyna, and R. Kung, J. Atmos. Sci. 37, 2129 (1980).

N. A. Phillips, Tellus 6, 273 (1954).

R. A. Plumb, J. Atmos. Sci. 40, 1669 (1983).

W. J. Randel and J. L. Stanford, J. Atmos. Sci. 40, 2312 (1983).

A. J. Simmons and B. J. Hoskins, J. Atmos. Sci. 35, 414 (1978).

J. J. Taljaard, in Meteorology of the Southern Hemisphere (American Meteorological Society, Boston, 1972), p. 139.

K. E. Trenberth, Mon. Wea. Rev. 108, 1378 (1980).

H. van Loon and R. L. Jenne, J. Geophys. Res. 77, 992 (1972).

H. van Loon, R. L. Jenne, and K. Labitkze, J. Geophys. Res. 78, 4463 (1973).

P. J. Webster and J. R. Holton, J. Atmos. Sci. 39, 722 (1982).

P. J. Webster and J. L. Keller, J. Atmos. Sci. 32, 1283 (1975).

A. Wiin-Nielsen, Tellus <u>19</u>, 540 (1967).

W.-B. Yu, J. L. Stanford, and R. L. Martin, J. Atmos. Sci. (1984), in press.

IX. ACKNOWLEDGMENTS

I would like to thank John Stanford for being both advisor and friend. His patience and wisdom is greatly appreciated, and his philosophy of careful science and clear thinking will follow me throughout my career.

I have shared an office and many graduate school experiences with Paul Newman, whom I thank for many beneficial discussions and arguments. I thank Russ Martin for his patient programming aide, and all the other members of Dr. Stanford's research group for ever-ready help and advice. This group's impact upon my learning cannot be underestimated. I also thank Dr. Mark Schoeberl for many stimulating discussions throughout the course of this work.

I thank my wife, Sharon. Her love and understanding have helped me throughout the many ups and downs experienced in connection with this thesis.

Finally, I wish to express my gratitude to my mother and father, to whom this work is dedicated. Their love, encouragement, and support have been with me always.

X. APPENDIX A:

NOTATION

A   wave geopotential amplitude

c   zonal phase speed

c_p specific heat of dry air at constant pressure

c_v specific heat of dry air at constant volume

DF   Eliassen-Palm flux divergence = $\rho_s^{-1} \nabla \cdot \vec{F}$

f   Coriolis parameter = $2\Omega\sin\theta$

F   Eliassen-Palm flux vector

g   gravitational acceleration

H   vertical scale height

k, ℓ, m zonal, meridional, vertical wavenumbers

L   horizontal length scale

N^2 Brunt-Väisälä frequency squared

p   pressure

q   potential vorticity

R   gas constant for dry air

r   radius of earth

t   time

T   temperature

u   zonal velocity

U   zonal velocity scale

v   meridional velocity

w   vertical velocity

x   zonal (east-west) coordinate = $\lambda r \cos\theta$

y   meridional (north-south) coordinate = $r\theta$

z   vertical coordinate = $-H \ln (p/p_{\infty})$

β north-south planetary vorticity gradient $\frac{\partial f}{\partial y} = 2\Omega \cos\theta/r$

ξ relative vorticity

θ latitude (negative in the SH)

λ longitude (positive eastward)

ρ density

σ angular frequency

τ time lag

ϕ geopotential

ψ wave amplitude of streamfunction

ω frequency

Ω angular velocity of earth

∇ horizontal del operator

$(\ )_{\infty}$ value of variable at surface

$(\ )_{s}$ basic state variable

$\overline{(\ )}$ zonally averaged variable

$(\ )'$ departure from zonal average

$\overline{(\ )}_{e}$ wave-induced meridional circulation

$\overline{(\ )}^{*}$ residual circulation

$(\ )_{k}$ zonal Fourier component at wavenumber k

$\tilde{(\ )}$ series mean

$(\ )_{S}$ stationary wave

$(\ )_{T}$ transient wave

XI. APPENDIX B:

DERIVATION OF POTENTIAL VORTICITY EQUATION

The horizontal momentum equations, per unit mass, on isobaric

(constant pressure) surfaces for a rotating fluid are:

$$x: \quad \frac{du}{dt} - fv = - \frac{d\phi}{dx} \quad \text{(B1)}$$

$$y: \quad \frac{dv}{dt} + fu = - \frac{d\phi}{dy} \quad \text{(B2)}$$

where ϕ is called the geopotential:

$$\phi = \int_{P_\infty}^{P} \frac{dp}{\rho} = \int_{P_\infty}^{P} RT(p)d(\ell n \ p)$$

and is a measure of the mean temperature between pressure p and the

surface. Here, d/dt is the total time derivative:

$$\frac{d}{dt} = \frac{\partial}{\partial t} + u \cdot \frac{\partial}{\partial x} + v \cdot \frac{\partial}{\partial y} + w \cdot \frac{\partial}{\partial z} \ .$$

The statement of mass conservation is:

$$\rho^{-1} \frac{d\rho}{dt} + \nabla \cdot \vec{u} = 0 \quad \text{(B3)}$$

and the thermodynamic equation is:

$$c_p \frac{dT}{dt} - \rho^{-1} \frac{dp}{dt} = 0 \quad \text{(B4)}$$

The nonlinearity of these equations, along with the generality

with which they apply to all scales of atmospheric motion, point to the

lack of a general solution. In order to get useful results, simplifying

assumptions are made which isolate the motions of interest.

One method of simplifying the equations is through a technique called scaling, in which variables are assigned typical values to compare the relative magnitudes of terms in the governing equations. For example, the ratio of the first two terms in the x-momentum equation is:

$$\frac{\frac{dU}{dt}}{fV} \simeq \frac{U}{fL} \simeq \frac{10 \text{ m/s}}{(10^{-4} \frac{1}{S})(10^6 \text{ m})} \simeq \text{Order } (0.1)$$

using typical values for medium-scale waves. This ratio, called the Rossby number, is generally small. The time derivative term is thus neglected to first approximation. This results in a balance between the Coriolis force and the pressure gradient force, or geostrophic balance. If similar analyses are applied to the other equations, the lowest order results are:

$$fv = \frac{\partial \phi}{\partial x} \tag{B5}$$

$$fu = - \frac{\partial \phi}{\partial y} \tag{B6}$$

$$\frac{\partial u}{\partial t} + \frac{\partial v}{\partial y} + \rho_s^{-1} \frac{\partial}{\partial z} (\rho_s w) = 0 \tag{B7}$$

$$\frac{\partial \phi}{\partial z} = \frac{RT}{H} \tag{B8}$$

$$\frac{d}{dt} (\frac{\partial \phi}{\partial z}) + N^2 w = 0 \tag{B9}$$

where $N^2 = \frac{R}{H} (\frac{\partial T_s}{\partial z} + \frac{g}{c_p})$

and $\frac{d}{dt} = \frac{\partial}{\partial t} + u \cdot \frac{\partial}{\partial x} + v \cdot \frac{\partial}{\partial y}$.

Equations B5 and B6 can be combined with Equation B8 to give the

so-called thermal wind equations:

$$f \frac{\partial v}{\partial z} = \frac{R}{H} \frac{\partial T}{\partial x} \tag{B10}$$

$$f \frac{\partial u}{\partial z} = - \frac{R}{H} \frac{\partial T}{\partial y} \tag{B11}$$

A problem arises from the use of the geostrophic winds, as they are exactly nondivergent, and satisfy the continuity equation with zero vertical velocity. The geostrophic approximation gives no information about the vertical velocity, although this information is needed to determine gravitational restoring forces. An additional piece of information is supplied by considering the fluid vorticity, equal to the normal (to the Earth's surface) component of the curl of the velocity:

$$\zeta = (\frac{\partial v}{\partial x} - \frac{\partial u}{\partial y}) = f^{-1} \nabla^2 \phi$$

An equation for the vorticity is obtained from Equations B1 and B2:

$$\frac{d}{dt} (\nabla^2 \phi) + f^2 (\frac{\partial u}{\partial x} + \frac{\partial v}{\partial y}) = 0$$

This is combined with the continuity Equation B7 to give:

$$\frac{d}{dt} (\nabla^2 \phi) - f \rho_s^{-1} \frac{\partial}{\partial z} (\rho_s w) = 0$$

which is in turn combined with the thermodynamic Equation B9 to get a single equation for the geopotential:

$$\frac{d}{dt} (f^{-1} \nabla^2 \phi + \rho_s^{-1} \frac{\partial}{\partial z} (\rho_s \frac{f}{N^2} \frac{\partial \phi}{\partial z})) = 0 \tag{B12}$$

The conserved quantity in brackets in Equation B12 is called the

potential vorticity, q. Even though the flow is geostrophic to high

degree, it is the small departures from geostrophy which determine the

fluid evolution. The motion is thus termed quasi-geostrophic. The

potential vorticity Equation B12 takes into account these small depar-

tures from geostrophy without having to calculate them explicitly.

It is the governing equation of motion for the large scale fluid motions

in the atmosphere. If forcing is present, it may be incorporated on

the right hand side of Equation B12.

XII. APPENDIX C:

EP FLUX DIAGRAM CONVENTIONS

Components of the EP flux vector $\vec{F}$ (Equation 9a) in spherical coordinates are given by:

$$F_\theta = - r \cos \theta \, \rho_s \, \overline{u'v'}$$

$$F_z = \frac{rf \cos \theta \, R}{H} \, \rho_s \, \frac{\overline{v'T'}}{N^2}$$

and the EP flux divergence is:

$$\rho_s^{-1} \, \nabla \cdot \vec{F} = \rho_s^{-1} \left(\frac{1}{r \cos \theta} \frac{\partial}{\partial \theta} (\cos \theta \, F_\theta) + \frac{\partial F_z}{\partial z} \right)$$

Due to the spherical geometry of the earth, if we represent $\vec{F}$ on a latitude-height grid, $\vec{F}$ will appear divergent when $\nabla \cdot \vec{F} = 0$. Edmon et al. (1980) has shown that this problem is overcome by defining:

$$\widehat{\vec{F}} = 2\pi r \cos \theta \vec{F}$$

If arrows are drawn in the (θ-z) plane whose horizontal and vertical components are proportional to the quantities $\widehat{F}_\theta$ and $\widehat{F}_z$, respectively, the resulting pattern of arrows will look divergent if and only if $\nabla \cdot \vec{F} = 0$.

The arrows in the EP figures here thus have components:

$$\widehat{\vec{F}} = \begin{bmatrix} \widehat{F}_\theta \\ \widehat{F}_z \end{bmatrix} = \rho_s \cdot 2\pi r^2 \begin{bmatrix} - \cos^2 \theta & \overline{u'v'} \\ \frac{f \cos^2 \theta \, R}{H} & \frac{\overline{v'T'}}{N^2} \end{bmatrix}$$

The reference arrow in each figure represents $\rho_s \cdot 2\pi \cdot r^2$ times 10 m/s of $\widehat{F}_\theta$, and 0.1 m/s of $\widehat{F}_z$.

The zonal-mean momentum equation is (Equation 8):

$$\frac{\partial \bar{u}}{\partial t} = \overline{fv^*} + \frac{\nabla \cdot \vec{F}}{\rho_s r \cos \theta}$$

Contours of the quantity $DF = \nabla \cdot \vec{F} / \rho_s r \cos \theta$, proportional to the zonal wind acceleration, are drawn in the EP diagrams, with units of m/s per day. Regions of positive EP flux divergence are shaded.

XIII. APPENDIX D:

MODIFIED POTENTIAL VORTICITY

Palmer (1982) has shown that for very large scale (in latitude)
motions, the northward potential vorticity flux, $\overline{v'q'}$, evaluated using
geostrophic winds, is not proportional to the EP flux divergence. This
is because the geostrophic wind for such scales is horizontally divergent
(on the sphere). Palmer shows that a slight modification to the
latitudinal derivative term in q' removes this problem, and defines a
modified $q'_{(m)}$:

$$q'_{(m)} = \frac{1}{fr^2} \left[\frac{1}{\cos^2\theta} \frac{\partial^2 \phi'}{\partial\lambda^2} + \frac{\sin\theta}{\cos\theta} \frac{\partial}{\partial\theta} \left(\frac{\cos\theta}{\sin\theta} \frac{\partial\phi'}{\partial\theta} \right) \right]$$

$$+ g^2 \frac{\partial}{\partial p} \left(\frac{f}{N^2} \rho_s^2 \frac{\partial\phi'}{\partial p} \right)$$

With this definition, Equation 10 becomes an exact statement, i.e.:

$$\overline{v'q'}_{(m)} = \frac{1}{\rho_s r \cos\theta} \nabla \cdot \vec{F}$$

Similarly, Equation 11b becomes:

$$\frac{\partial}{\partial t} \left(\frac{1}{2} \frac{\overline{q'_{(m)}}^2}{\bar{q}_y} \right) + \overline{v'q'}_{(m)} = 0 \tag{D1}$$

with

$$\bar{q}_y = \frac{2\Omega\cos\theta}{r} + \frac{1}{r^2} \frac{\partial}{\partial\theta} \left(\frac{1}{\cos\theta} \frac{\partial}{\partial\theta} (\cos\theta\bar{u}) \right)$$

$$- g^2 \frac{\partial}{\partial p} \left(\frac{f}{N^2} \rho_s^2 \frac{\partial\bar{u}}{\partial p} \right)$$

Equation D1 may alternately be written as

$$\frac{\partial}{\partial t} A_{(m)} + \nabla \cdot \vec{F} = 0 \qquad \qquad (D2)$$

with

$$A_{(m)} = r \cdot \cos \theta \cdot \rho_s \cdot \frac{\frac{1}{2} \overline{q'^2_{(m)}}}{\overline{q}_y} \qquad \qquad (D3)$$

Palmer has further shown that $\vec{F}$ may be written as

$$\vec{F} = A_{(m)} \cdot \vec{C}_g$$

where $\vec{C}_g$ is the Rossby wave group velocity. Insertion into Equation D2 gives:

$$\frac{\partial}{\partial t} A_{(m)} + \nabla \cdot (A_{(m)} \cdot \vec{C}_g) = 0 \qquad \qquad (D4)$$

This equation can be regarded as a local conservation equation, where $A_{(m)}$ is an exactly conservable measure of local quasi-geostrophic planetary scale wave activity.

The quantity $q'_{(m)}$ is used in the calculations here, although the results are virtually identical to those using q'.